

ESTABLISHMENT OF SUBSIDENCE MODEL CONSIDERING LONG-TERM BEHAVIOR OF CAVING ZONE IN LONGWALL COAL MINE

孟, 凡非

<https://hdl.handle.net/2324/4496023>

出版情報 : Kyushu University, 2021, 博士 (工学) , 課程博士
バージョン :
権利関係 :



**ESTABLISHMENT OF SUBSIDENCE MODEL
CONSIDERING LONG-TERM BEHAVIOR OF
CAVING ZONE IN LONGWALL COAL MINE**



KYUSHU UNIVERSITY

FANFEI MENG

JUNE 2021

**ESTABLISHMENT OF SUBSIDENCE MODEL
CONSIDERING LONG-TERM BEHAVIOR OF CAVING
ZONE IN LONGWALL COAL MINE**

A DOCTORAL DISSERTATION

SUBMITTED TO THE GRADUATE SCHOOL OF ENGINEERING
KYUSHU UNIVERSITY

AS A PARTIAL FULFILLMENT OF THE REQUIREMENTS FOR THE DEGREE
OF
DOCTOR OF PHILOSOPHY OF ENGINEERING

BY

FANFEI MENG

SUPERVISED BY

ASSOCIATE PROFESSOR DR. TAKASHI SASAOKA

PROFESSOR DR. HIDEKI SHIMADA

DEPARTMENT OF EARTH RESOURCES ENGINEERING
KYUSHU UNIVERSITY

FUKUOKA, JAPAN

JUNE, 2021

ABSTRACT

Ground subsidence in underground coal mining areas causes environmental damage and creates hazards on the ground surface, which is long-term, widely distributed, and can lead to large-scale geological disasters. Achieving a high-precision method to predict mining subsidence deformation is very important for assessing environmental damage and identifying countermeasures. The longwall mining system is a very productive and efficient method and is widely used throughout the world as a coal mining technique. During longwall mining, the immediate roof caves in behind the hydraulic shield support as coal is continuously extracted and then overlying strata hangs up to form a rock beam. As the longwall face continually advances, the rock beam breaks into large blocks and then collapses when the span reaches a certain limiting value. The broken rock fills in the goaf area in a space termed a caving zone. The overburden strata can be divided into three vertical zones including the continuous deformation zone, the damage zone, and the caving zone. Brillouin optical time-domain reflectometer (BOTDR) technology is introduced and adopted in this study to obtain the movement data along the vertical direction above the goaf. According to the results of the field measurements, the deformation of the caving zone is the most complex, and the long-term behavior has not yet been clarified. Therefore, this research discusses the deformation mechanism and long-term behavior of the caving zone by means of field investigations, laboratory tests and numerical simulations. This dissertation consists of seven chapters and the main contents in each chapter are listed as follows:

Chapter 1: This chapter introduces the research background and significance of prediction of the long-term behavior of the caving zone in order to predict long-term surface subsidence due to the longwall coal mining operation. The reviews of the literatures on the measurement technology and prediction of surface subsidence and ground behavior were also presented in this chapter. This chapter describes the objectives of this research.

Chapter 2: The chapter describes the BOTDR technology for measurement of ground movement due to longwall coal mining operation. As the BOTDR technology can measure the strain at specific monitoring points, the returned strain is somewhat different from the rock mass strain outside of the monitoring point. Hence, in case that the strain data returned from the monitoring point is considered the same as the overall deformation of the rock, a large cumulative error will occur, especially in the caving zone and the damage zone. The new calculation model which can calculate the ground deformation above the goaf based on the data measured by BOTDR technology is proposed. In this model, the ground above the goaf is divided into three zones: the caving zone, the damage zone and the continuous deformation zone then the constitutive model of each zone is developed. The caving zone is represented as the constitutive model of rock fragments. The deformation of this model contains the compressive deformation of the rock body and the sliding behavior among rock particles. The damage zone represents the fractures zones as an elastoplastic body. The continuous deformation zone represents the elastic deformation zone and unconsolidated zone which can be modeled as the elastic body. The amount of surface subsidence above the goaf can be calculated by the summation of deformation of each zone.

Chapter 3: In order to discuss the applicability of BOTDR Technology, the long-term behavior of each zone and the applicability of calculation models proposed in Chapter 2, the field investigation and the analysis of measurement data is conducted in Zhangzhuang coal mine, Anhui Province, China. Based on the measurement data, it is confirmed that the overburden can be classified into three zones: the continuous deformation zone, the damage zone, and the caving zone in terms of the deformation behavior. Large strain can be observed in the caving zone and it increases with increasing elapsed time after extraction of longwall panels. Additionally, as a result of predicting the deformation in each zone using the calculation model proposed in this research, the long-term deformation behaviors of the damage and continuous deformation zones can be simulated. However, the long-term deformation behavior of

the caving zone cannot be simulated and it is remarkable differences between the predicted value and measured one. Hence, it can be said that the long-term deformation behavior of the caving zone has to be understood and modeled in order to predict long-term ground behavior due to the longwall coal extraction.

Chapter 4: In order to understand the long-term deformation behavior of the caving zone, a series of triaxial creep tests are conducted using the specimen that simulates the caving zone filled with rock fragments under different axial pressures, confining pressures and size distributions of rock fragments. Based on the results of a series of creep tests, it can be said that both the axial and confining pressures have an obvious impact on the creep behaviors of the specimen. The creep strain increases with increasing the axial pressure and decreases with increasing the confining pressure. Moreover, it also can be recognized that the breakage of rock fragments inside of the specimen occur during creep tests and this phenomenon also has an obvious effect on the creep behavior of the specimen. Here, the relative breakage index, which is calculated by the total breakage volume divided by the total volume of rock fragments, is introduced in order to evaluate the breakage degree of rock fragments in the specimen. The size of rock fragments in the specimen has an obvious impact on the breakage behavior of rocks and the breakage index become large when the contents of large size rock fragments is large. In addition, as the breakage index increases with increasing confining pressure, it can be expected that the decrease of creep strain with increasing confining pressure is due to the internal structural change of the specimen. Therefore, it can be said that the bulking coefficient, which represents the characteristics of volume expansion, is an important factor for prediction of long-term deformation behavior of the caving zone.

Chapter 5: The bulking coefficient plays an important role for long-term deformation behavior of the caving zone. In order to understand the long-term deformation behavior and determine the bulking coefficient of the specimen that simulates the caving zone, a three-dimensional numerical model of the specimen is

developed and simulated by means of Particle Flow Code (PFC) Ver. 5.0. The failure criterion of the rock fragments in the specimen is also implemented in this simulation. Based on the results of a series of numerical simulations, the deformation behavior of the specimen can be understood and the creep behaviour of the specimen can be simulated by Burgers creep model. Moreover, as the particle size distribution of rock fragments in the specimen, the axial and confining pressures have an obvious impact on the bulking coefficient of the specimen, the deformation characteristics parameter which represents the effects of the particle size distribution of rock fragments in the specimen, axial and confining pressures on the bulking coefficient is determined and introduced. Then the bulking coefficient under different conditions and elapsed time can be predicted.

Chapter 6: In this chapter, a new creep model is proposed in order to predict long-term behavior of the caving zone considering the change of bulking coefficient of caving zone. The new model attempts to predict the long-term behavior of the caving zone by incorporating the deformation characteristics parameter into the transition creep factor in the Burgers creep model. Compared with the results of the triaxial compressive tests, it can be said that the new creep model can simulate the behavior of the specimen simulated caving zone more accurately than the classic Burgers model. Moreover, compared with the results of laboratory tests with excavation model and the field measurement data of the caving zone in Zhangzhuang coal mine, it can be verified that the new proposed model can predict the long-term deformation behavior of the caving zone.

Chapter 7: This chapter summarizes and concludes the results and findings of this research.

Keywords: Subsidence calculation model; BOTDR technology; Triaxial compression experiment; Broken rock; Relative breakage index; Bulking coefficient; Particle discrete element; Fractional order creep model

ACKNOWLEDGEMENT

Time flies like arrow, and it is the third summer in Fukuoka. Fukuoka is a beautiful place with grateful nature view and kind people. I'm very appreciative of my growth during living here these three years. The gain of the three years' struggle here will accompany me on my new life in the future.

I would like to sincerely thank my supervisor, Assoc. Prof. Takashi Sasaok for his careful guidance of my scientific research. His patient encouragement and support have made my research mind more and more mature and his experience in the rock mechanics research area is of great help to the content and structure logic of my graduation thesis. Thanks again for his every kind work to improve this thesis.

I am also grateful to Prof. Hideki Shimada for his help in my life and study in Fukuoka over the past three years and he has given me a lot of meaningful comments. Especially I am very grateful to him as the guarantor when I rent a house in Fukuoka, which helped me a lot. The vigor in him has been infecting me a lot, making me remain optimistic when facing the problems of scientific research and life.

Except for my supervisor, I would like to express my deep appreciation to Assoc. Prof. Akira Sato for from Kumamoto University. As another member of the examination committee of this dissertation, also deserves my hearty gratitude for his kind help and useful advice to improve this work.

Sincere gratitude goes to my previous supervisor at China University of Mining and Technology (CUMT) for supporting the broken rock triaxial compression experiment in CUMT. As my research enlightenment tutor, his guidance that I learnt at CUMT has laid the important foundation for the research in this thesis.

I would like to express the appreciation to Assoc. Prof. Minwei Zhang for his kind support in my application for Kyushu University and the scholarship of China

Scholarship Council (CSC). Then, special appreciation and gratitude are expressed to Assoc. Prof. Chunde Piao, the visiting scholar of our research group, for providing the fieldwork information which is important in this work. He also gave a lot of meaningful and crucial comments for the fieldwork part in this thesis, which helped the research route very much. I would also like to thank Asst. Pro. Akihiro Hamanaka for his every kind of help, which made my research and daily life much easier here.

As a research student, I spent the majority time with the other PhD students in our office of the laboratory of Rock Engineering and Mining Machinery. I would like to thank Dr. Nuang, Dr. Thant, Dr. Pisith, Dr Tumelo, Dr. Ma, Dr. Dyson, Dr. Cho, Dr. Jona, and Dr. Ulaankhuu for creating the harmonious laboratory environment, which made my academic research and daily life in Kyushu University happy and bright.

Last but not least, sincere gratitude goes to the financial sponsor of my PhD period at Kyushu University, the State Scholarship Fund from China Scholarship Council (CSC).

Finally, I would like to thank my family and friends. I have left my hometown for ten years, and I felt being loved by them every second in these ten years. The emotional support from them strengthens me during my struggle time.

Fanfei Meng
Kyushu University
Fukuoka
May 2021

CONTENTS

ABSTRACT.....	I
ACKNOWLEDGEMENT	V
LIST OF FIGURES	XI
LIST OF TABLES	XVI
1 Introduction.....	1
1.1 Research background and significance.....	1
1.2 Literature review.....	3
1.2.1 Measurement of overburden movement	3
1.2.2 Experimental study of gangue mechanical behavior in caving zone.....	5
1.2.3 Numerical simulation study of gangue mechanical behavior in caving zone.....	8
1.2.4 Prediction method of surface subsidence.....	9
1.3 Contents of research.....	13
References.....	18
2 Measurement of ground behavior due to longwall mining operation by using BOTDR technology.....	23
2.1 Introduction of BOTDR technology.....	23
2.2 Calculation model of overburden subsidence based on BOTDR technology.....	25
2.2.1 Simplify.....	25
2.2.2 Subsidence calculation model of rock mass in caving zone.....	29
2.2.3 Subsidence calculation model of rock mass in damage zone	32
2.2.4 Subsidence calculation model of rock mass in the continuous deformation zone	34
2.3 Parameter analysis of subsidence calculation model	35
2.3.1 Calculation and sensitivity analysis of damage factor.....	35
2.3.2 Calculation and sensitivity analysis of contact parameters.....	40
2.3.3 The final calculation model after parameter analysis	45

2.4 Summary	46
References	47
3 Field investigation of overburden subsidence by using BOTDR technology.....	50
3.1 Distributed monitoring.....	50
3.1.1 A survey of test site	50
3.1.2 Distributed monitoring scheme for overburden in the goaf.....	51
3.1.3 Overburden monitoring results by BOTDR technology.....	55
3.2 Determination of calculation model parameters	57
3.2.1 Initial bulking coefficient.....	57
3.2.2 Particle contact parameters	57
3.2.3 Damage distribution parameters	58
3.2.4 Calculation of stress strength and plastic strain strength	58
3.3 Results of the field subsidence monitoring based on BOTDR technology	60
3.3.1 Results analysis of field test overburden subsidence.....	60
3.3.2 Accuracy discussion of the subsidence calculation model	61
3.4 Summary	64
References.....	65
4 Creep and breakage behavior of gangue broken rock in caving zone under triaxial compression condition	67
4.1 Creep experiment design.....	67
4.1.1 Material components.....	67
4.1.2 Material preparation.....	69
4.1.3 Experimental apparatus.....	71
4.1.4 Experimental procedure	73
4.2 Creep results of broken rock under triaxial compression test.....	73
4.2.1 Gradation loading.....	74
4.2.2 Creep results of broken rock	74
4.3 Particle breakage characteristics of broken rock under triaxial compression loading.....	81

4.3.1 Introduction of particle breakage indexes.....	81
4.3.2 Particle breakage characteristics of broken rock under different grading size index	82
4.3.3 Particle breakage characteristics of broken rock under different confining stress.....	86
4.4 Summary	88
Reference	90
5 Prediction of broken rock bulking coefficient based on particle discrete element method.....	92
5.1 Establishment of the particle numerical model.....	92
5.1.1 Boundary profile of rock fragments in particle mechanical model	93
5.1.2 Deformation and damage criterion of rock fragments in particle mechanical model	94
5.1.3 Simulation of the time effect in particle mechanical model	95
5.1.4 Bulking coefficient monitoring in particle mechanical model.....	96
5.2 Schemes	97
5.2.1 Model sizes	97
5.2.2 Loading process	97
5.2.3 Modelling parameters	98
5.2.4 Specimens	99
5.3 Change law of bulking coefficient.....	100
5.3.1 Bulking coefficient.....	100
5.3.2 Change rate of the bulking coefficient.....	103
5.3.3 Deformation inside rock blocks	105
5.3.4 Internal force distribution of the broken rock.....	106
5.4 Bulking coefficient calculation and prediction model	107
5.4.1 Calculation equation of bulking coefficient.....	107
5.4.2 Deformation characteristic parameter in the prediction model.....	108
5.4.3 Feasibility of bulking coefficient prediction.....	111

5.5 Summary	114
Reference	115
6 Creep equation of broken rock in caving zone based on Fractional order theory ..	117
6.1 Creep curves of broken rock in caving zone.....	117
6.2 Fractional order theory.....	118
6.2.1 Introduction of fractional order theory	118
6.2.2 Definition of fractional calculus	119
6.2.3 Fractional basic mechanical elements -- Abel dashpot.....	121
6.3 Creep model of broken rock based on fractional order theory	122
6.3.1 Construction of broken rock creep model.....	122
6.3.2 Calculation of broken rock creep model.....	125
6.4 Reliability of proposed broken rock creep model.....	126
6.5 Application of the fractional order creep model	137
6.5.1 Caving zone subsidence considering time based on fractional order model.....	138
6.5.2 Proof of caving zone subsidence prediction equation.....	138
6.6 Summary	141
References.....	142
7 Conclusions.....	143
Supplement	147

LIST OF FIGURES

Figure	Title	Page
Fig. 1-1	Deformation of strata above an extracted area without permanent pillars	2
Fig. 1-2	Compaction stage of caving zone	3
Fig. 1-3	Influencing factors in underground engineering design	6
Fig. 1-4	Creep mutation points of saturated broken rock with the particle size 5 - 10 mm	7
Fig. 1-5	Comparison of elapsed time to bond failure between three bond-aging models	9
Fig. 1-6	Vertical deformation of an undermined rock rock mass in flat-lying measures	10
Fig. 1-7	Schematic diagram of influence function calculation	11
Fig. 1-8	Flow chart of the research contents and approaches	17
Fig. 2-1	Diagram of BOTDR monitoring principle	24
Fig. 2-2	Diagram of mining overburden state and stratum zoning	26
Fig. 2-3	Distributed monitoring scheme for overburden in mining area	27
Fig. 2-4	Monitoring points of the optical fiber sensor	28
Fig. 2-5	Schematic diagram of simplification of compressive deformation of the rock mass in the caving zone	30
Fig. 2-6	Schematic of the monitoring points number method of caving zone	32
Fig. 2-7	Schematic of the monitoring points number method of damage zone	34
Fig. 2-8	Schematic of the monitoring points number method of continuous deformation zone	35
Fig. 2-9	Stress-strain curve of sandstone under different confining	37

LIST OF FIGURES

	pressures	
Fig. 2-10	Change rules of distribution parameters and peak strain under different confining pressures	38
Fig. 2-11	Influences of ε_0 and m_0 on the strain ε_r^b in the caving zone	39
Fig. 2-12	Influences of ε_0 and m_0 on the strain ε_r^d in the damage zone	42
Fig. 2-13	Curve of θ 's influence on the calculated strain ε_r^b in the caving zone	44
Fig. 2-14	Curve of μ 's influence on the strain ε_r^b in the caving zone	45
Fig. 3-1	Layout location of hydrostatic levelling line and optical fiber monitoring point	52
Fig. 3-2	Guide head assembling and optical cable welding	53
Fig. 3-3	Pay-off reel	53
Fig. 3-4	Lowering of the optical cable	54
Fig. 3-5	Monitoring station	55
Fig. 3-6	Vertical strain distribution	56
Fig. 3-7	Results of subsidence calculation model based on the measured strain in different zones	60
Fig. 3-8	Ground surface subsidence results based on calculation model, integral method and field monitoring	61
Fig. 4-1	Quantitative analysis from profile-fitted peaks by XRD	68
Fig. 4-2	Four particle groups with different particle size after screening	69
Fig. 4-3	The sample of saturated time confirming test	71
Fig. 4-4	The weight change at saturated time tests	71
Fig. 4-5	Physical diagram of MTS815	72
Fig. 4-6	Schematic of the sample design	73
Fig. 4-7	Stress loading path of the Chen's loading method	74
Fig. 4-8	Strain time curve of broken rock undergoing different	75

LIST OF FIGURES

	confining pressure	
Fig. 4-9	Strain time curve of broken rock undergoing different size grading	75
Fig. 4-10	Creep curve of broken rock under different confining pressure	77
Fig. 4-11	Creep curve of broken rock under different size grading	80
Fig. 4-12	Creep strain rate curve of broken rock with size grading G5 and $p_0 = 3$ MPa	81
Fig. 4-13	Definition of the relative breakage index B_r	82
Fig. 4-14	Relative breakage indexes of broken rock under different size grading	85
Fig. 4-15	Relative breakage index of different size grading after creep test	85
Fig. 4-16	Relative breakage indexes of broken rock under different confining pressure	87
Fig. 5-1	Gangue scanning geometry and rock fragment templates in simulation.	93
Fig. 5-2	The deformation of contact inside the gangue rock-block	95
Fig. 5-3	The schematic diagram of the specimen and the loading plates	97
Fig. 5-4	The changing curve of the bulking coefficient under different conditions	101
Fig. 5-5	Bulking coefficient change rate under different conditions	104
Fig. 5-6	2D cut of the specimen No.3	105
Fig. 5-7	Deformation of the researched rock block with time increasing	105
Fig. 5-8	The block internal contact force distribution under different Talbot grading index	106
Fig. 5-9	The morphology of intact coal before and after creep loading	107
Fig. 5-10	Changing curves of deformation characteristic parameter a	109

LIST OF FIGURES

Fig. 5-11	Average and variance of a under the influence of different factors	111
Fig. 5-12	Bulking coefficient results comparison based on different method	113
Fig. 6-1	Creep curve modes of standard rock material	117
Fig. 6-2	Schematic diagram of Abel dashpot	121
Fig. 6-3	Creep characteristic curves of Abel dashpot in different β -th-order	122
Fig. 6-4	Schematic diagram of the broken rock creep model	123
Fig. 6-5	Creep compression test data and fitted results at the size grading of G5	128
Fig. 6-6	Creep compression test data and fitted results at the size grading of G4	130
Fig. 6-7	Creep compression test data and fitted results at the size grading of G3	132
Fig. 6-8	Creep compression test data and fitted results at the size grading of G2	134
Fig. 6-9	Creep compression test data and fitted results at the size grading of G1	136
Fig. 6-10	Determination coefficient of fractional order creep model and classic Burgers model	137
Fig. 6-11	Deformations of overburden after mining at 220m of simulation experiment	139
Fig. 6-12	Comparison of the subsidence between prediction equation and experiment results	139
Fig. 6-13	Comparison of the subsidence between prediction equation and	140

LIST OF FIGURES

	on-site results	
--	-----------------	--

LIST OF TABLES

Table	Title	Page
Table 3-1	Physical and mechanical properties of the strata in Zhangzhuang coal mine	51
Table 3-2	Main technical performance indicators of N8511 optical fiber strain analyzer	52
Table 3-3	Damage parameters of overburden in the goaf	58
Table 4-1	The component percentage of rock blocks	69
Table 4-2	Particle size grade schemes of the broken rock block	70
Table 5-1	Meso-structure parameters of the numerical model	98
Table 5-2	Mechanical parameters of the numerical intact rock model	99
Table 5-3	Specimen schemes in particle discrete element numerical simulation	100
Table 6-1	Fitting parameters of the subsidence prediction equation with simulation experiment results	140
Table 6-2	Fitting parameters of the subsidence prediction equation of on-site calculated results	141
Table S1	Fitting parameters of the fractional order creep model of broken rock	147

CHAPTER 1

1 Introduction**1.1 Research background and significance**

Long wall mining system is a very productive and efficient method and widely used in the world as a coal mining technique (Zhang et al. 2019). It is predicted that by 2025, the total global coal consumption will be around 7.4 billion tons (International Energy Agency 2020), which means that lots of large-scale goafs or mined-out areas are generated. Hence, the height of the longwall face will continually increase, resulting that more rock beam breaks into large blocks. These blocks will collapse when the span reaches a certain limiting value, filling into the goafs and then a zone called caving zone will be formed, as shown *a* part in Fig. 1-1. Above this zone, the rock mass is damaged because of the stress release after the rock block collapsing, and the damage rock mass formed the fissured intermediate zone, *b* part as shown in Fig. 1-1. *c* part in Fig. 1-1 is surface zone in the overburden, which also called unconsolidated layers. According to Fig. 1-1, this part is also subsidence which is because the fissured intermediate zone's deformation. Therefore, the surface subsidence is caused by the rock block collapsing in the caving zone, and the deformation of the caving zone play important parts in the subsidence of the whole overburden at longwall mining.

Overburden subsidence not only affect the subsequent mining of coal, but also cause environmental problems such as the damage to farmland and transportation facilities, the pollution of water resources and unsafety of building structures. Therefore, timely grasping and evaluating the characteristics of the overburden deformation and the surface subsidence plays an important role in ensuring safe production and solving ecological problems of mining areas.

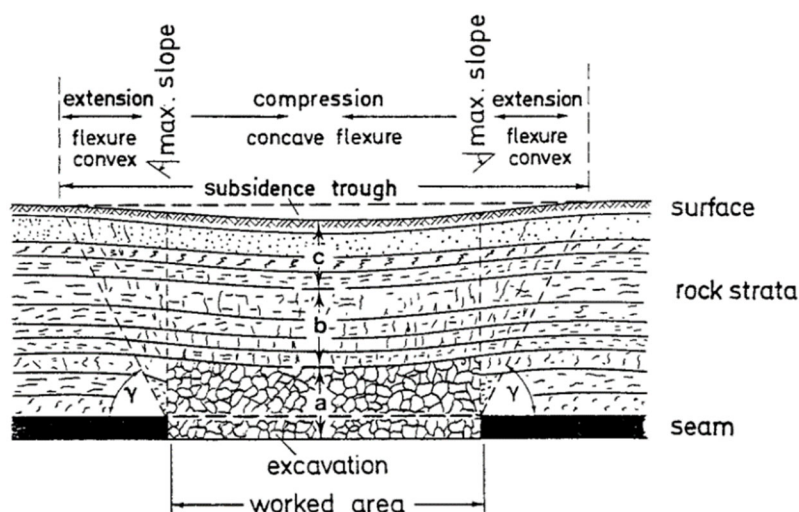


Fig. 1-1 Deformation of strata above an extracted area without permanent pillars **a.** zone of shattered roof beds over mine excavation; **b.** fissured intermediate zone; **c.** surface zone; γ limit angle from edge of working to through margin (Kratzsch 1986)

There is a large amount of broken coal, gangue and broken collapsed rocks in a caved goaf formed by traditional longwall mining (Feng and Wang 2020; Zhang et al. 2019; Liu et al. 2020). The void ratio in caving zone is the largest among the overburden, shown in Fig. 1-1, resulting that this zone is the easiest deforming part of the whole overburden and the movement of rock blocks in this zone is complex to learn. Hence, it is necessary to study the mechanical behavior of the broken rock in the caved goaf. As the broken rock has a diverse structure and complex internal interactions (Fan and Liu 2017), the characteristics of bulking deformation in the caving zone are important to analyze and determine mining operation process. As a parameter describing the expansibility of the rock mass, the bulking coefficient plays an important role in the research of mining roof management, mining subsidence law and preventing spontaneous coal combustion in goafs (Sun et al. 2020; Palchik 2015; Hao et al. 2011).

In addition, the overburden deformation in a coal mine is a long-term study, and rock mass especially in caving zone usually shows significant creep behaviors under a long-term compressive stage (Li et al. 2020). The general movement stages of the overburden are shown in Fig. 1-2.

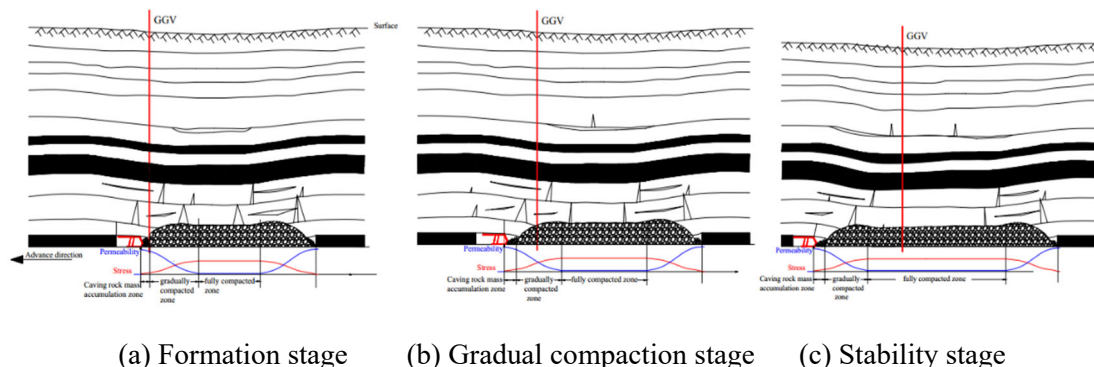


Fig. 1-2 Compaction stage of caving zone (Zhang et al. 2019)

Generally, the caving zone deformation after mining will experience three stages (Shihao et al. 2016; Zhang et al. 2016; Zhang et al. 2019): after the excavation of the goaf, the rock blocks in the immediate roof falls into the goafs and the caving zone is formed, called formation stage (Fig. 1-2(a)). Then, the above overburden damages and compresses the rock mass in the caving zone. This stage is called the gradual compaction stage (Fig. 1-2(b)). Finally, the stress in the overburden becomes rebalanced and the deformation stabled gradually. This stage is called the stability stage (Fig. 1-2(c)). The deformation of the caving zone also will drive the movement of above rock mass and finally influence the surface subsidence. Hence, when studying the deformation of the caving zone and the surface subsidence, time effect should be considered.

1.2 Literature review

1.2.1 Measurement of overburden movement

Distributed optical fiber sensing technology was born in the late 1970s. Since it was proposed, distributed optical fiber sensing technology has developed very rapidly. Many researchers over the world have been interested in the theory of distributed optical fiber sensing. A lot of research on the principle and application technology has been carried out, and a series of laboratory experiments and engineering practices have been carried out. The contents included the calibration of distributed optical fiber sensors, the development of sensor packaging methods, and the development of new

application fields.

At present, global positioning system (GPS) technology (Chrzanowski et al. 1997; Can et al. 2012), synthetic aperture radar (SAR) technology (Jung et al. 2007), and interferometric SAR (InSAR) technology (Guéguen et al. 2009; Yang et al. 2017) have advantages of high spatial positioning, high deformation sensitivity, and high spatial resolution. They can monitor the continuous subsidence of the goaf and obtain the surface subsidence distribution data. However, due to the increasing thickness of overburden, more and more interference factors especially the time effect will influence the deformation of the rock mass in the overburden, and then effect the surface subsidence. Hence, it is hard to grasp the overburden subsidence rule only by using the above technologies for ground subsidence monitoring (Donnelly 2009). Brillouin optical time-domain reflectometer (BOTDR) is a distributed optical fiber strain sensor technology whose operation is based on Brillouin scattering. It can obtain the strain distribution information of measurand fields overburden vertically along the fiber path in time and space simultaneously (Zhang et al. 2018; Hong et al. 2017). In addition, BOTDR technology equipment can measure continuous strain along an optical fiber over 10 km (Ohno et al. 2001) and is used to detect deformations or predicted problems in large-scale structures. Hence, with the vertically strain distribution of the overburden during the monitoring period by BOTDR technology, the overburden long-term deformation even in the large-scale field test can be obtained.

There are other technologies which can also obtain the information in the overburden, but they have their own limitation. For example, using the time-domain reflectometry (TDR) technology and underground radon concentration detection technology to monitor the overburden subsidence in the goaf is still in the validation stage (O'Connor and Murphy 1997; Kies et al. 2006). There are many interferences when applying the electrometric method (Hohmann and Ward 1981), and the borehole sound velocity method is mostly used for auxiliary detection (Yasar and Erdogan 2004). For CT detection method, it is difficult to realize distributed quantitative detection (Li

et al. 2017). As for BOTDR technology, it used the fiber to implant into the overburden and the fiber is light weight and small size. Moreover, because when monitoring the optical fiber is buried into the overburden and the buried hole is closed, the interferences is less.

According to the above analysis, distributed optical fiber sensor based on BOTDR is a better choice to monitor deformation of overburden rock in coal mines (Zhang D et al. 2017; Madjdabadi et al. 2017; Gang et al. 2015). When disposal the strain data from BOTDR technology, it is common to integrate the optical fiber sensor monitored strain along the whole monitored range to obtain the deformation behavior of the overburden (Zhang GX et al. 2017). The integrate method can be describe as:

$$W_o = \int \varepsilon dh \quad (1-1)$$

where W_o is the subsidence of the overburden; ε is the strain data from BOTDR technology; h is the height of the monitored overburden.

However, the integration method does not involve the relationship between mechanical parameters rock mass and the subsidence stage of the overburden. Moreover, the uneven deformation of the overburden rock mass is not considered. Hence, it's necessary to propose a more considered and precise method to disposal the BOTDR strain data of the mining overburden.

1.2.2 Experimental study of gangue mechanical behavior in caving zone

At the field scale, the typical environmental factors undergoing by the surrounding rock mass of an underground cavern are confining pressure, temperature and ground water, and the intrinsic rock factors of the rock mass are jointing, anisotropy, composition, and grain size. These factors should be considered when exploring the underground rock mass behaviour, as shown in Fig. 1-3 (Zhang 2014).

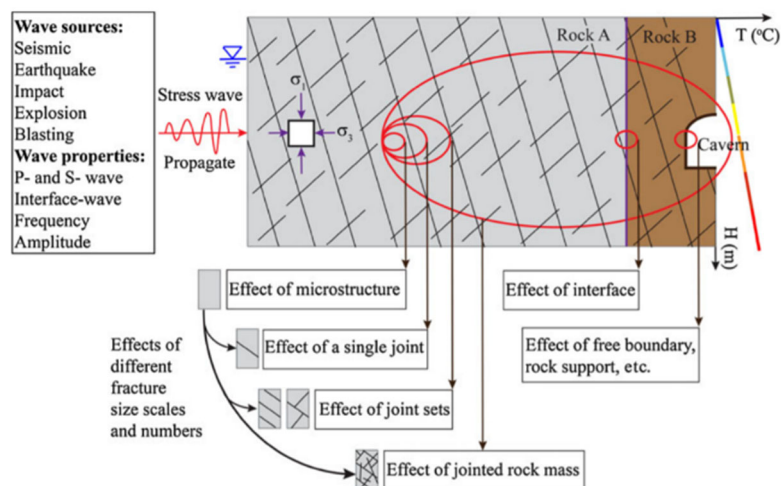


Fig. 1-3 Influencing factors in underground engineering design (Zhang 2014)

However, guidance and standards in field testing and design are generally lacking, and moreover advances in understanding of mechanical behaviour have been paced to an important degree by advances in experimental techniques (Zhang 2014). Hence, reliable results of rock mechanical behaviour can be obtained at the laboratory scale under appropriate testing design.

Large-scale experiments on coarse-grained materials began in the 1960s. Marsal conducted a series of large-scale tests on rockfills in 1967 (Marsal R J 1967). The Japanese Society of Soil Engineering conducted a series of studies and summaries on the mechanical properties of coarse-grained materials and on-site compaction control. With the development of high earth-rock dams, high-rise buildings, high-speed railways and highways, coastal riverbanks and other projects, the experimental research of coarse-grained materials has continued to deepen (Hufenus et al. 2006). The test methods mainly include large-scale triaxial, large-scale direct shear and in-situ tests. The confined compression test results of the saturated broken rock have showed that there is an exponential function relationship between time and the porosity of the broken rock (Ma et al. 2014).

As for the creep behavior test of disaggregated rocks, at a certain applied stress, creep occurred at an attenuated rate, and steady-state creep occurred at a zero rate in the broken rock. At high stress, samples exhibited creep at an attenuated rate and steady-

state creep at a non-zero rate (Li et al. 2020). To predict and get the law of the overburden deformation, it is also important to precisely analyze the influence of the time on bulking coefficient of the broken rock in caved zones (Ma et al. 2014; Sun et al. 2020).

Ma Zhanguo studied the creep behavior of saturated disaggregated sandstone under uniaxial compression with side limits (Ma Z, 2014). The relationship between axial displacement and time was described by nonlinear exponential function in his study. It was also proved that the mechanisms of the creep of saturated disaggregated sandstones include fragment crushing, fragment splitting, fragment rearrangement and possibly stress corrosion cracking due to the existence of water. Experimental research on the creep behavior of saturated fractured rock mass was also carried out by scholars (Li et al. 2013; Ma et al. 2014), and the fitting formular of axial strain and time was obtained. The creep parameter of saturated broken rock increased with the increase of axial stress. There were creep mutation points in the broken rock under the condition of high axial pressure, as shown in Fig. 1-4.

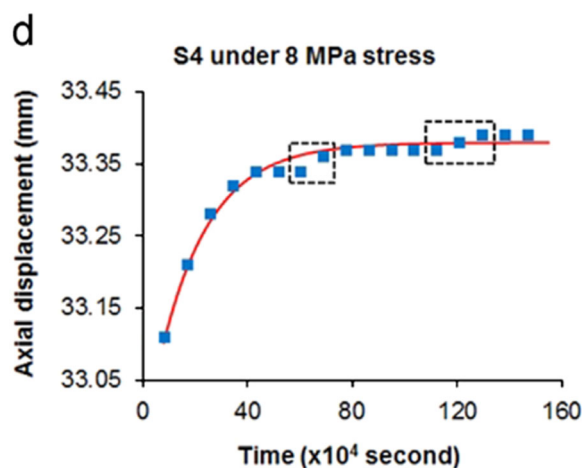


Fig. 1-4 Creep mutation points of saturated broken rock with the particle size 5 - 10 mm (Ma et al. 2014)

However, because of the difficulty to add confining pressure during the triaxial compression loading, the study of the confining pressure influence on the broken rock creep behavior is not enough. In addition, although the creep behaviors of the intact or damaged rock mass have been studied by many researchers recently (Zang et al. 2017;

Firme et al. 2016; Kabwe et al. 2020), for broken rock in the caving zone, there are few studies about the time effect on the expansion and deformation of it not only by experiment tests but also by numerical simulation studies.

1.2.3 Numerical simulation study of gangue mechanical behavior in caving zone

Numerical simulation test can help to get the visualized interaction results inside the rock model during the test. As for the creep research of broken rock masses, Ma ZG et al. used the particle discrete element numerical simulation method to simulate broken rock masses of different shapes by using particle clusters (Ma et al. 2019). In his study, the Burger contact model is used for intra-particle cluster contact, and the linear contact model is used for inter-particle cluster contact. The creep behavior of broken rock under triaxial compression was simulated, and the relationship between particle gradation and creep was discussed. The creep behavior of broken rock masses under dry and wet conditions was studied by PFC software (Zhao and Song 2015). A particle dispersion model was proposed to simulate the wet state of the broken rock which reduced the short-term strength, the stress threshold of strength degradation and the contact friction coefficient compared with the dry state. It was proved that in a rockfill specimen where aggregates were irregularly packed, breakage mainly occurred at the angularities or corners of aggregates. However, the coefficient reduction value in this study needed to be obtained through indoor experiment fitting, indicating that only a qualitative method was proposed. Also, this article ignored that most of the water in nature is acidic, and the short-term strength of the friction coefficient will decrease compared with water. The rotation of particles in the process of crushing rock mass compression was also neglected.

As for the creep behavior simulation method using particle discrete method, Zhao Z and Song E compared three kinds of the bond-aging model which can simulate the stress corrosion process well: proposed by Tran et al. 2009 (Tran et al. 2009); proposed by Silvani et al. 2009 (Silvani et al. 2009); and proposed by Potyondy 2007 (Potyondy 2007). The compared results are as shown in Fig. 1-5.

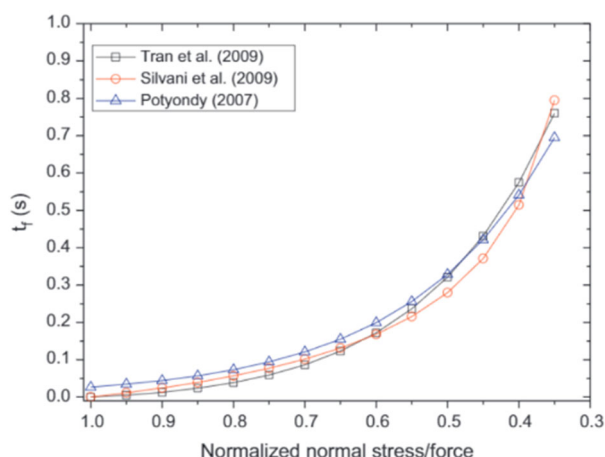


Fig. 1-5 Comparison of elapsed time to bond failure between three bond-aging models (Zhao and Song 2015)

As shown in Fig. 1-5, the trend of the normalized normal stress was almost the same, indicating that all these three bond-aging models can be used to simulate rock mass creep with appropriate empirical parameters.

However, it is difficult to simulate the real rotation and occlusion behavior between complex 3D particles by a two-dimension numerical model (Wang et al.2018; Zhao and Song 2015; Ma et al. 2019; Zhang et al.2020). A 3D numerical model is necessary to be built. In addition, the deformation and damage inside the rock fragmentation and the time effect of bulking coefficient were practically not considered in the existing 3D numerical simulation study of the broken rock mechanical behavior (Huang et al. 2017; Li et al. 2020).

1.2.4 Prediction methods of surface subsidence

With the further understanding and mastery of mining subsidence in the coal mine, especially the spatial and temporal laws of surface movement, many mining subsidence prediction theories and methods have been established (He 2013).

Section function method: Using mathematical and physical methods, different functions were selected to analyze the rock layer movement and surface settlement caused by mining. The expressions of rock layer movement and surface settlement under different mining conditions were obtained, and the deformation prediction

calculation method were analyzed. Finally, the mining section function for subsidence prediction was gradually formed.

Scholars have conducted a lot of researches in section function method, and successively proposed the Donez section function method (see Eq. (1-2)), Budryk-knothe section function method (see Eq. (1-3)), negative exponential function method (see Eq. (1-4)) and other research methods, which greatly enriched and developed the section function method for mining surface subsidence prediction.

$$W(x) = W_{\max} \left(1 - \frac{x}{L} + \frac{1}{2\pi} \sin 2\pi \frac{x}{L} \right) \quad (1-2)$$

$$W(x) = W_{\max} \int_x^\infty e^{-\pi \frac{x^2}{r^2}} dx \quad (1-3)$$

$$W(x) = W_{\max} \int_x^\infty e^{-a \left(\frac{b-x}{H} \right)^n} dx \quad (1-4)$$

where W_{\max} is the max value of the overburden subsidence; x is the surface distance from the central point of the sinking basin to the calculated point. L is the half length of the sinking basin; a , b and n are the undetermined coefficients; r is the main influence radius, $r = H_0/\tan \gamma$; H_0 is the average mining depth; γ is the mining influence angle; $\tan \gamma$ is the tangent of main influence angle; H is the depth of mining. These parameters are described in Fig. 1-6.

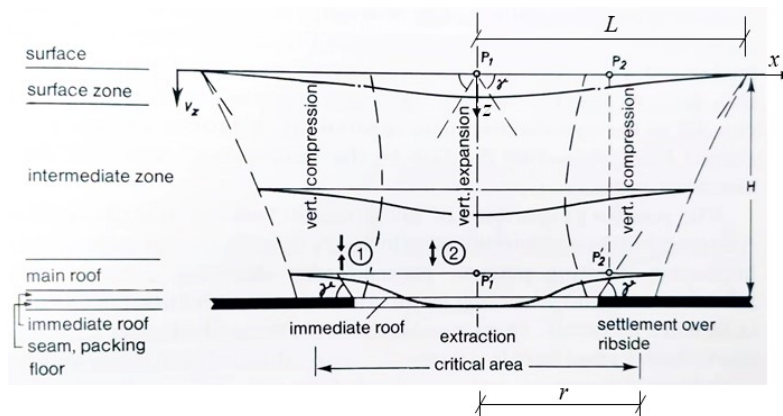


Fig. 1-6 Vertical deformation of an undermined rock mass in flat-lying measures

(Kratzsch 1986)

Influence function method: The influence function method is a method between the empirical method and the theoretical method. It has high accuracy and is more convenient for the surface movement calculation caused by the mining of ore bodies with complex conditions. An influence function is used to describe the amount by which an underground extraction affects the surface. Assuming an infinitesimal element dA at depth H to be extracted, it will create an elementary trough at the surface; the deepest point of the trough is vertically over the extraction element dA , and the trough decreases towards the limit line. The amount of subsidence at an arbitrary point in the trough varies according to its position, and consequently, the subsidence can be stated as a function $f(x)$ of the position of point P by means of either radial distance from the trough central point. To describe the parameters clearly, Fig. 1-7 shows the schematic diagram of influence function calculation.

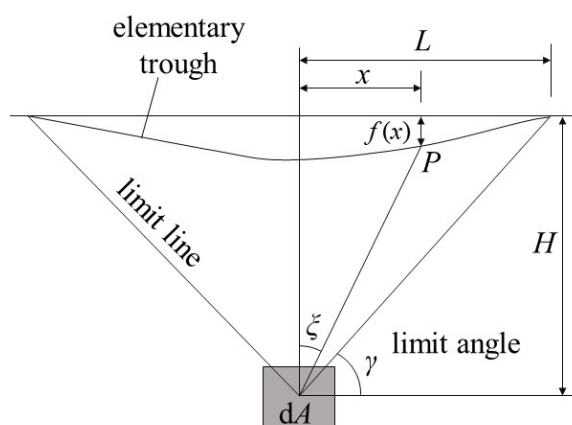


Fig. 1-7 Schematic diagram of influence function calculation

The basic principle of the influence function method is that it is assumed that the influence of the opening of a small underground unit on any point on the surface is related to the horizontal distance between the surface and the unit. The basic concept of the influence function method is the influence angle and the full mining degree or range determined by the influence angle, which is the so-called influence radius, are used to describe the influence of mining.

J. Litwiniszyn used mathematical statistics to establish the expression of the

overlying strata and surface movement of the mined-out area, thus laying the theoretical foundation of the influence function (Salamon 1974):

$$f(x) = W_{\max} \frac{1}{r^2} e^{-\frac{\pi x^2}{r^2}} \quad (1-5)$$

Brauner et al. proposed the circular integral grid method to calculate the surface movement when studying the movement of the overburden and the surface settlement during the mining process (Brauner 1973).

$$f(x) = W_{\max} \frac{2}{\sqrt{\pi^3}} e^{-\frac{4x^2}{r^2}} \quad (1-6)$$

Another scholars, such as Ehrhardt-Sauer, Beyer, Koehmanski, Kothe, Sauer and so on have successively developed and proposed some new influence function theories and methods based on the previous research results, which have improved and enriched mining subsidence (He 2013).

Probability Integral Method: This approach is currently commonly utilized in the prediction of mining subsidence. The rock mass analyzed in mining subsidence is treated as a non-continuum model in this manner, comparable to granulosis medium (Li et al. 2011). The subsidence of any surface point (x, y) induced by mining can be represented as follows using the probability integral method (Fan et al. 2014; He et al. 1991)

$$\left\{ \begin{array}{l} W(x, y) = mq \cos \alpha \iint W_{eoi}(x, y) dx dy \\ W_{eoi}(x, y) = \frac{1}{r^2} \exp\left(\frac{-\pi(x-x_i)^2}{r^2}\right) \cdot \exp\left(\frac{-\pi(y-y_i + H_i \text{ctg} \gamma)^2}{r^2}\right) \end{array} \right. \quad (1-7)$$

where m is the mining height; q is the subsidence coefficient; α is the angle of dip of the coal strata; (x_i, y_i) is the plane coordinate of mining unit i ; (x, y) is the coordinate of any surface point.

The probability integral method can effectively predict mining surface subsidence, and the major predictive parameters need be inferred from a large number of mining

subsidence data generally.

Although these research methods are important for a macroscopic understanding of the dynamic law of subsidence and deformation, they only qualitatively or quantitatively describe the movement of the overburden caused by underground opening and the geometric characteristics of the surface subsidence basin. It cannot objectively reflect the essential characteristics of mining subsidence because it ignores the influence of the structural and mechanical properties of the rock strata on mining subsidence, and it must be combined with other research methods to comprehensively analyze the essential characteristics of mining subsidence.

1.3 Contents of research

This dissertation consists of seven chapters and the main contents in each chapter are listed as follows:

Chapter 1: This chapter introduced the research background and significance of prediction of the long-term behavior of the caving zone in order to predict long-term surface subsidence due to the long wall coal mining operation. The reviews of the literatures on the measurement technology and prediction of surface subsidence and ground behavior were also presented in this chapter. This chapter describes the objectives of this research.

Chapter 2: The chapter describes the BOTDR technology for measurement of ground movement due to longwall coal mining operation. As the BOTDR technology can measure the strain at specific monitoring point, the returned strain may be somewhat different from the rock mass surrounding the monitoring point. Hence, it can be expected that a large cumulative error may occur if the strain measured by BOTDR technology at the monitoring point is considered as the same as overall deformation of the rock mass, especially in caving zone and damage zone. The new calculation model which can calculate the ground deformation above gab can be calculated from the data measured by BOTDR technology is proposed. In this model, the ground above goaf is

divided into three zones: caving zone, damage zone and continuous deformation zone then the constitutive model of each zone is developed. The caving zone represents as a constitutive model of broken rock mass. The deformation of this model contains the compressive deformation of rock body and the sliding behavior of rock particles. The damage zone represents the fractures zones as an elastoplastic body. The continuous deformation zone represents the elastic deformation zone and unconsolidated zone which can be modeled as the elastic body. The value of surface subsidence above goaf can be calculated by the summation of deformation of each zone.

Chapter 3: In order to discuss the applicability of BOTDR Technology and identify the technical issues to be solved for measurement and prediction of long-term behavior of ground movement and surface subsidence due to longwall coal mining extraction, the field investigation was conducted in Zhangzhuang coal mine, Anhui Province, China. Based on the measurement data, it was confirmed that the overburden can be classified into four zone: unconsolidated zone, bending zone, fractures zone and caving zone depend on the movement behavior. It can be seen that the strain in the caving zone increases with increasing the time elapsed after extraction of longwall panel obviously. Besides, the settlement rate of caving zone also increases with increasing the elapsed time after extraction of longwall panel though and continuous the settlement rate of caving zone also increases with increasing the elapsed time even though the settlement rates of fracture zone and continuous zone such as unconsolidated and bending zones increase gradually in the beginning and then are stable. Therefore, it can be said that the behavior of caving zone has an obvious impact on the long-term ground behavior and subsidence due to the longwall mining extraction. Moreover, comparing with the measurement data of the surface subsidence, the subsidence calculation model proposed by Chapter 2 is more suitable method for prediction of surface subsidence in comparison to the conventional strain integral method but there is still about 10 % error between the calculated value based on the strain data by BOTDR Technology and field monitoring data of surface subsidence. It can be thought that this is because the long-term behavior of caving zone is not considered and

implemented in the calculation model. From these results, it can be concluded that the long-term deformation mechanism and behavior of caving zone have to be made clear in order to predict long-term surface subsidence due to the longwall coal extraction.

Chapter 4: In order to understand the long-term deformation behavior of caving zone, a series of the triaxial creep tests with broken rocks were conducted under different grading size of broken rocks, confining stress and axial stress. Based on the results of a series of the creep tests, it can be said that about 90% of the overall deformation of broken rocks was elastic deformation during an instantaneous stage and a stable deformation one. Both the axial stress and confining stress have an obvious impact on the creep behaviors of broken rocks, the period of stable stage increases with increasing the axial stress and the maximum creep value decreases with increasing the confining pressure. Moreover, it also can be seen that the breakage of rock pieces occurs during creep tests and this phenomenon has an obvious effect on the creep behavior of broken rocks. The relative breakage index, which was calculated by the total breakage divided by the breakage potential, was introduced in order to evaluate the breakage degree of rock pieces. The distribution of the size of broken rocks has an obvious impact on the breakage behavior of rock pieces and the breakage index is large value when the contents of large size rock pieces is large and that of small one is small. Besides, the breakage index decreases with increasing the confining pressure.

Chapter 5: As the bulking coefficient plays an important role for deformation behavior of caving zone. In order to understand the long-term deformation behavior and determine/characteristics of the bulking coefficient of broken rocks, a three-dimensional numerical model to represent the block contents broken rocks was developed and applied for a series of numerical simulations. In this simulation, the damage criterion of the rock fragmentation by particle discrete element was also implemented in this model. Based on the results of a series of numerical simulations, the deformation behavior for long period can be made clear as follows. The broken rock was in compaction stage at the initial triaxial compression loading period, and the

bulking coefficient decreased with a certain fluctuation. Besides, the fluctuation behavior of deformation increases with the decrease of the confining pressure and the increase of the axial pressure. After that, the deformation of broken rocks turns into the viscoelastic deformation stage, the bulking coefficient gradually monotonously decreased with the elapsed time and the rock block could be easily damaged at the protruding edge. From the results of a series of numerical simulations, it can be concluded that the creep behaviour of broken rocks can be simulated by Burgers creep model and the model for prediction of bulking coefficient was proposed.

Chapter 6: In this chapter, a new the creep model based on the fractional order theory is proposed in order to predict short and long-term behavior of caving zone consisted by broken rocks. Compared with the result of the triaxial compressive experiment with using broken rocks, it can be said that the new creep model can simulate the behavior of the specimen with broken rocks with the 0.995 accuracy and better than the classic Burgers model. Moreover, the prediction equation for caving zone behavior is developed based on this new creep model. Compared with the field measurement date of caving zone deformation, it can be said that the new prediction equation can predict the long-term behavior caving zone with the accuracy of 0.997.

Chapter 7: This chapter summarized and concluded the results and findings of this study.

The flow chart of this study is shown in Fig. 1-8.

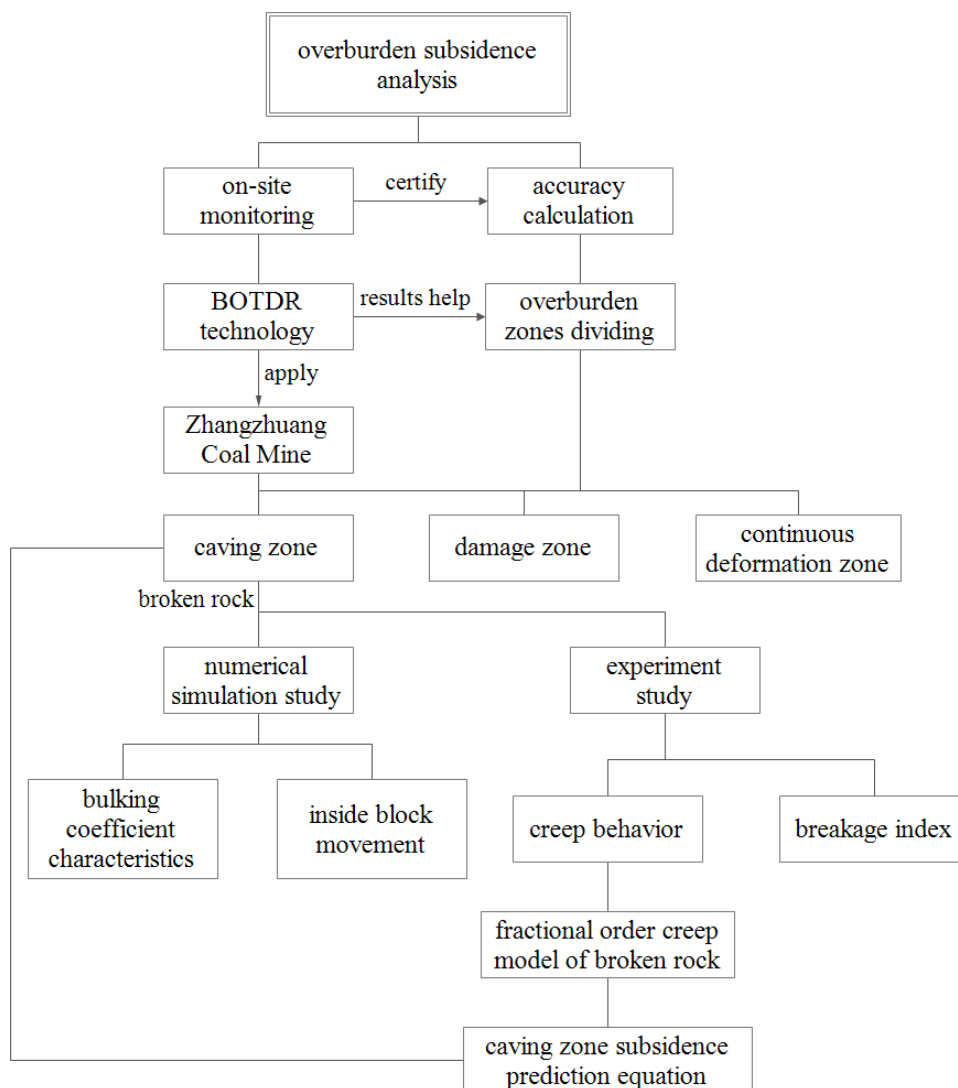


Fig. 1-8 Flow chart of the research contents and approaches

References

- Braimer G. Subsidence due to underground mining. Bureau of Mines, USA, 1973.
- Can E, Kuşçu Ş, Mekik C. Determination of underground mining induced displacements using GPS observations in Zonguldak-Kozlu Hard Coal Basin. *Int J Coal Geol.* 2012;89:62-69.
- Chrzanowski A, Monahan C, Roulston B, et al. Integrated monitoring and modelling of ground subsidence in potash mines. *Int J Rock Mech Min Sci.* 1997;34(3-4):55.
- Donnelly LJ. A review of international cases of fault reactivation during mining subsidence and fluid abstraction. *Q J Eng Geol.* 2009;42(1):73–94.
- Fan H, Wei G, Yong Q, et al. A model for extracting large deformation mining subsidence using D-InSAR technique and probability integral method. *Transactions of Nonferrous Metals Society of China*, 2014, 24(4): 1242-1247.
- Fan L, Liu S. A conceptual model to characterize and model compaction behavior and permeability evolution of broken rock mass in coal mine gobs. *International Journal of Coal Geology* 2017;172:60-70.
- Feng G, Wang P. Simulation of recovery of upper remnant coal pillar while mining the ultra-close lower panel using longwall top coal caving. *International Journal of Mining Science and Technology* 2020;30(1):55-61.
- Firme PALP, Roehl D, Romanel C. An assessment of the creep behaviour of Brazilian salt rocks using the multi-mechanism deformation model. *Acta Geotechnica* 2016;11(6):1445-1463.
- Gang C, Shi B, Zhu HH, et al. A field study on distributed fiber optic deformation monitoring of overlying strata during coal mining. *J. Civ. Struct. Health Monit.* 2015; 5:553–562.
- Gu'eguen Y, Deffontaines B, Fruneau B, et al. Monitoring residual mining subsidence of Nord/Pas-de-Calais coal basin from differential and Persistent Scatterer Interferometry (Northern France). *J Appl Geophys.* 2009;69:24–34.
- Hao S, Shuguang J, Lanyun W, Zhengyan W. Bulking factor of the strata overlying the gob and a three-dimensional numerical simulation of the air leakage flow field. *International Journal of Mining Science and Technology* 2011;21(2):261-266.
- He Guoqing, Yang Lun, Ling Gengdi, et al. Mining subsidence. Xuzhou: China University of
-

- Mining and Technology Press 1991. (in Chinese)
- He Guicheng. Investigation into prediction and control of mining subsidence of the gently inclined bedded ore body. Doctoral thesis 2013. (in Chinese)
- Hohmann GW, Ward SH. Electrical methods in mining geophysics. *Econ Geol.* 1981; 75:806–828.
- Hong CY, Zhang YF, et al. Recent progress of using Brillouin distributed fiber optic sensors for geotechnical health monitoring. *Sens. Actuator A Phys.* 2017;258: 131–145.
- Huang YL, Li JM, Teng YC, Dong XJ, Wang X, Kong GQ, et al. Numerical simulation study on macroscopic mechanical behaviors and micro-motion characteristics of gangues under triaxial compression. *Powder Technology* 2017;320:668-684.
- Hufenus R, Rueegger R, Banjac R, et al. Full-scale field tests on geosynthetic reinforced unpaved roads on soft subgrade. *Geotextiles and Geomembranes.* 2006,24(1):21-37.
- International Energy Agency (IEA). *Coal 2020 – Analysis and forecast to 2025.* <https://www.iea.org/reports/coal-2020>. December 2020.
- Jung HC, Kim SW, Jung HS, et al. Satellite observation of coal mining subsidence by persistent scatterer analysis. *Eng Geol.* 2007;92:1–13.
- Kabwe E, Karakus M, Chanda EK. Time-dependent solution for non-circular tunnels considering the elasto-viscoplastic rockmass. *International Journal of Rock Mechanics and Mining Sciences* 2020;133:104395.
- Kratzsch H. Mining subsidence engineering. *Environmental Geology and Water Sciences* 1986,8(3):133-136.
- Kies A, Storoni A, Tosheva Z, et al. Radon measurements as a monitoring possibility for mining subsidence occurrence. *J Min Sci.* 2006;42(5):518–522.
- Li PX, Tan ZX, Deng KZ. Calculation of maximum ground movement and deformation caused by mining. *Transactions of Nonferrous Metals Society of China*, 2011, 21(s3): s562-s569.
- Li M, Li A, Zhang J, Huang Y, Li J. Effects of particle sizes on compressive deformation and particle breakage of gangue used for coal mine goaf backfill. *Powder Technology* 2020;360:493-502.
- Li M, Zhang JX, Meng GH, Gao Y, Li AL. Testing and modelling creep compression of waste
-

-
- rocks for backfill with different lithologies. *International Journal of Rock Mechanics and Minings Sciences* 2020;125:104170.
- Liu S, Wan Z, Zhang Y, Lu S, Ta X, Wu Z. Research on evaluation and control technology of coal pillar stability based on the fracture digitization method. *Measurement* 2020:107713.
- Li S, Fan CJ, Luo MK, et al. Structure and deformation measurements of shallow overburden during top coal caving longwall mining. *Int. J. Min. Sci. Technol.* 2017;27 (6):1081–1085.
- Li S, Zhang Q, Chen Z. Experimental study of compaction creep model of broken rock. *Journal of Mining World Express Volume*, 2013, 2(4).
- Madjdabadi B, Valley B, Dusseault MB, et al. Experimental evaluation of a distributed Brillouin sensing system for detection of relative movement of rock blocks in underground mining. *Int J Rock Mech Min Sci.* 2017;93:138–151.
- Ma Z, Gu R, Huang Z, Peng G, Zhang L, Ma D. Experimental study on creep behavior of saturated disaggregated sandstone. *International Journal of Rock Mechanics and Minings Sciences* 2014;66:76-83.
- Ma Z, Zhang M, Cheng S, Hu J, Su Y, Chen Y. The mechanism of fractured sandstone in compaction creep process. *Thermal Science* 2019;23:S989-S995.
- Marsal R J. Large scale testing of rockfill materials. *Journal of the Soil Mechanics and Foundations Division*, 1967, 93(2): 27-43.
- O'Connor KM, Murphy EW. TDR monitoring as a component of subsidence risk assessment over abandoned mines. *Int J Rock Mech Min Sci.* 1997;34(3-4):230.
- Ohno H, Naruse H, Kihara M, et al. Industrial applications of the BOTDR optical fiber strain sensor. *Opt Fiber Technol.* 2001;7(1):45–64.
- Palchik V. Bulking factors and extents of caved zones in weathered overburden of shallow abandoned underground workings. *International Journal of Rock Mechanics and Minings Sciences* 2015;79:227-240
- Potyondy DO. Simulating stress corrosion with a bonded-particle model for rock. *International Journal of Rock Mechanics and Mining Sciences* 2007;44(5):677-691.
- Salamon M D G. *Rock mechanics of underground excavations.* 1974.
- Shihao T U, Cun Z, Guanyu Y, et al. Research on permeability evolution law of goaf and
-

-
- pressure-relief mining effect. *Journal of Mining and Safety Engineering*, 2016, 33(4): 571.
- Silvani C, Désoyer T, Bonelli S. Discrete modelling of time - dependent rockfill behaviour. *International Journal for Numerical and Analytical Methods in Geomechanics* 2009;33(5):665-685.
- Sun CL, Li GC, Gomah M E, Xu JH, Sun YT. Creep characteristics of coal and rock investigated by nanoindentation. *International Journal of Mining Science and Technology* 2020;30(6):769-776.
- Sun Y, Zhang P, Yan W, Yan F, Wu J. Compressive deformation characteristics of crushed sandstone based on multiple experimental factors. *Archives of Mining Sciences* 2020;65(1):129-146.
- Tran T-H, Vénier R, Cambou B. Discrete modelling of rock-ageing in rockfill dams. *Computers and Geotechnics* 2009;36(1-2):264-275.
- Wang JH. Development and prospect on fully mechanized mining in Chinese coal mines. *Int. J. Coal Sci. Technol.* 2014;1(3):253–260.
- Wang Y, Song E, Zhao Z. Particle mechanics modeling of the effect of aggregate shape on creep of durable rockfills. *Computers and Geotechnics* 2018;98:114-131.
- Yang ZF, Li ZW, Zhu JJ, et al. Deriving dynamic subsidence of coal mining areas using InSAR and logistic model. *Rem Sens.* 2017;9(2):125.
- Yasar E, Erdogan Y. Correlating sound velocity with the density, compressive strength and Young's modulus of carbonate rocks. *Int J Rock Mech Min Sci.* 2004;41 (5):871–875.
- Zhang C, Ren Z, Hao D, Zhang T. Numerical Simulation of Particle Size Influence on the Breakage Mechanism of Broken Coal. *Arabian Journal for Science and Engineering* 2020:1-15
- Zhang C, Shi B, Gu K, et al. Vertically distributed sensing of deformation using fiber optic sensing. *Geophys Res Lett.* 2018;45(21):732–741.
- Zhang C, Tu S, Zhang L, et al. A methodology for determining the evolution law of gob permeability and its distributions in longwall coal mines. *Journal of Geophysics and Engineering*, 2016, 13(2): 181-193.
- Zhang C, Tu S, Zhao Y. Compaction characteristics of the caving zone in a longwall goaf: a
-

review. *Environmental Earth Sciences* 2019;78(1).

Zhang D, Wang JC, Zhang PS, et al. Internal strain monitoring for coal mining similarity model based on distributed fiber optical sensing. *Measurement*. 2017;97: 234–241.

Zhang GX, Lei ZQ, Cheng H. Shear creep simulation of structural plane of rock mass based on discontinuous deformation analysis. *Mathematical Problems in Engineering* 2017;e1582825.

Zhang Q B, Zhao J. A review of dynamic experimental techniques and mechanical behaviour of rock materials. *Rock mechanics and rock engineering*, 2014, 47(4): 1411-1478.

Zhao Z, Song E-x. Particle mechanics modeling of creep behavior of rockfill materials under dry and wet conditions. *Computers and Geotechnics* 2015;68:137-146.

CHAPTER 2

2 Measurement of ground behavior due to longwall mining operation by using BOTDR technology

With the increase of the coal consumption, the longwall mining goaf scale has become significantly large, increasing the risk of subsidence. Distributed optical fiber sensor can obtain the strain and temperature distribution information of measurand fields along the fiber path in time and space simultaneously and it can realize long-term monitoring of structures (Zhang et al. 2018; Hong et al. 2017). Hence, optical fiber sensor based on Brillouin optical time-domain reflectometer (BOTDR) technology was adopted in order to measure the overburden deformation behavior due to longwall mining operation after mining in this research.

2.1 Introduction of BOTDR technology

BOTDR is the distributed optical fiber sensing technology which based on Brillouin optical time domain reflectometry (Gao et al. 2019; Weng et al. 2015; Fabien et al. 2007).

Its working principle is (Gao et al. 2019; Shi 2006): a continuous light of a certain frequency from the DFB-LD (distributed feedback laser diode) laser light source is injected into the optical fiber medium, this light can be separated into the probe light to the output to the optical fiber to be measured and the reference light for heterodyne detection. The probe light can be modulated into the pulse light by an intensity modulator. When the pulse light entering the inside of the optical fiber, it interacts with the elastic acoustic wave therein to generate back Brillouin scattering, which causes Brillouin scattering due to the temperature and the stress received. Brillouin scattering occurs in the optical fiber, and the Brillouin backlight generates a frequency shift. The frequency shift amount is in proportion to the longitudinal strain of the optical fiber. By measuring the frequency shift, the relationship of the frequency shift with the

temperature and strain of the optical fiber can be used to obtain the external information of the optical fiber. When one end of the optical fiber receives the pulsed light of the specified frequency, the pulsed light interacts with the elastic acoustic wave in the optical fiber to form Brillouin scattering, then the back Brillouin scattered light returns through the original path of the optical fiber and enters the BOTDR light receiving part and the signal processing unit. The conversion of the optical signal and electrical signal is completed in the receiving part, the electrical signal is transmitted to the receiver through the broadband amplifier. The digital signal processor is used to perform the average processing, the specific distribution of Brillouin scattering light power in each sampling point of the fiber is obtained. The diagram of BOTDR is shown in Fig. 2-1 (Shi et al. 2006).

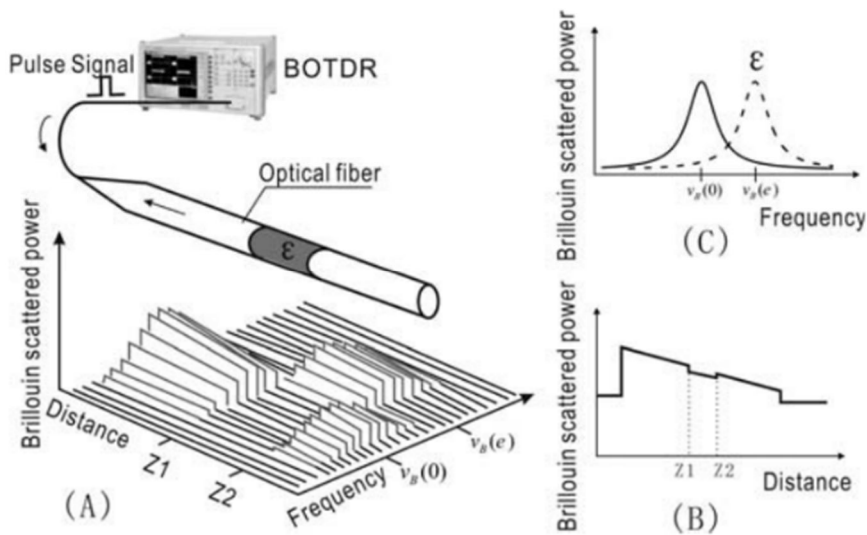


Fig. 2-1 Diagram of BOTDR monitoring principle (Shi et al. 2006)

Both the temperature and strain have linear relationship between the frequency shift of Brillouin scattered light. From the monitoring frequency shift of Brillouin scattered light, the temperature and strain of the monitored material can be measured by BOTDR technology. The relationship of Brillouin frequency shift with temperature and strain is shown in Eq. (2-1) (Gao et al. 2019; Sakairi et al. 2002; Horiguchi et al. 1995; Hong 2017; Klar 2014)

$$\Delta \nu_B(\varepsilon, T) = \frac{\partial \nu_B(\varepsilon)}{\partial \varepsilon} \Delta \varepsilon + \frac{\partial \nu_B(T)}{\partial T} \Delta T \quad (2-1)$$

where, $\Delta v_B(\varepsilon, T)$ is the amount of Brillouin frequency shift change, related to temperature and strain; $\frac{\partial v_B(\varepsilon)}{\partial \varepsilon}$ is the strain coefficient of change; $\Delta \varepsilon$ is the amount of the strain change of the optical fiber; $\frac{\partial v_B(T)}{\partial T}$ is the temperature coefficient of change; ΔT is the amount of the temperature change of the optical fiber.

The strain and temperature coefficients of change $\frac{\partial v_B(\varepsilon)}{\partial \varepsilon}$ and $\frac{\partial v_B(T)}{\partial T}$ are coefficients which is related to the optical fiber's properties and stay unchanged if the optical fiber sensor is fixed. In that case, both of coefficients can be obtained from a laboratory monitoring experiment. In Eq. (2-1), $\Delta v_B(\varepsilon, T)$ can be monitored by the optical fiber sensor. Then, during a mechanical test by the optical fiber sensor, if the temperature change value ΔT is known, it will be easy to obtain the value of strain change.

2.2 Calculation model of overburden subsidence based on BOTDR technology

2.2.1 Simplify

(1) *Division of different zones of overburden*

According to the characteristics of the rock mass in the overburden after excavation, the strata can be generally divided into three parts caving zone, fractured zone, bending zone and unconsolidated layers (Peng 1992). The rock mass in the caving zone is completely broken and filled with rock blocks, which contributes most to the surface subsidence above the goaf. The rock mass in the fractured zone is full of fully developed fractures. While the rock mass of the bending zone has good integrity and is divided into a microseismic active area and an elastic deformation area based on the rock deformation state (Shabanimashcool 2012). The microseismic active area is in direct contact with the fractured zone and contains rock fractures and other types of damage; therefore, the damage factor can be used to represent the fracture development state in the microseismic active area. The elastic deformation area is under the elastic deformation stage in the bending zone. The unconsolidated layers are comprised of the

rock and soil, and it can be assumed that only elastic deformation occurred like the elastic deformation area in the bending zone.

For the convenience of the subsidence calculation model derivation, the overburden was divided into three new parts according to the state and deformation characteristics of overlying rock and soil above the goaf, that is, caving zone based on the broken rock mass, damage zone (fracture zone and microseismic active area) based on the fractured rock mass, and continuous deformation zone (elastic deformation area and unconsolidated layers) based on continuous rock mass. The schematic diagram of overburden deformation zones in coal seam is shown in Fig. 2-2.

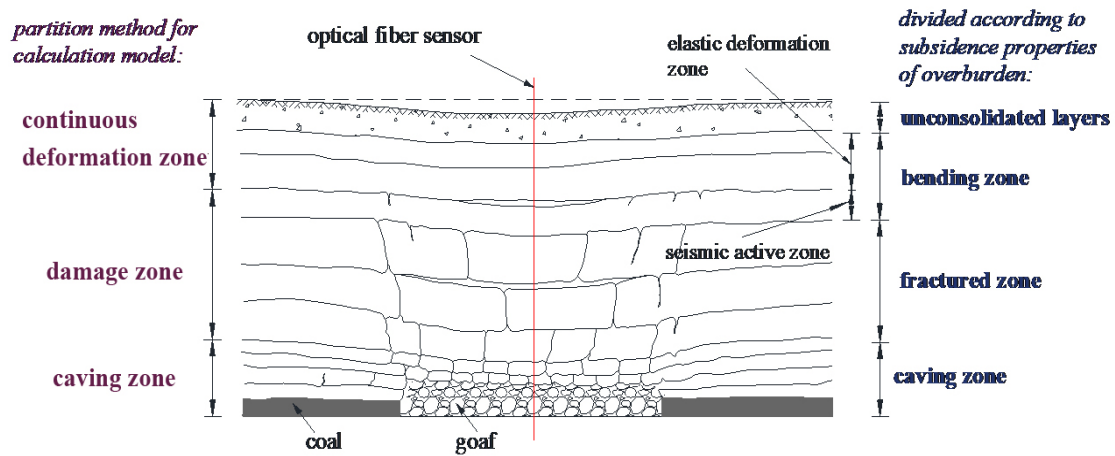


Fig. 2-2 Diagram of mining overburden state and stratum zoning

The red line in Fig. 2-2 is an example of the optical fiber strain sensor's layout in overburden. It is noted that the strain data of overburden by optical fiber strain sensor is in one direction along the optical fiber. If we lay a vertically oriented fiber within the overburden of the goaf, then it is reasonable to assume that the strain data returned by the fiber is vertical strain (Zhang et al. 2018).

(2) Distributed monitoring scheme for overburden in the goaf

To explain the basis of the simplified calculated model clearly, a brief description of the optical fiber monitoring scheme in the mining overburden is necessary: first drill a hole into the ground along the goaf of the coal mine, implant an optical cable made of glass fiber reinforced plastics (GFRP) into the borehole slowly, and then pour

concrete grout into the hole to seal. In order to ensure the filling back material concrete grout deforms together with the surrounding rock, it is better that the elastic modulus of filling material is larger than the surrounding rock (Zhang 2020). In addition, adopting a screw-like package design for an embeddable distributed optical fiber strain sensor also can improve the deformation coupling degree between them (Du 2018). The schematic diagram of the layout and monitoring of the optical fibre cable in the overburden is shown in Fig. 2-3.

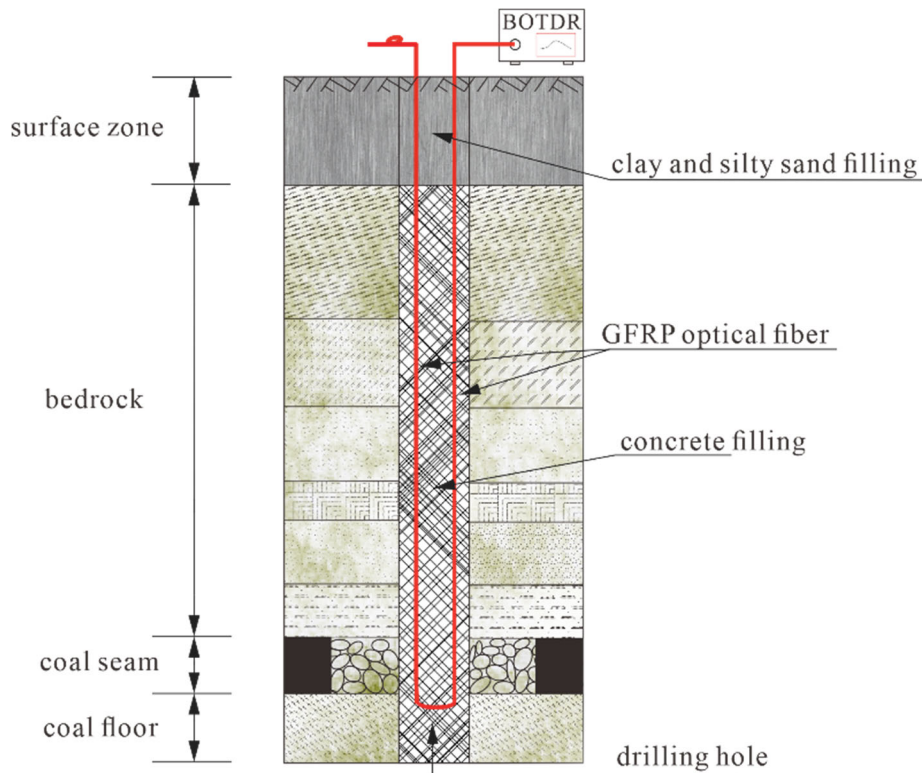


Fig. 2-3 Distributed monitoring scheme for overburden in mining area

(3) Assumptions of the overburden model for calculation

According to the principle of BOTDR, it can be considered that strain sensors are distributed every sampling interval along the fiber, and the interval is usually between 0.05m and 1m (Zhang et al. 2013; Zhang et al. 2019). Because of the existing of the void, cracks and other damage, the deformation of overburden, especially in caving zone and damage zone, is unevenly. As the optical fiber strain sensor monitors only at specific monitored points, the returned strain is somewhat different from the rock mass strain outside the monitoring point. When calculating the subsidence, it is required to

accumulate the strain within the height range. If the strain data returned from the monitoring point is considered the same as the overall deformation of the rock, a large cumulative error will occur. In this study, we use the strain outside the monitoring point ε_r and the strain at the monitoring point ε_m to distinguish these two kinds of strain.

The calculation model is simplified, as shown in Fig. 2-4, where λ is the spatial sampling interval.

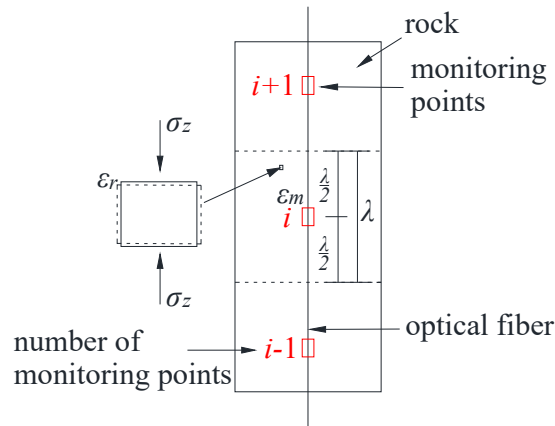


Fig. 2-4 Monitoring points of the optical fiber sensor

The strain outside the monitoring point i is considered as the average strain of one spatial resolution λ as shown in Fig. 2-4.

The interaction between the optical fiber and the monitored rock has been studied by many researches (Zhang et al. 2020; Zang et al. 2015; Zhang et al. 2016), and to simply the model, it is assumed that the data returned from optical fiber sensor is the rock mass strain at the monitoring point. To get a general calculated method, the other following assumptions also need be claimed.

- The strain returned by the optical fiber sensor is vertically.
- The monitored rock mass, filling material and optical fiber deform together.
- The stress near each monitoring point is equal.
- When implanting the optical fiber, the mine below the drilling hole was excavated.

2.2.2 Subsidence calculation model of rock mass in caving zone

As shown in the Subsection 2.2.1, the strain at the monitoring point and the strain of the whole rock mass should be calculated separately.

A constitutive model of broken rock mass was adopted to reflect the stress-strain relationship of the rock mass at the strain monitoring point (Ryder 1978; Salamon 1990):

$$\sigma_z^b = \frac{E \varepsilon_m^b}{1 - \varepsilon_m^b / \varepsilon_{\max}} \quad (2-2)$$

where σ_z^b is the vertical strain of rock mass in the caving zone; E is the elastic modulus of rock mass; ε_m^b is the strain at the monitoring point in the caving zone; ε_{\max} is the maximum strain of the rock mass along the vertical direction.

The maximum strain can be calculated as (Yavuz 2004; Zhang 2019):

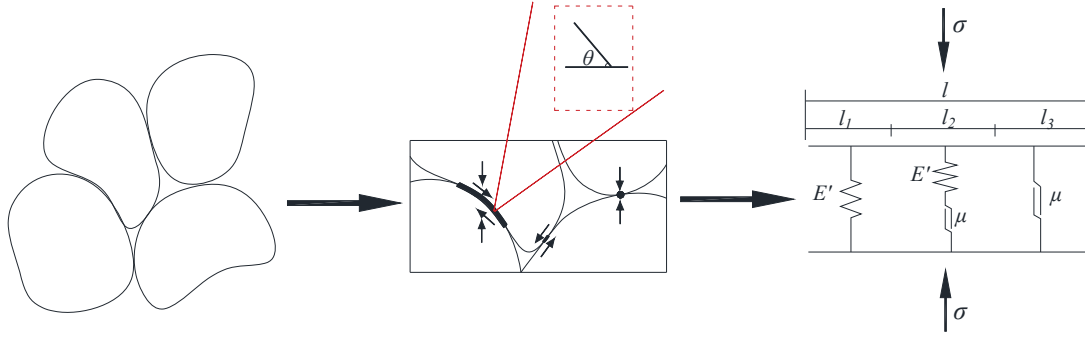
$$\varepsilon_{\max} = 1 - \frac{1}{K_0} \quad (2-3)$$

where K_0 is the initial bulking coefficient.

Since the coal mine was excavated and the rock mass has been broken, the deformation in caving zone has two main forms: the compression deformation of the rock body itself and the volumetric compression of the rock mass void caused by arrangement and distribution changes of rock blocks. When the stress applied to the broken rock fragments cannot cause sliding deformation, the rock particles only undergo self-compressive deformation. When the stress is large enough to cause sliding friction between particles, sliding deformation among rock particles and self-compressive deformation of the rock mass would occur simultaneously or only sliding deformation. Compressive deformation of the broken rock mass can be represented by three kinds of components in a parallel form, as shown in Fig. 2-5.

Fig. 2-5 shows that the deformation of the broken rock mass can be simplified into

three forms: Component I. The compressive deformation of rock particles is simplified as an elastic element; Component II. When the deformation of the rock body and the sliding friction occur together, the deformation is then simplified as an elastic element and a friction plate which are connected in series; Component III. The sliding friction between the rock particles is simplified as a friction plate.



Broken rock particles → Particle contact types → Components simplified from contacts

Fig. 2-5 Schematic diagram of simplification of compressive deformation of the rock mass in the caving zone

The three components are connected in parallel, and the relationship of strain and stress with each contact form can be obtained:

$$\begin{cases} \sigma_z^b = \sigma_{E'} + \sigma_\mu \\ \varepsilon_r^b = \varepsilon_1 = \varepsilon_2 = \varepsilon_3 \end{cases} \quad (2-4)$$

where σ_z^b is vertical stress of the rock in the caving zone; $\sigma_{E'}$ is the total stress of the elastic element in component I and component II; σ_μ is the total stress of the sliding plate in component II and component III; ε_r^b is vertical strain of the rock in the caving zone; ε_1 is the strain applied to component I; ε_2 is the strain applied to component II; ε_3 is the strain applied to component III.

Since the elastic component of the model represents the rock block deformation, the damage influence needs to be considered. According to damage mechanics, the effective elastic modulus of each rock particle can be expressed by using the damage factor (Liu 2015):

$$E' = (1-D)E \quad (2-5)$$

where E' is the effective elastic modulus; D is the damage factor.

The stress applied to the elastic component and the friction plate in Fig. 2-5(c) can be calculated by:

$$\begin{cases} \sigma_{E'} = (1-D)E\varepsilon_r^b \\ \sigma_\mu = \frac{1}{2}\mu\sigma_z^b \sin(2\theta) \end{cases} \quad (2-6)$$

Where μ is the friction coefficient; θ is the angle between the tangent of the sliding friction surface and the horizontal direction (shown in Fig. 2-5(b)), named as the contact surface angle in the following discussion.

By substituting Eq. (2-6) into Eq. (2-4) and then into Eq. (2-2), the relationship between the vertical strain of the rock mass in the caving zone ε_r^b and the strain at monitoring points in the caving zone ε_m^b can be expressed by:

$$\varepsilon_r^b = \frac{\varphi(K_0 - 1)\varepsilon_m^b}{(1-D)[(1-\varepsilon_m^b)K_0 - 1]} \quad (2-7)$$

where $\varphi = 1 - \frac{1}{2}\mu\sin(2\theta)$, is the contact parameter of rock particles, and is related to the contact surface inclination and roughness.

The subsidence of the overburden rock mass including two parts: the compression of the rock mass itself which can be calculated by Eq. (2-7) and the displacement with the lower strata. Therefore, the subsidence of the caving zone can be obtained by adding all the strata deformation from the bottom of the caving zone to this certain depth. The formula for calculating the subsidence of overburden at height h_1 in the caving zone can be expressed by:

$$W_b(h_1) = \sum_{k=1}^n \frac{\lambda\varphi(K_0 - 1)\varepsilon_{mk}^b}{(1-D)[(1-\varepsilon_{mk}^b)K_0 - 1]} \quad (2-8)$$

where $W_b(h_1)$ is the subsidence of the rock mass in the caving zone when the overburden height is h_1 , and at this time h_1 falls within the height range of the caving zone; n is the maximum number of optical fiber sensor's monitoring points within height h_1 ; λ is the space sampling interval of the optical fiber sensor; ε_{mk}^b is the strain value monitored at the k^{th} monitoring point in the caving zone. In order to easy understand the parameters of the caving zone in Eq. (2-8), the schematic figure of the number of the monitoring points is shown in Fig. 2-6.

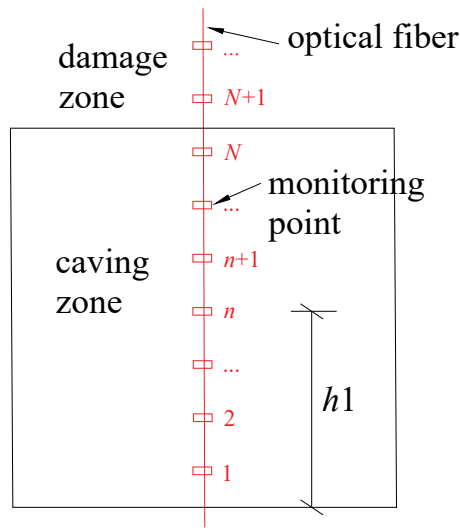


Fig. 2-6 Schematic of the monitoring points number method of caving zone

2.2.3 Subsidence calculation model of rock mass in damage zone

The same as caving zone, because of the uneven deformation, the strain at the monitoring point and the strain of the rock mass at the damage zone should calculate separately. The rock strain at the monitoring point is considered as elastoplastic strain, then it can be calculated by:

$$\varepsilon_m^d = \varepsilon_z^e + \varepsilon_z^p \quad (2-9)$$

where ε_m^d is the strain at the morning point in the damage zone; ε_z^e is vertical elastic strain of the rock mass at the monitoring point; ε_z^p is vertical plastic strain of the rock mass at the monitoring point.

Assuming that the deformation of the rock mass in the damage zone conforms to plastic total deformation theory, Eq. (2-9) can be rewritten as:

$$\varepsilon_m^d - \varepsilon_z^e = \frac{\varepsilon_i}{\sigma_i} \left[\sigma_z^d - \frac{1}{2}(\sigma_x^d + \sigma_y^d) \right] \quad (2-10)$$

where σ_i is the stress strength; ε_i is the plastic strain strength; σ_x^d , σ_y^d and σ_z^d are the stress of rock mass in the damage zone at x , y , and z direction, respectively.

Elastic strain in Eq. (2-10) of the rock mass in the damage zone can be expressed by:

$$\varepsilon_z^e = \frac{1}{E} \left[\sigma_z^d - \frac{1}{2}(\sigma_x^d + \sigma_y^d) \right] \quad (2-11)$$

When damage occurs at the rock mass due to cracks, pores and other structures, the rock mass strain can be expressed by the constitutive equation of the damaged rock:

$$\varepsilon_r^d = \frac{1}{(1-D)E} \left[\sigma_z^d - \frac{1}{2}(\sigma_x^d + \sigma_y^d) \right] \quad (2-12)$$

where ε_r^d is the vertical strain in the damage zone.

By combining Eq. (2-10), Eq. (2-11), and Eq. (2-12), the relationship between the rock mass strain ε_r^d and the strain at the monitoring point ε_m^d can be expressed by:

$$\varepsilon_r^d = \frac{\sigma_i}{(1-D)(E\varepsilon_i + \sigma_i)} \varepsilon_m^d \quad (2-13)$$

The same as caving zone, according to Eq. (2-13), the model for calculating the subsidence of the rock at height h_2 in the damage zone can be expressed by:

$$W_d(h_2) = W_b + \sum_{k=N+1}^m \frac{\lambda \sigma_i}{(1-D)(E\varepsilon_i + \sigma_i)} \varepsilon_{mk}^d \quad (2-14)$$

where $W_d(h_2)$ is overburden subsidence in the damage zone when the overburden height is h_2 , and h_2 falls within the height range of the damage zone; W_b is total subsidence of the caving zone, which can be calculated by Eq. (2-8); N is the total number of

monitoring points in the caving zone; m is the maximum number of optical fiber sensor's monitoring points within height h_2 ; ε_{mk}^d is the strain value monitored at the k^{th} monitoring point in the damage zone. The same as caving zone, in order to easy understand the parameters in the damage zone of Eq. (2-14), the schematic figure of the number of the monitoring points is shown in Fig. 2-7.

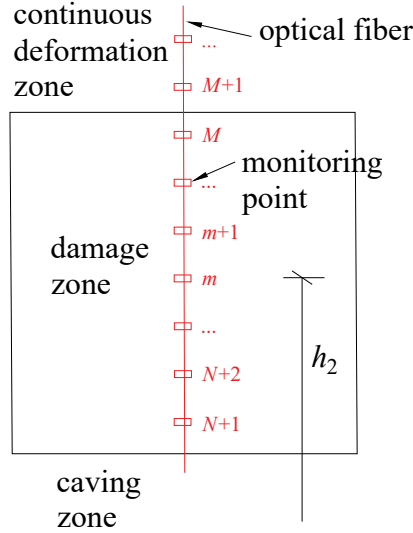


Fig. 2-7 Schematic of the monitoring points number method of damage zone

2.2.4 Subsidence calculation model of rock mass in the continuous deformation zone

Because the rock-soil body in elastic deformation zone and unconsolidated layers are assumed to be elastic body, the deformation in continuous deformation zone is homogeneous. In that case, the strain can reflect that of the whole rock mass in continuous deformation zone. The model for calculating the subsidence at height h_3 in the continuous deformation zone can be expressed by:

$$W_c(h_3) = W_b + W_d + \sum_{k=M+1}^p \lambda \varepsilon_{mk}^c \quad (2-15)$$

where $W_c(h_3)$ is overburden subsidence in the continuous deformation zone when the overburden height is h_3 , and h_3 falls within the height range of the continuous deformation zone; W_d is the total subsidence of the damage zone, which can be calculated by Eq. (2-14); M is the total number of monitoring points in the caving zone

and damage zone; p is the maximum number of monitoring points in the continuous deformation zone when the overburden height is h_3 ; ε_{mk}^c is the strain at the monitoring point in continuous deformation zone at the k^{th} monitoring point. The same as caving zone and damage zone, in order to easy understand the parameters in the continuous deformation zone of Eq. (2-15), the schematic figure of the number of the monitoring points is shown in Fig. 2-8.

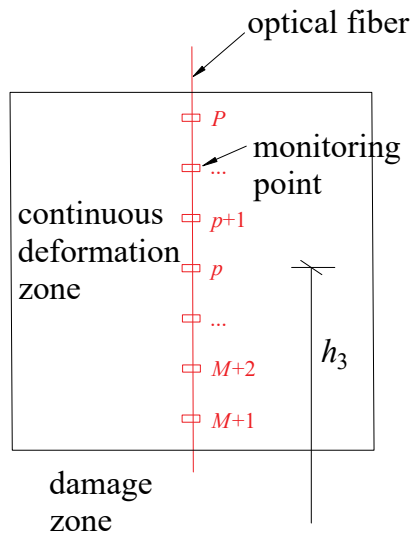


Fig. 2-8 Schematic of the monitoring points number method of continuous deformation zone

2.3 Parameter analysis of subsidence calculation model

2.3.1 Calculation and sensitivity analysis of damage factor

(1) Calculation of the damage factor

The damage factor is related to the degree of damage and deformation of the rock mass. Conventionally, the internal defects of microelement of rock are subject to obey the statistical law and the two-parameter Weibull distribution (Chen 2018; Krajcinovic 1982). The damage factor can be defined as:

$$D = 1 - \exp \left[- \left(\frac{\varepsilon_m}{\varepsilon_0} \right)^{m_0} \right] \quad (2-16)$$

where ε_m is the overburden strain measured by the optical fibre sensor; ε_0 , m_0 is Weibull distribution parameters, which can be determined from the stress-strain curve fitting.

ε_0 reflects the strain value of the rock, which is proportional to the mean value of the strain, and it also increases along with the increase of the peak strain in the stress-strain curve. m_0 reflects the concentration of strain distribution of rock microelements, and the bigger m_0 is, the more concentrated the strain distribution becomes. m_0 is also referred to as the homogeneity index (Tang 1997).

By substituting Eq. (2-16) into the constitutive equation of damaged rock mass, a new constitutive function of the damaged rock based on the Weibull distribution is obtained:

$$\sigma_z - \mu_0(\sigma_x + \sigma_y) = E\varepsilon_z \exp\left[-(\varepsilon_m / \varepsilon_0)^{m_0}\right] \quad (2-17)$$

where μ_0 is the passion ratio; σ_x , σ_y and σ_z are the stress of the material in x , y and z direction, respectively; and ε_z is the strain of the material in z direction.

In order to find the magnitude of distribution parameters, logarithmic transformation is applied to Eq. (2-17). Thus, it is rewritten as:

$$m_0 \ln \varepsilon_z - m_0 \ln \varepsilon_0 = \ln \left\{ -\ln \frac{\sigma_z - \mu_0(\sigma_x + \sigma_y)}{E\varepsilon_z} \right\} \quad (2-18)$$

According to the post-peak data of the stress-strain curve in the triaxial compression test of the rock mass, the value of ε_0 and m_0 can be obtained by linear fitting of Eq. (2-18).

For example, in order to obtain the relationship between stress and strain of sandstone, a software named PFC3D based on particle discrete element method is adopted to conduct a conventional triaxial compression test. The parameters used in this numerical simulation test are as follows: elastic modulus is 2.29×10^3 MPa; peak strength is 190 MPa when confining pressure is 8 MPa; poisson's ratio is 0.230 (Yang 2016). After parameter calibration, discrete particle simulation in the conventional triaxial compression test was carried out to study stress-strain curve of sandstone when

the confining pressure changes as 2 MPa, 8 MPa, 14 MPa, 20 MPa, 26 MPa and 32 MPa.

Fig. 2-9 shows the results of triaxial compression tests of sandstone under different confining pressures, and p_0 represents the confining pressure.

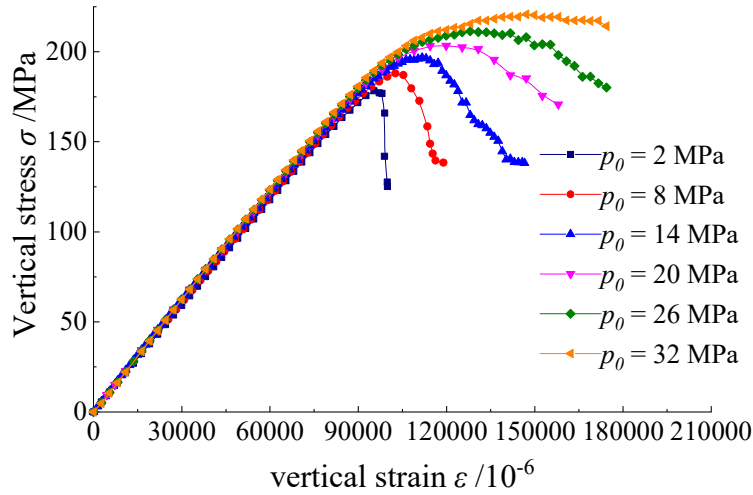


Fig. 2-9 Stress-strain curve of sandstone under different confining pressures

As shown in Fig. 2-9, as the confining pressure increases, the peak strength and peak strain of the rock mass also increases, while the concentration of the stress-strain curve decreases.

The post-peak data of the sandstone stress-strain curve under different confining pressures is fitted by linear fitting according to Eq. (2-18). The change characteristics of m_0 , ε_0 and ε_{peak} under different confining pressures are shown in Fig. 2-10.

As shown in Fig. 2-10, due to the concentration changes of the stress-strain curve concentration under different confining pressures, m_0 decreases exponentially with the increasing of the confining pressure, and their fitting function is $m_0 = \exp(1.83 - 0.104p_0 + 0.0015p_0^2)$, coefficient of determination R^2 is 0.99. When the confining pressure reaches 20 MPa, m_0 gradually stabilizes. ε_0 and ε_{peak} increase linearly with the increasing of the confining pressure, and their fitting functions are $\varepsilon_0 = 0.097 + 0.0034p_0$ and $\varepsilon_{peak} = 0.090 + 0.0017p_0$, whose coefficients of determination R^2 are 0.99 and 0.98, respectively. Besides, ε_0 is always larger than ε_{peak} .

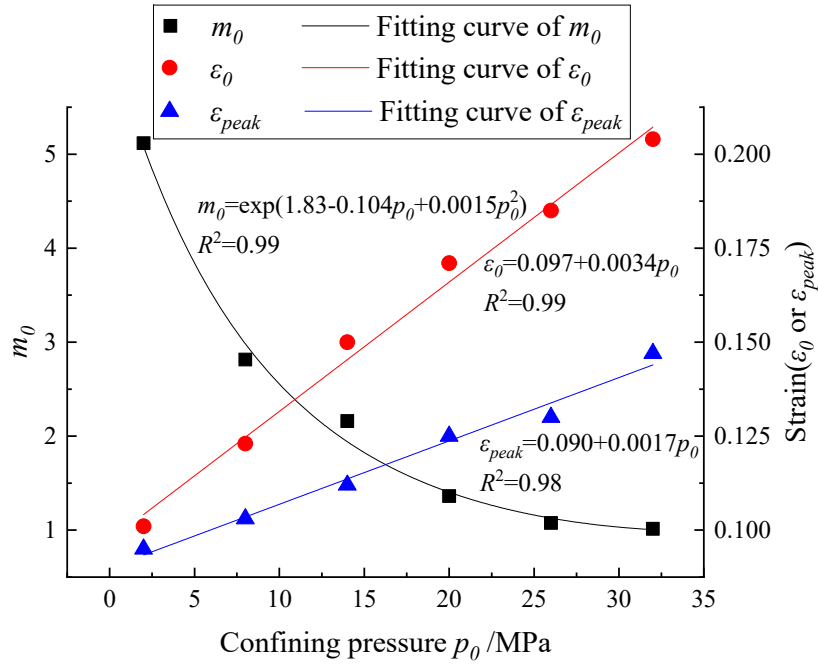


Fig. 2-10 Change rules of distribution parameters and peak strain under different confining pressures

(2) Sensitivity analysis of distribution parameters in caving zone

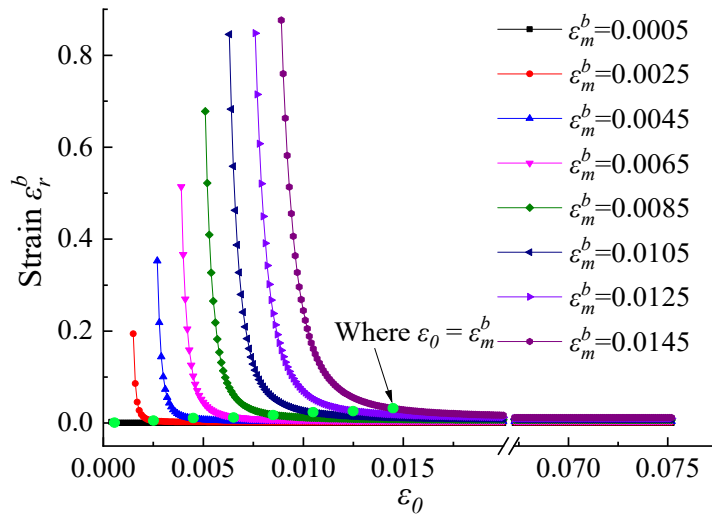
By substituting Eq. (2-16) into the strain calculation function Eq. (2-7) of the caving zone, the following equation can be obtained:

$$\varepsilon_r^b = \frac{\varphi(K_0 - 1)\varepsilon_m^b}{\exp\left[-\left(\varepsilon_m^b / \varepsilon_0\right)^{m_0}\right]\left[\left(1 - \varepsilon_m^b\right)K_0 - 1\right]} \quad (2-19)$$

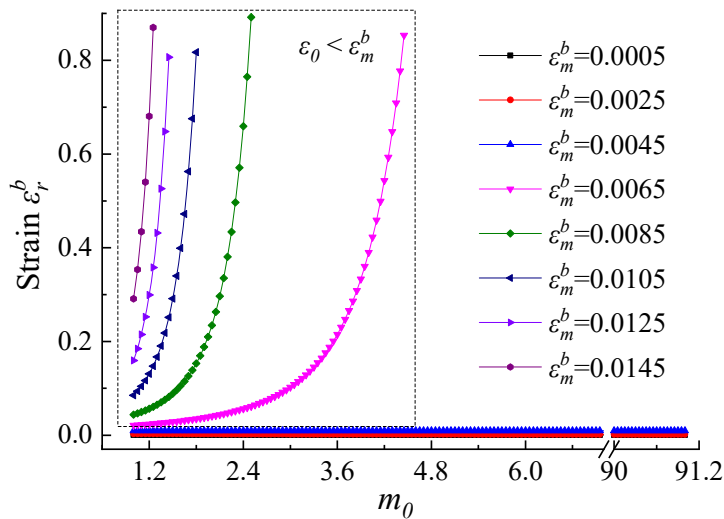
Assume that the contact parameter of rock particles φ is 0.75, the bulking factor K_0 is 1.3, and the strain at the monitoring point of the caving zone is 0.0005, 0.0025, 0.0045, 0.0065, 0.0085, 0.0105, 0.0125 and 0.0145, respectively. Then, the influence of distribution parameters on the precision of subsidence calculation in the caving zone was studied. To control the variable, m_0 should be constant and fixed as 3 when discussing the influence of ε_0 . When studying the influence of m_0 , ε_0 should be constant and fixed as 0.0045. Fig. 2-11 shows the curves of ε_r^b changing with ε_0 and m_0 respectively.

Fig. 2-11(a) shows that when $\varepsilon_0 \geq \varepsilon_m^b$, the maximum change value of the strain

ε_r^b is 0.00198 as ε_0 increases from ε_m^b to 0.0752. Hence, ε_0 has little influence on ε_r^b , and according to Eq. (2-8), it also has little influence on subsidence calculation results. When $\varepsilon_0 < \varepsilon_m^b$, except for $\varepsilon_m^b = 0.0005$ (As the data of $\varepsilon_0 < \varepsilon_m^b$ when $\varepsilon_m^b = 0.0005$ is less, there is no abrupt phase of the calculated strain in the caving zone ε_r^b), ε_r^b decreases sharply at the initial stage of ε_0 , and its sensitivity to ε_0 is high. Hence, in this situation, the accuracy of ε_0 has great influences on the subsidence calculation results.



(a) The relation between ε_0 and ε_r^b when $m_0 = 3$



(b) The relation between m_0 and ε_r^b when $\varepsilon_0 = 0.0045$

Fig. 2-11 Influences of ε_0 and m_0 on the strain ε_r^b in the caving zone

As shown in Fig. 2-11(b), when $\varepsilon_0 \geq \varepsilon_m^b$, strain in the caving zone ε_r^b is almost constant with the change of m_0 . The maximum change of the strain ε_r^b is 0.0014 as m_0 changes from 1 to 91, which indicates that the change of m_0 at this situation has little effect on the strain ε_r^b , and thus has little effect on the final subsidence calculation results. When $\varepsilon_0 < \varepsilon_m^b$ and m_0 increases to a certain value, the strain in the caving zone ε_r^b increases sharply, especially when $\varepsilon_m^b \geq 0.0005$, the strain ε_r^b changes almost vertically in Fig. 2-11(b), and at this time, the accuracy of m_0 has a huge impact on the subsidence calculation results.

Because of the mined-out stage of the goaf, the secondary broken of the rock particles after rock mass breaks is not considered. According to Fig. 2-10, ε_0 is always larger than ε_{peak} . It ought to be noted that from the derivation process of the subsidence calculation model of the caving zone, D is the damage factor of the rock mass blocks rather than the entire rock mass in the caving zone. As the overburden subsidence after mining is in a stable stage and no rock particle at the monitoring point breaks again, the strain at the monitoring point in the caving zone ε_m^b will always be smaller than the peak strain ε_{peak} of the rock body, and also smaller than ε_0 . Hence, the accuracy of distribution parameters ε_0 and m_0 have a little effect on the subsidence results of the caving zone. In that case, if fix $\frac{\varepsilon_m^b}{\varepsilon_0} = \left| \varepsilon_{mk}^b \right|$ (ε_0 and ε_{mk}^b always has the same directions), $m_0 = 1$, and the model for calculating the overburden subsidence in the stable stage in the caving zone can be simplified as:

$$W_b(h_1) = \sum_{k=1}^n \frac{\lambda \varphi (K_0 - 1) \varepsilon_{mk}^b}{\exp(-\left| \varepsilon_{mk}^b \right|) \left[(1 - \varepsilon_{mk}^b) K_0 - 1 \right]} \quad (2-20)$$

2.3.2 Calculation and sensitivity analysis of contact parameters

(1) Sensitivity analysis of distribution parameters in damage zone

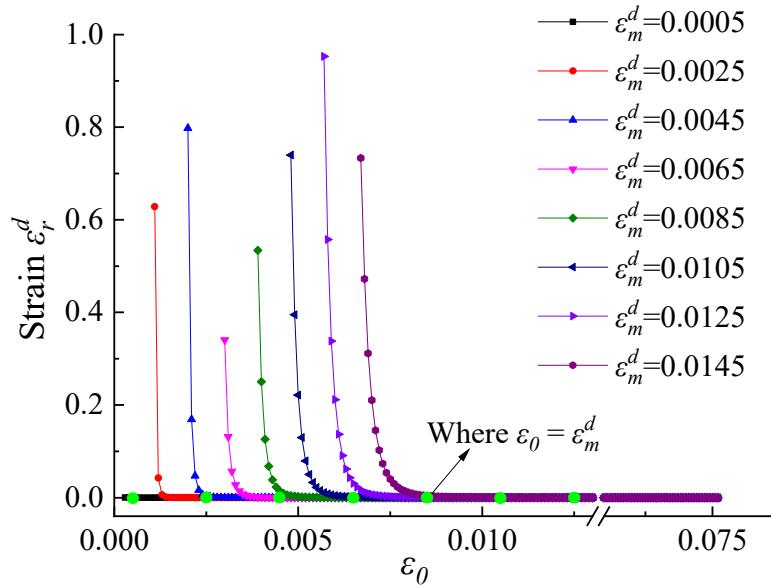
By substituting Eq. (2-16) into strain calculation function of the damage zone Eq. (2-13), then the equation can be obtained as follows:

$$\varepsilon_r^d = \frac{\sigma_i}{\exp\left[-\left(\varepsilon_m^d / \varepsilon_0\right)^{m_0}\right] (E\varepsilon_i + \sigma_i)} \varepsilon_m^d \quad (2-21)$$

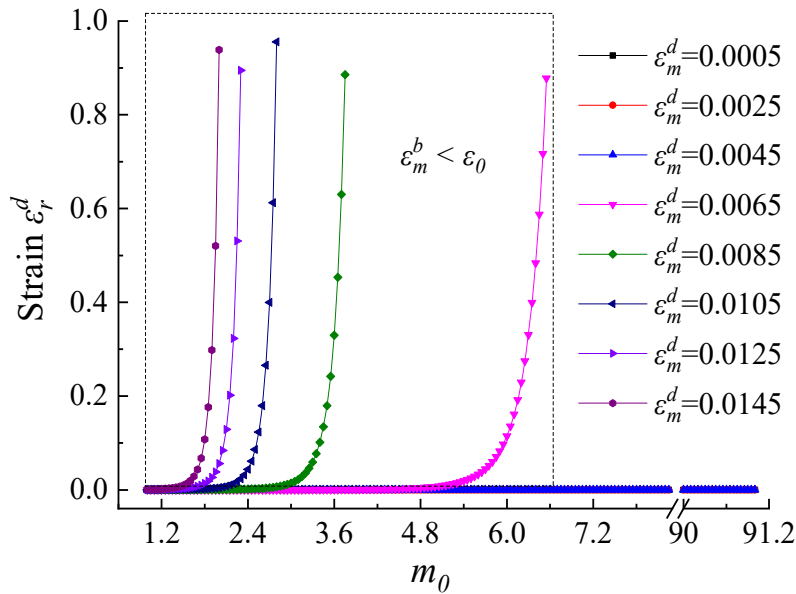
In order to study the influence of distribution parameters on subsidence calculation results of the damage zone, fix the values of the parameters are as follows: $\sigma_i = 3$ MPa, $\varepsilon_i = 0.075$ and the strain at monitoring points in the damage zone ε_m^d are 0.0005, 0.0025, 0.0045, 0.0065, 0.0085, 0.0105, 0.0125 and 0.0145, respectively. When analyzing the influence of ε_0 on ε_r^d , fix $m_0 = 3$. When analyzing the influence of m_0 on ε_r^d , fix $\varepsilon_0 = 0.0045$. Fig. 2-12 shows the changes of calculated strain in the damage zone ε_r^d along with ε_0 and m_0 .

As shown in Fig. 2-12, similar to the caving zone, when $\varepsilon_0 \geq \varepsilon_m^d$, the maximum change of the strain in the damage zone ε_r^d is 4.97×10^{-5} as ε_0 increases from ε_m^d to 0.0752, while as m_0 increases from 1 to 91, the maximum change of ε_r^d is 3.72×10^{-6} . Therefore, when $\varepsilon_0 \geq \varepsilon_m^d$, combining with Eq. (2-14), it can be found that the results of subsidence calculation are insensitive to the changes of ε_0 and m_0 , and the accuracy of ε_0 has no obvious impact on the final results of subsidence calculation. When $\varepsilon_0 < \varepsilon_m^d$, similar to the caving zone, except for $\varepsilon_m^d = 0.0005$, the calculated strain of the damage zone ε_r^d decreases sharply in turn at the initial stage of ε_0 , and under this situation, its sensitivity to ε_0 is high, which means the accuracy of ε_0 has a large impact on the final calculation results of subsidence. As for m_0 , when $\varepsilon_0 < \varepsilon_m^d$, the relationship curve of ε_r^d and m_0 has the tendency of steady increase followed by a rapid increase, and the bigger the ε_m^d is, the smaller the m_0 at the catastrophe point is. Thus, the larger the

monitored strain in the damage zone ε_m^d is, the smaller the value of m_0 at the high sensitivity area of the strain in the damage zone becomes. Hence, when $\varepsilon_0 < \varepsilon_m^d$, the subsidence calculation result is sensitive to the change of m_0 .



(a) The relation between ε_0 and ε_r^d when $m_0 = 3$



(b) The relation between m_0 and ε_r^d when $\varepsilon_0=0.0045$

Fig. 2-12 Influences of ε_0 and m_0 on the strain ε_r^d in the damage zone

The rock mass in the damage zone has not completely broken yet and still has the

ability to withstand stress, so it is reasonable to assume that ε_m^d is always less than ε_0 like the caving zone. Therefore, it can be considered that the accuracy of the distribution parameters ε_0 and m_0 under discussion has little effect on the subsidence calculation results of the damage zone. When the strain at monitoring points is less than the distribution parameter ε_0 , $\frac{\varepsilon_{mk}^d}{\varepsilon_0} = |\varepsilon_{mk}^d|$ (ε_0 and ε_{mk}^d always has the same direction) and $m_0 = 1$ and be fixed and a simplified model for calculating the subsidence of the damage zone can be obtained:

$$W_d(h_2) = W_b + \sum_{k=N+1}^m \frac{\lambda \sigma_i}{\exp(-|\varepsilon_{mk}^d|)(E\varepsilon_i + \sigma_i)} \varepsilon_{mk}^d \quad (2-22)$$

(2) *Sensitivity analysis of particle contact parameter in caving zone*

According to Eq. (2-7), the vertical strain of the rock mass in the caving zone ε_r^b is proportional to the particle contact parameter φ . The influence of the contact parameter on the subsidence calculation model from two perspectives: contact surface angle θ and friction coefficient μ were analyzed.

In order to study the influence of changes of contact surface angle θ on the subsidence calculation model, the following parameters can be fixed: bulking coefficient K_0 as 1.3, friction coefficient μ as 0.35, and distribution parameters ε_0 and m_0 as 0.0045 and 3, respectively. Fig. 2-13 shows the influence of changes of the contact surface angle on the subsidence calculation model under different monitored strain conditions.

According to Fig. 2-13, the strain of the caving zone ε_r^b is symmetrical along the contact surface angle of 90° . As θ increases within the range of $0\sim 180^\circ$, ε_r^b and φ decrease at first and then increase, which reach the maximum when θ is 0° and 180° and reach the minimum when θ is 90° . When $\varepsilon_m^b \leq 0.0025$, the change of θ has little effect on ε_r^b , and under this situation, when $\varepsilon_m^b = 0.0025$, ε_r^b changes the most, being

0.002. When $\varepsilon_m^b > 0.0025$, changes of θ affect ε_r^b . The bigger the ε_m^b is, the bigger the curvature is, and the more sensitive of ε_r^b changes of θ is. When $\varepsilon_m^b = 0.0045$, ε_r^b undergoes the maximum change, being 0.016. Therefore, the maximum influence of the surface contact angle of rock particles on model calculation results is $0.016h_b$ (h_b is the height of the caving zone). Hence, when calculating subsidence of the caving zone by using the model, the accuracy of θ needs to be considered.

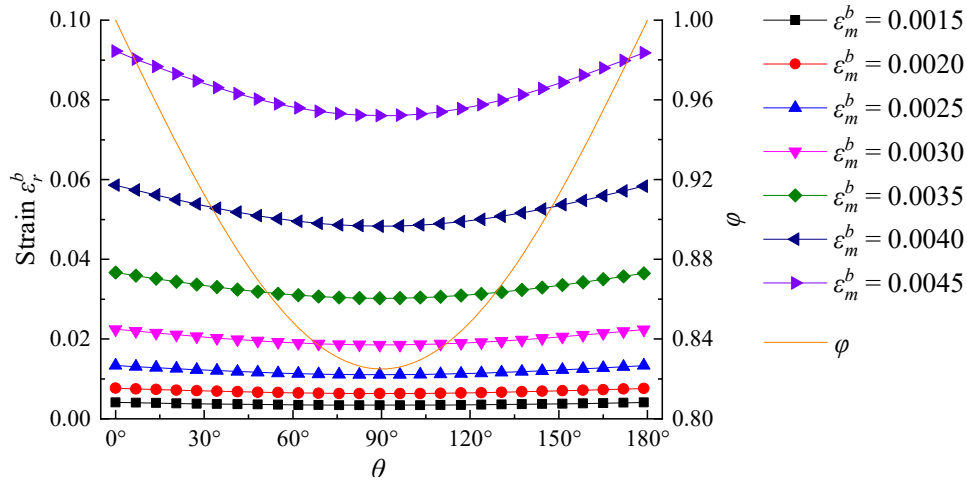


Fig. 2-13 Curve of θ 's influence on the calculated strain ε_r^b in the caving zone

Due to the large amount of θ and the difficulty of monitoring on field, it is assumed that θ follows a normal distribution in the range $[0^\circ, 180^\circ]$, that is, $\theta \sim N(90^\circ, (30^\circ)^2)$. Then the mean value of θ can be obtained as follows:

$$\bar{\theta} = \int_0^{180} \frac{1}{569.2} \exp\left[-\frac{(\theta - 90)^2}{1800}\right] d\theta \quad (2-23)$$

Hence, currently, $\varphi = 1 - 0.463\mu$.

In order to study the sensitivity of the subsidence calculation model to changes of the friction coefficient μ , fix $K_0 = 1.3$, $\theta = 90^\circ$, $\varepsilon_0 = 0.0045$ and $m_0 = 3$. Fig. 2-14 shows the influence of friction coefficient changes on the subsidence calculation model under different monitoring point strain ε_m^b conditions.

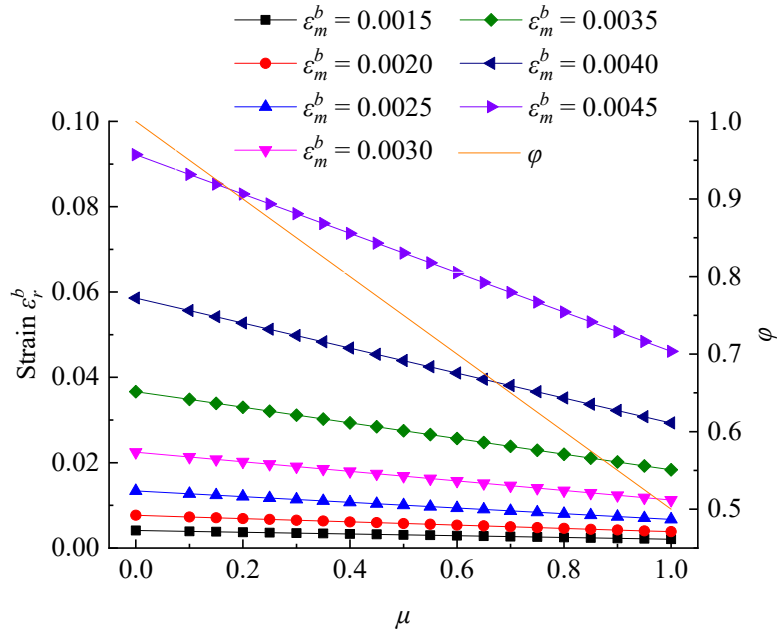


Fig. 2-14 Curve of μ 's influence on the strain ε_r^b in the caving zone

According to Fig. 2-14, φ and ε_r^b decrease linearly with the friction coefficient, and the decreasing rate increases with the strain at monitoring points. When $\varepsilon_m^b = 0.0015$, the change of ε_r^b is smallest with the increase of the friction coefficient, as 0.002. When $\varepsilon_m^b = 0.0045$, the influence value of the contact parameter on ε_r^b is getting the maximum value, as 0.046. Hence, the maximum influence value of the rock particle friction coefficient on the calculation model is $0.046hb$. φ decreases linearly with the contact surface friction coefficient μ , and the value of it is always from 0.5 to 1.0.

2.3.3 The final calculation model after parameter analysis

After the analysis of the damage factor and the contact parameters, a simplified final calculation model of the overburden subsidence is obtained:

$$W(h) = \begin{cases} \sum_{k=1}^n \frac{\lambda(1-0.463\mu)(K_0-1)\varepsilon_{mk}^b}{\exp[-|\varepsilon_{mk}^b|] \left[(1-\varepsilon_{mk}^b)K_0-1 \right]} & 0 < h \leq H_1 \\ W(H_1) + \sum_{k=N+1}^m \frac{\lambda\sigma_i}{\exp[-|\varepsilon_{mk}^d|] (E\varepsilon_i + \sigma_i)} \varepsilon_{mk}^d & H_1 < h \leq H_2 \\ W(H_2) + \sum_{k=M+1}^p \lambda\varepsilon_{mk}^c & H_2 < h \leq H_3 \end{cases} \quad (2-24)$$

Where H_1 is the height of the boundary between the caving zone and the damage zone; H_2 is the height of the boundary between the damage zone and the continuous deformation zone; H_3 is the height of the total overburden.

2.4 Summary

(1) According to the deformation and failure characteristics of the overburden rock above the goaf, the overburden can be divided into the caving zone, damage zone and continuous deformation zone. Based on the characteristics of the broken rock mass in the caving zone, the fractured rock mass in the damage zone and the intact rock and soil in the continuous deformation zone, a measured strain-based model for calculating subsidence can be proposed.

(2) The proposed model considers the uneven deformation of the rock mass and can reflect the relationship between the mechanical parameters and the subsidence of the overburden. It is also suitable to calculate the overburden subsidence above the goaf when monitored by distributed optical fiber sensor.

(3) The calculation method and sensitivity analysis of the damage distribution parameters and the particle contact parameters were analyzed. The damage distribution parameters can be fixed when the damage distribution parameter ε_0 is smaller than the monitored strain ε_m . The form of the calculation model of the caving zone and the damage zone was simplified according to the sensitivity analysis of the parameters.

References

- Can E, Kus, cu S, , Mekik C. Determination of underground mining induced displacement using GPS observations in Zonguldak-Kozlu Hard Coal Basin. *Int J Coal Geol.* 2012;89:62–69.
- Chen S, Qiao C, Ye Q, et al. Comparative study on three-dimensional statistical damage constitutive modified model of rock based on power function and Weibull distribution. *Environ. Earth Sci.* 2018;77(3):108.
- Chrzanowski A, Monahan C, Roulston B, et al. Integrated monitoring and modelling of ground subsidence in potash mines. *Int J Rock Mech Min Sci.* 1997;34(3-4):55.
- Donnelly LJ. A review of international cases of fault reactivation during mining subsidence and fluid abstraction. *Q J Eng Geol.* 2009;42(1):73–94.
- Du Y, Chen Y, Zhuang Y, et al. A uniform strain transfer scheme for accurate distributed optical fiber strain measurements in civil structures. *Inventions.* 2018;3(2):30.
- Fabien, R.; Bao, X.; Li, Y.; Yu, Q.; Yale, A.; Kalosha, V.P.; Chen, L. Signal processing technique for distributed Brillouin sensing at centimeter spatial resolution. *Lightwave Technol.* 2007, 25, 3610–3618.
- Gao L, Han C, Xu Z, et al. Experimental study on deformation monitoring of bored pile based on BOTDR. *Applied Sciences*, 2019, 9(12): 2435.
- Gu'eguen Y, Deffontaines B, Fruneau B, et al. Monitoring residual mining subsidence of Nord/Pas-de-Calais coal basin from differential and Persistent Scatterer Interferometry (Northern France). *J Appl Geophys.* 2009;69:24–34.
- Horiguchi T, Shimizu K, Kurashima T, Tateda M, Koyamada Y. Development of a distributed sensing technique using Brillouin scattering. *J. Lightwave Technol.* 1995; 13:1296-1302.
- Hong CY, Zhang YF, Li GW, Zhang MX, Liu ZX. Recent progress of using Brillouin distributed fiber optic sensors for geotechnical health monitoring. *Sens. Actuators A Phys.* 2017;258:131-145.
- Hong CY, Zhang YF, et al. Recent progress of using Brillouin distributed fiber optic sensors for geotechnical health monitoring. *Sens. Actuator A Phys.* 2017;258:131–145.
- Jung HC, Kim SW, Jung HS, et al. Satellite observation of coal mining subsidence by persistent
-

- scatterer analysis. *Eng Geol.* 2007;92:1–13.
- Klar A, Dromy I, Linker R. Monitoring tunneling induced ground displacements using distributed fiber-optic sensing. *Tunn. Undergr. Space Technol.* 2014;40:141-150.
- Krajcinovic D, Silva MAG. Statistical aspects of the continuous damage theory. *Int J Solid Struct.* 1982;18(7):551–562.
- O'Connor KM, Murphy EW. TDR monitoring as a component of subsidence risk assessment over abandoned mines. *Int J Rock Mech Min Sci.* 1997;34(3-4):230.
- Peng SS, ed. *Surface Subsidence Engineering: Theory and Practice.* New York: CRC Press; 1992:1–4.
- Ryder JA, Wagner H. 2D analysis of backfill as means of reducing energy release rates at depth. In: *Chamber of Mines of South Africa.* Johannesburg; 1978:47–78.
- Salamon MDG. Mechanism of caving in longwall coal mining. In: *Rock Mechanics Contributions and Challenges: Proceedings of the 31st U.S. Golden: Symposium;* 1990:161–168.
- Sakairi Y, Uchiyama H, Li ZX, Adachi S. System for measuring temperature and strain separately by BOTDR and OTDR. *Proc. SPIE* 2002, 4920,274-284.
- Shabanimashcool M, Li CC. Numerical modelling of longwall mining and stability analysis of the gates in a coal mine. *Int J Rock Mech Min Sci.* 2012;51:24–34.
- Shi B, Sui H, Liu J, et al. The BOTDR-based distributed monitoring system for slope engineering//*Proceedings of the 10th IAEG International Congress, Nottingham, UK.* 2006: 6-10.
- Tang CA. Numerical simulation of progressive rock failure and associated seismicity. *Int J Rock Mech Min Sci Geomech Abstr.* 1997;34(2):249–261.
- Wang JH. Development and prospect on fully mechanized mining in Chinese coal mines. *Int. J. Coal Sci. Technol.* 2014;1(3):253–260.
- Weng, Y.; Ip, E.; Pan, Z.; Wang, T. Singlend simultaneous temperature and strain sensing techniques based on Brillouin opticaltime domain reflectometry in fewmode fibers. *Opt. Express* 2015, 23, 9024–9039.
- Yang ZF, Li ZW, Zhu JJ, et al. Deriving dynamic subsidence of coal mining areas using InSAR
-

- and logistic model. *Rem Sens.* 2017;9(2):125.
- Yavuz H. An estimation method for cover pressure re-establishment distance and pressure distribution in the goaf of longwall coal mines. *Int J Rock Mech Min Sci.* 2004;41(2):193–205.
- Zhang CC, Shi B, Gu K, et al. Vertically distributed sensing of deformation using fiber optic sensing. *Geophys Res Lett.* 2018;45(21):732–741.
- Zhang CC, Shi B, Gu K, et al. Vertically distributed sensing of deformation using fiber optic sensing. *Geophys Res Lett.* 2018;45(21):732–741.
- Zhang CC, Shi B, Zhu HH, et al. Toward distributed fiber-optic sensing of subsurface deformation: a theoretical quantification of ground-borehole-cable interaction. *J. Geophys. Res. Solid Earth.* 2020;125(3),e2019JB018878.
- Zhang D, Cui HL, Shi B. Spatial resolution of DOFS and its calibration methods. *Optic Laser Eng.* 2013;51:335–340.
- Zhang W, Xiao R, Shi B, et al. Forecasting slope deformation field using correlated grey model updated with time correction factor and background value optimization. *Eng Geol.* 2019;260:105215.
- Zhang CC, Zhu HH, Shi B, et al. Experimental investigation of pullout behavior of fiber-reinforced polymer reinforcements in sand. *J Compos Construct.* 2015;19(3), 04014062.
- Zhang CC, Zhu HH, Shi B. Role of the interface between distributed fibre optic strain sensor and soil in ground deformation measurement. *Sci Rep.* 2016;6:36469.
- Zhang C, Tu S, Zhao YX. Compaction characteristics of the caving zone in a longwall goaf: a review. *Environ. Earth Sci.* 2019;78(1):27.

CHAPTER 3

3 Field investigation of overburden subsidence by using BOTDR technology

According to the Chapter 2, a calculation method considering each zone's rock mass properties based on BOTDR technology is proposed to obtain the overburden subsidence. To verify the feasibility of this monitoring and calculation method, field studies at Zhangzhuang Coal Mine were carried out. Optical fiber sensor based on BOTDR technology was used to monitoring the overburden vertical strain data of Zhangzhuang Coal Mine after mining, also the subsidence results was calculated by adopting the calculation model proposed.

3.1 Distributed monitoring

3.1.1 A survey of test site

Zhangzhuang Coal Mine is in the middle of the Zhahe synclinorium in Huaibei Coalfield, which is 8 kilometers northeast of Huaibei City, Anhui Province, China. Take Zhang Huaizhu working face in Zhangzhuang Coal Mine as an example, BOTDR technology was used to study the subsidence calculation methods and subsidence characteristics of overburden above the goaf. The coal seam thickness of Zhang Huaizhu working face is 3.2 m, and its burial depth is from 240.33 m to 243.53 m. The stratum layer distribution and physical and mechanical parameters of Zhangzhuang coal mine are shown in Table 3-1.

Table 3-1 Physical and mechanical properties of the strata in Zhangzhuang coal mine

No	Layer name	Burial depth (m)	Thickness (m)	Bulk density (kN/m ³)	Elastic modulus (10 ⁴ MPa)
(1)	Unconsolidated layers	65	65	14.7	6×10 ⁻⁴
(2)	Sandy mudstone	68.53	3.53	24.79	0.67
(3)	Mudstone	76.82	8.29	24	0.49
(4)	Sandstone	80.78	3.96	25.97	10
(5)	Mudstone	115.44	34.66	24.58	0.65
(6)	Sandstone	134.65	19.21	25.97	9.51
(7)	Mudstone	178	43.35	24.44	0.62
(8)	Mudstone interbedded with sandstone	229.96	51.96	24.83	4.48
(9)	Mudstone	240.33	10.37	24.7	0.55
(10)	3# coal	243.53	3.2	--	--
(11)	Carbon mudstone	251.56	8.03	24.01	0.6

3.1.2 Distributed monitoring scheme for overburden in the goaf

The N8511 BOTDR instrument was used to test the strain distribution information of the overburden, and the optical fiber is implanted as the method expressed in Subsection 2.2.1. Table 3-2 shows the main technical performance indicators of the N8511 BOTDR instrument.

Table 3-2 Main technical performance indicators of N8511 optical fiber strain analyzer

Name	Value				
Measuring range (km)	1, 2, 5, 10, 20, 40, 80				
Space sampling interval (m)	1.00, 0.50, 0.20, 0.10, 0.05				
Spatial pointing accuracy (m)	$\pm(2.0 \times 10^{-5} \times \text{measuring range (m)} + 0.2\text{m} + 2 \times \text{sampling interval (m)})$				
Strain measurement range	-1.5% ~ 1.5% (15,000 $\mu\varepsilon$)				
Pulse width (ns)	10	20	50	100	200
Spatial resolution degree (m)	1	2	5	11	22
Strain measurement precision	$\pm 0.004\% (40\mu\varepsilon)$		$\pm 0.003\% (30\mu\varepsilon)$		
Repeatability	<0.04%		<0.02%		

In order to grasp the on-site data of ground subsidence above the goaf and verify the proposed subsidence calculation model, the hydrostatic levelling line based on fiber Bragg grating (FBG) is set from north to south at 10 m west of the drilling hole. The distribution of optical fiber monitoring point and hydrostatic levelling monitoring line in the mining area of Zhangzhuang Coal Mine is shown in Fig. 3-1.



Fig. 3-1 Layout location of hydrostatic levelling line and optical fiber monitoring point

The detailed process of the laying out the fiber is described as follows:

(1) Installation of guide head

A 1.5-2.5 m long steel bar with a thickness of 0.5-1 cm is welded to the tail of the guide head to facilitate the drill rod to be placed under the guide head. Before the construction, pass the mine-used thick fixed-point optical cable and metal base cable through the guide head, and then weld them to form a U-shaped loop. After that, the cables will be connected and checked whether they are accessible. As the special-made fixed-point optical cable for mining is thick, the optical cable is fixed on the guide head with a hoop, as shown in Fig. 3-2.

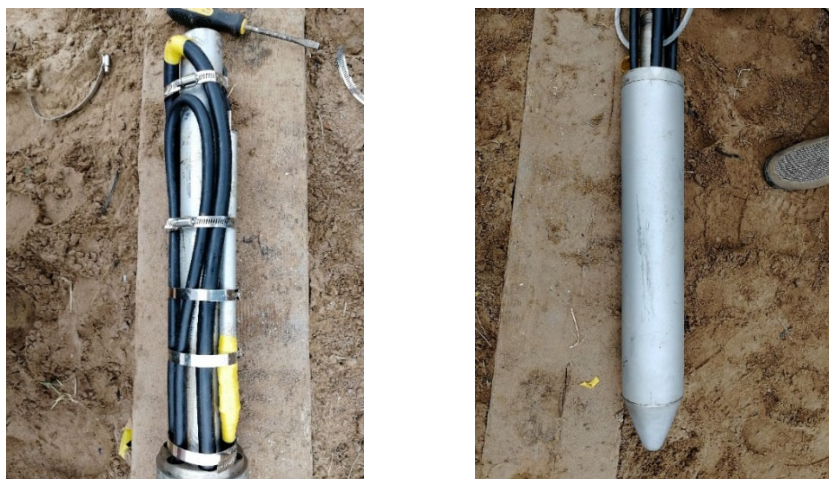


Fig. 3-2 Guide head assembling and optical cable welding

(2) Setting up the pay-off reel

Set up the pay-off reel directly opposite to the dring rig and fix the pay-off reel to facilitate the lowering of the optical cable, as shown in Fig. 3-3.



Fig. 3-3 Pay-off reel

(3) Lowering the optical cable

Put mine fixed-point optical cable and counterweight guide head into the drilling hole, and then lower the drill rod to bring the optical cable into the deep part of the drilling hole, shown in Fig. 3-4.



(a) Detail view of lowering



(b) Whole view of lowering

Fig. 3-4 Lowering of the optical cable

(4) Optical cable securing and initial testing

Fix the steel wire rope and tighten the optical cable. Then fixed the optical cable on the pay-off rack. After that, a demodulator is used to detect the initial strain value of the optical cable after lowering.

(5) Backfilling the drilling hole

Backfill the drilling hole immediately. The backfilling method is layered backfilling, mainly using grouting and quartz sand.

(6) Final fixation of the optical cable

After the drilling and backfilling is completed, a support crossbar is established near the hole to fix the optical cable at the hole position. Remove the fiber optic cable wound on the pay-off rack and fix it on the support rail.

(7) Building the monitoring station

After a period of consolidation and coupling between the sensor and the backfill material, a protection station was built at the drilling hole, shown in Fig. 3-5.



Fig. 3-5 Monitoring station

3.1.3 Overburden monitoring results by BOTDR technology

The mining of coal seam of Zhang Huaizhu working face in Zhangzhuang Coal Mine was finished in April 2011. To grasp the characteristics of overburden deformation and ground subsidence tendency caused by the mining, we completed the layout of the optical fiber cable before August 9, 2013, and then performed the first test. Fig. 3-6 shows the vertical monitored strain distribution of overburden rock above the goaf during the period from October 2, 2013 to December 10, 2014.

Combined with the recommended equation of each zone's height (Coal Industry Ministry 2017) and the vertical strain distribution characteristics in Fig. 3-6, the coal seam overburden in Zhang Huaizhu working face is most likely can be divided into four zones from bottom to top: the caving zone, with a burial depth of 197 ~ 240 m; the fractured zone, with a burial depth of 160 ~ 197 m; the bending zone, with a burial depth of 65 ~ 160m; and the unconsolidated layers, with a burial depth of 0~65 m. Among them, the range of the elastic deformation area of the bending zone is 65 ~ 155 m, and the range of the seismic active area is 155 ~ 160 m.

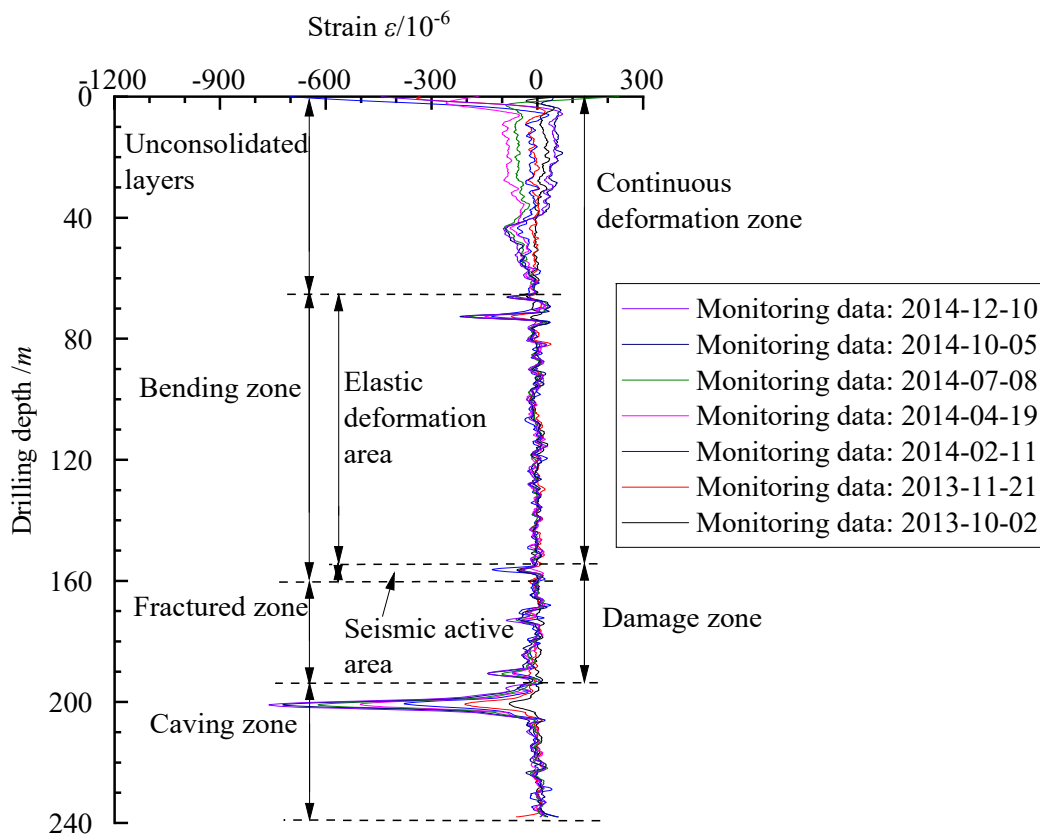


Fig. 3-6 Vertical strain distribution

As shown in Fig. 3-6, the rock mass in the caving zone has been broken, the compression deformation has not yet stabilized, so the strain changed greatly. It is noted that the deformation of the caving zone is a total long-term issue. There were many unusual deformation areas in the fractured zone. Although the rock mass has not yet settled and stabilized totally, the strain value was not large. The overall strain value of

the bending zone was small, indicating that coal mining has a limited impact on this zone. Due to the shallow burial depth of unconsolidated layers, the test data provided by the optical cable was susceptible to temperature. Additionally, affected by the looseness of this zone easily, the bonding between the optical cable and the surrounding soil layer was weak after drilling and sealing, causing the heavy fluctuation of the monitored data. Therefore, the strain monitoring results can not accurately reflect the deformation characteristics of unconsolidated layers. It is not appropriate to directly use the monitored strain of the test data when calculating the subsidence of these layers. For the application of the calculation model, these four zones of the overburden was divided again into three deformation zones: a caving zone with a burial depth of 197 m ~ 240 m, a damage zone with a burial depth of 155 m ~ 197 m and a continuous deformation zone with a burial depth of 0 ~ 155 m.

3.2 Determination of calculation model parameters

3.2.1 Initial bulking coefficient

The initial bulking coefficient of the rock mass in the caving zone can be obtained as (Tajdu's 2009):

$$K_0 = \frac{c_1 m + c_2}{100} + 1 \quad (3-1)$$

where c_1 and c_2 is strength coefficients of strata; m is the mining height.

According to the stratum properties in the caving zone of Zhang Huaizhu working face, the strength coefficients c_1 and c_2 are 4.7 and 19 (Yavuz 2004; Shao 2011), respectively. Hence, the initial bulking coefficient K_0 of the rock mass in this test is 0.33.

3.2.2 Particle contact parameters

Assume that the angle between the particle contact surface and the horizontal

direction obeys the normal distribution, the strata in the caving zone is mudstone interbedded with sandstone and the friction coefficient is fixed as 0.32, then its particle contact parameters of rock mass φ is 0.795.

3.2.3 Damage distribution parameters

The range of the caving zone and damage zone in the overburden of Zhang Huaizhu working face is: 155 m ~ 240 m, including 3 rock layers, which are layer (7), (8), and (9) in Table 3-1. To obtain the subsidence calculation parameters of the damage zone, estimate the average values of the confining pressures of the (7), (8), and (9) layers of the caving zone and damage zone according to formula $p_0 = \eta \sum(\gamma_d h_z)$ (γ_d is the bulk density; h_z is the height of each layer; η is the ratio of horizontal in-situ stress to vertical in-situ stress, and we can estimated that this ratio in Huaibei region of China is 1.9 (Zhao 2010).), use the discrete particle simulation method to obtain the stress-strain curve of the three layers under the confining pressures, and apply the linear fitting to Eq. (2-17). The damage parameters of overburden in the goaf are shown in Table 3-3.

Table 3-3 Damage parameters of overburden in the goaf

Stratum layer sequence number	Lithology	Confining pressure (MPa)	m_0	ε_0
(7)	Mudstone	3.51	3.93	0.0179
(8)	Mudstone interbedded with sandstone	4.43	7.32	0.0751
(9)	Mudstone	4.56	3.04	0.0202

3.2.4 Calculation of stress strength and plastic strain strength

As the subsidence calculation of overburden in damage zone is related to the depth of coal seam, plastic strain and elastic strain in the vertical direction of overburden, and is independent of shear strain (Shabanimashcool 2012), the effective stress can be calculated as follows:

$$\sigma_i = \sqrt{(\eta - 1)}\sigma_z \quad (3-2)$$

where σ_z is the average vertical stress of the strata in the damage zone, which can be calculated according to the burial depth and bulk density of the rock layer in Table 3-1. Therefore, the effective stresses of layer (7) and (8) of the overlying strata in the damage zone of Zhang Huaizhu working face are calculated to be 12.96 MPa and 13.44 MPa respectively.

According to the single curve assumption, curve σ_i - ε_i can be replaced by simple stretch curve σ - ε (Yang 2013). Based on the direct tensile test results of mudstone and sandstone (Dai et al. 2005), the effective strain strengths of the overburden layer (7) and (8) in the damage zone of Zhang Huaizhu working face are estimated as 6.5×10^{-6} and 8.5×10^{-6} , respectively.

4.2.5 Subsidence of unconsolidated layers

According to the engineering geological survey data of Zhangzhuang Coal Mine, unconsolidated layers on site are buried at a depth of $H = 65$ m and consist of clay and silty sand. Fig. 3-6 shows that the unconsolidated layer strain monitored by the optical fiber sensor is greatly affected by the external temperature and looseness, and it is difficult to accurately reflect the deformation characteristics of the overlying rock and soil. Thus, it is unreliable to use the monitored strain to calculate subsidence of unconsolidated layers by Eq. (2-14). Assume that the subsidence of the soil in unconsolidated layers follows the law of elastic deformation in this field test, then the subsidence of unconsolidated layers W can be calculated by:

$$W = \frac{\gamma_d H^2}{2E_s} \quad (3-3)$$

where E_s is compressive modulus of the soil. After calculation, the final subsidence value of the unconsolidated layers in this field test is 3.61 mm. Since the distributed optical fiber monitoring of Zhangzhuang Coal Mine was performed one and a half years later after mining, it can be assumed that the subsidence value of the unconsolidated layers in the monitoring period has reached the final value and remained unchanged.

3.3 Results of the field subsidence monitoring based on BOTDR technology

3.3.1 Results analysis of field test overburden subsidence

Based on the strain data of the mined-out area measured on October 2, 2013, the Eq. (2-24) are used to calculate the subsidence of each zone in Zhang Huaizhu working face with time, and Fig. 3-7 shows calculation results.

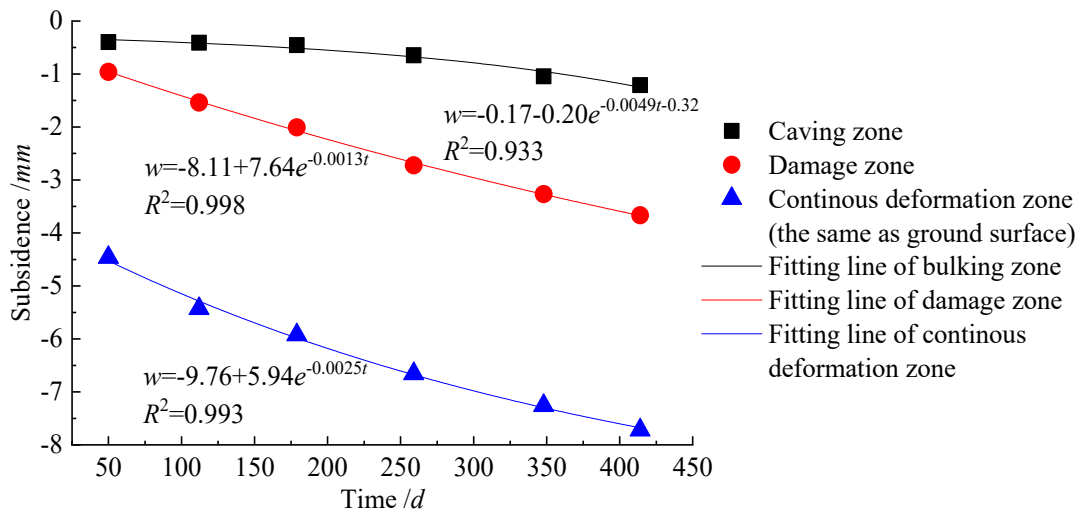


Fig. 3-7 Results of subsidence calculation model based on the measured strain in different zones

As shown in Fig. 3-7, the cumulative subsidence of the ground surface was 7.72 mm. The subsidence of the caving zone, damage zone and ground surface above the goaf gradually increased with time and showed a relationship of the negative exponential function. However, the subsidence of the caving zone is different from another two zones, and the subsidence speed is increase. The stability of this zone needs more time to prove. The total subsidence values of the caving zone and damage zone were 1.21 mm and 2.46 mm, which accounted for 15.7% and 31.9% of the surface subsidence, respectively. Hence, the damage zone contributed more to ground subsidence than the caving zone. After the coal seam was mined, the subsidence in the caving zone was affected by the large gap between the rock mass particles, so during the monitoring period, the subsidence of the caving zone gradually became faster and

remained unstable. The damage zone was affected by the continuous development of cracks and stress redistribution, so during the monitoring period, the overburden subsidence tended to be stable. The subsidence of the continuous deformation zone gradually increased with time and had the tendency to be stable. Because the proportion of the height of the continuous deformation zone was large (64.6% of the overburden height), the subsidence of this area was the main contribution zone to surface subsidence. According to the “Code for Coal Pillar Retention and Coal Mining in Buildings, Water Bodies, Railways and Main Shafts” (Coal Industry Ministry 2017), when the sinking value of the local surface point does not exceed 30mm for 6 consecutive months, the surface movement period is considered to be finished, so the ground surface subsidence of this coal mine reached a stable stage.

3.3.2 Accuracy discussion of the subsidence calculation model

In order to verify the rationality of the overburden subsidence calculation model proposed in this Chapter 2, the calculation result of this model, the result of the sensor returned strain integral method and the monitoring result by the surface hydrostatic levelling line at site were compared, as shown in Fig. 3-8. The classic strain integral method was widely accepted to disposal the BOTDR technology data, and the equation of integral method is Eq. (1-1).

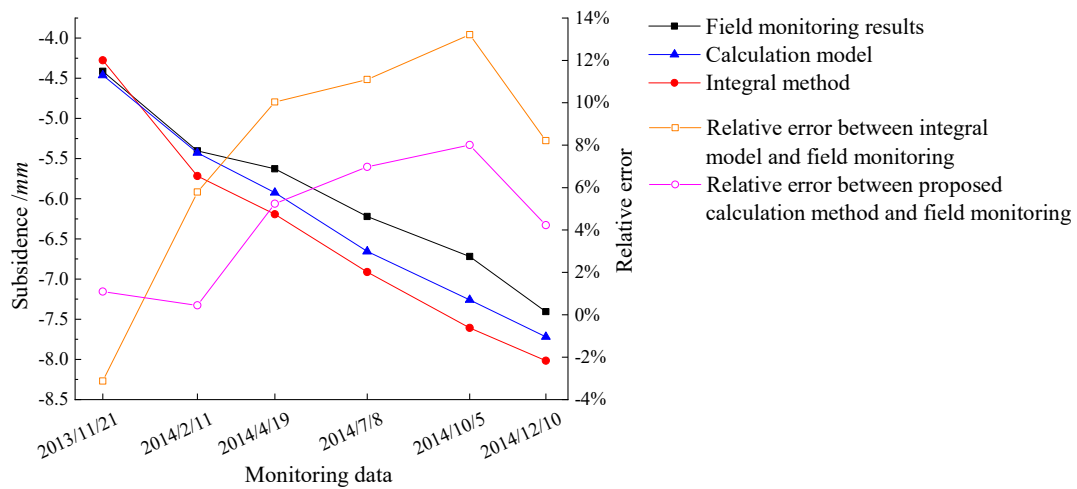


Fig.3-8 Ground surface subsidence results based on calculation model, integral method and field monitoring

According to Fig. 3-8, the relative error between the result of the subsidence calculation model and the on-site monitoring result was smaller than it of the monitored strain integral method. In addition, the calculation model considers the mechanical parameters of the overburden rock mass. Hence, it can be indicated that the calculation model proposed is trustworthy and improved the accuracy of the classic integral method.

When $t = 348 d$, the relative error of the subsidence calculation model reached a maximum value and it is around 10%. Because the monitoring period in this field case is at the stable stage of the overburden deformation, the change value of 10% is not large in this field condition. However, if the whole overburden height is large and its deformation is not stable after mining, 10% error will be much larger. Hence, further study should be carried out to analyze the error causing reason.

Firstly, because of the most complex structure in the caving zone, the caving zone has the most possibility to cause the error. Secondly, the long-term influence of the caving zone is not considered in the proposed calculation model, which was proved can be influenced most of the caving zone in Figs. 3-6 and 3-7. Thirdly, when deriving the subsidence function of the caving zone, the rock blocks was assumed that they were not broken again, which is incompatible with the reality. Fourthly, the difficulties for unconsolidated rock to move with optical fiber especially in caving zone is also the reason of the error. Hence, new side to understand the caving zone subsidence behavior is needed to further study the overburden movement law.

Aiming at the issue that the existence of cracks and voids in the caving zone affects the continuity of the rock mass, the subsidence calculation model proposed in Chapter 2 takes the uneven deformation of the overburden rock within λ range of each monitoring point into account, which improves the calculation accuracy of the overburden subsidence in the goaf. At present, the minimum spatial resolution and sampling interval of BOTDR among distributed optical fiber testing instruments are 1m and 50mm (Zhang 2013; Zhang 2019), and the minimum spatial resolution and sampling interval of optical frequency-domain reflectometry (OFDR) are 1mm (Barrias

2019). With the spatial resolution and sampling interval of the DOFS instrument keep decreasing, the parameter λ in Fig. 2-4 reduces. At that time, the strain of the rock mass between monitoring points is more accuracy, and the result of the proposed calculation model based on the overburden subsidence is closer to the actual subsidence on site.

The monitored strain integral method used to calculate the subsidence overburden is based on the following assumption: the deformation of the rock mass between two adjacent monitoring points is evenly, and the subsidence is obtained by integrating the strain data among the whole height of the overburden (Ohno 2001; Gang 2015; Wu 2017; Mohamad 2011). When the amount of rock deformation is small or it is in the stage of elastic deformation, this method can meet the requirements of subsidence calculation. However, as the existence of voids and fractures in the rock mass makes it difficult to meet the evenly requirements of mining overburden above the goaf.

When calculating damage factor of the caving zone and the damage zone, the confining pressures were estimated by $p_0 = \eta \Sigma(\gamma_d h_z)$. If it is possible, it is better to use the on-site monitoring data instead of estimated one. However, since the strain monitored by the optical sensor in the caving zone and damage zone of Zhangzhuang Coal Mine was always smaller than ε_0 , the errors of confining pressure and damage distribution parameters have little effect on the subsidence calculation results. Also, if calculated using the simplified formula, Eq. (2-23), the accuracy of confining pressure need not to be considered.

For unconsolidated layers, the final subsidence was calculated. Compared with the actual subsidence process, the calculation model result is larger. The values of particle contact parameters in the caving zone also cause errors of the calculation results. However, because the distributed monitoring was performed one and a half years later after coal mining, the overall strain value was smaller and had less impact. When calculating the damage zone subsidence, to satisfy plastic total deformation theory, we need to assume that the rock mass loading obeys the single load process. Although there is little cyclic loading phenomenon in the subsidence process of overburden rock after

mining, there is an unloading process during coal mining. Therefore, the total deformation theory has certain errors, which require further research and discussion in the future.

3.4 Summary

(1) The proposed subsidence calculation model of overburden in the goaf was applied to Zhang Huaizhu working face in Zhangzhuang mining area, and the subsidence value of each zone was obtained.

(2) The settlement speed of the caving zone increases with time, while the subsidence of the damage zone and continuous deformation zone has a negative exponential function relationship with time, and gradually increases and stabilizes.

(3) Comparing the result by the proposed subsidence calculation model with the field data, it is found that the relative error between the two is around 10%, which is less than the relative error of the result by the monitored strain integral method. The error can be thought that this is because the long-term behavior of caving zone is not considered and implemented in the calculation model. From these results, it can be concluded that the long-term deformation mechanism and behavior of caving zone have to be made clear in order to predict long-term surface subsidence due to the longwall coal extraction.

References

- Barrias A, Casas JR, Villalba S. Fatigue performance of distributed optical fiber sensors in reinforced concrete elements. *Construct Build Mater.* 2019;218:214–223.
- Coal Industry Ministry, People’s Republic of China. *The Specification of Design for Pillars of Buildings, Water Bodies, Railway, Main Shafts and Drifts.* Beijing: China Coal Industry Publishing House; 2017:53–56 (in Chinese).
- Dai GF, Xia CC, Yan C. Testing study on deformation behaviour of rock in longtan hydropower project under tensile condition. *Chinese Journal of Rock Mechanics and Engineering.* 2005;24(3):384-388. (In Chinese)
- Gang C, Shi B, Zhu HH, et al. A field study on distributed fiber optic deformation monitoring of overlying strata during coal mining. *J. Civ. Struct. Health Monit.* 2015;5:553–562.
- Mohamad H, Soga K, Pellew A, et al. Performance monitoring of a secant-piled wall using distributed fiber optic strain sensing. *J Geotech Geoenviron Eng.* 2011;137(12):1236–1243.
- Ohno H, Naruse H, Kihara M, et al. Industrial applications of the BOTDR optical fiber strain sensor. *Opt Fiber Technol.* 2001;7(1):45–64.
- Shabanimashcool M, Li CC. Numerical modelling of longwall mining and stability analysis of the gates in a coal mine. *Int J Rock Mech Min Sci.* 2012;51:24–34.
- Shao H, Jiang SG, Wang LY, Wu ZY. Bulking factor of the strata overlying the gob and a three-dimensional numerical simulation of the air leakage flow field. *Min Sci Technol.* 2011;21:261–266.
- Tajdu’s K. New method for determining the elastic parameters of rock mass layers in the region of underground mining influence. *Int J Rock Mech Min Sci.* 2009;46:1296–1305.
- Wu JH, Shi B, Cao DF, et al. Model test of soil deformation response to dragining-recharging conditions based on. *DFOS. Eng. Geol.* 2017;226:107–121.
- Yang GT, ed. *Introduction to Elasticity and Plasticity.* second ed. Beijing: Tsinghua University Press; 2013:63–70 (In Chinese).
- Yavuz H. An estimation method for cover pressure re-establishment distance and pressure
-

distribution in the goaf of longwall coal mines. *Int J Rock Mech Min Sci.* 2004;41(2):193–205.

Zhang D, Cui HL, Shi B. Spatial resolution of DOFS and its calibration methods. *Optic Laser Eng.* 2013;51:335–340.

Zhang W, Xiao R, Shi B, et al. Forecasting slope deformation field using correlated grey model updated with time correction factor and background value optimization. *Eng Geol.* 2019;260:105215.

Zhao W, ed. *Rock Mechanics*. Chang Sha. Central South University Press; 2010:104–114 (In Chinese).

CHAPTER 4

4 Creep and breakage behavior of gangue broken rock in caving zone under triaxial compression condition

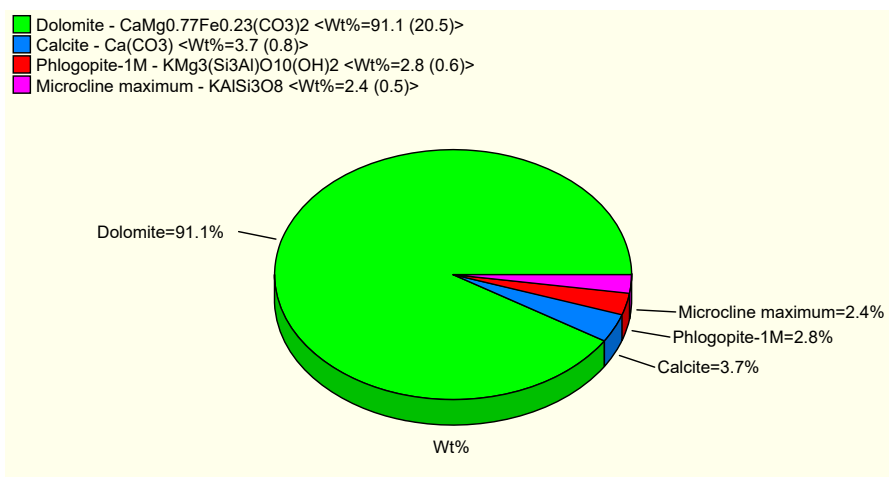
It is obvious that the time-effect on the strain in the caving zone is the biggest during the monitoring period as shown in Fig. 3-6. Also, we can see from the Fig. 3-7, the subsidence of the caving zone increases even the other two zone already stable. In addition, although the final subsidence calculation model of caving zone in Eq. (2-24) considers the mechanical parameters, the mechanism of the broken rock behavior in caving zone is not discussed. Because of the largest void rate, the rock mass of the caving zone is the most complex comparing with other zones. All in all, according to the results in Chapter 3, new side to understand the caving zone subsidence behavior is needed to improve the accuracy of the subsidence prediction model of the caving zone.

4.1 Creep experiment design

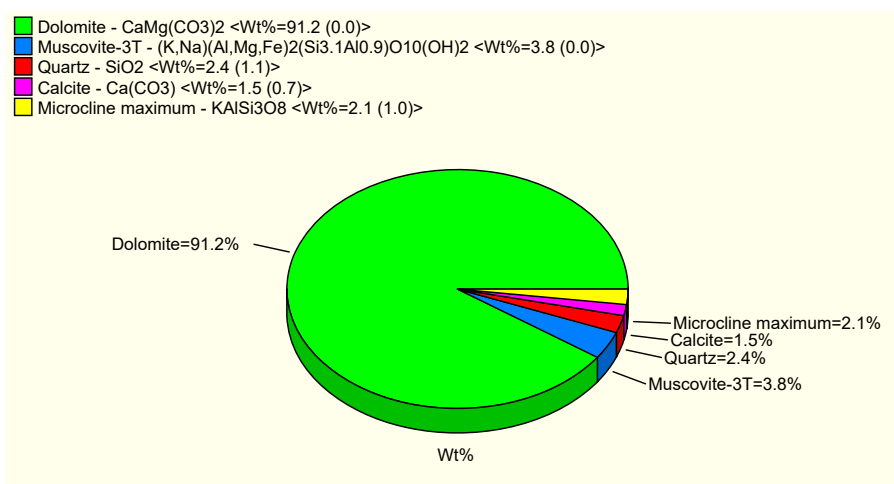
4.1.1 Material components

The broken rock of the sample in this experimental test was obtained from Nanyanchuan Township, Lingshou County, Hebei Province. To know the properties of the researched rock and provide the basic for next experimental plane making, the X-ray diffraction (XRD) scanning data of the rock blocks was obtained. Three blocks among the samples were scanned totally, and the XRD results are shown in Fig. 4-1.

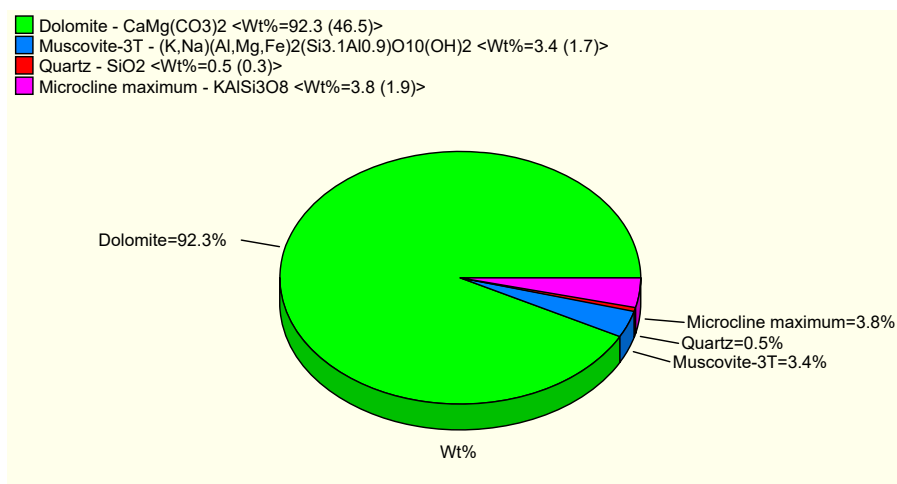
According to Fig. 4-1, the mainly component of the rock block is dolomite ($\text{CaMg}(\text{CO}_3)_2$), muscovite ($(\text{K},\text{Na})(\text{Al},\text{Mg},\text{Fe})_2(\text{Si}_{3.1}\text{Al}_{0.9})\text{O}_{10}(\text{OH})_2$), quartz (SiO_2), calcite ($\text{Ca}(\text{CO}_3)$) and microcline maximum (KAlSi_3O_8). These components are stable minerals and difficult to undergo chemical reactions with water. Hence, the water in the saturated block samples of this experiment influences the physical properties of the block most.



(a)



(b)



(c)

Fig. 4-1 Quantitative analysis from profile-fitted peaks by XRD

The percentage of each component of the three blocks is shown in Table 4-1.

Table 4-1 The component percentage of the rock samples

Sample number	Dolomite	Muscovite	Quartz	Calcite	Microcline maximum
1	91.10%	2.80%	0	3.70%	2.40%
2	91.20%	3.80%	2.40%	1.50%	2.10%
3	92.30%	3.40%	0.50%	0	3.80%

4.1.2 Material preparation

The rock blocks were divided at 4 different particle size groups. The broken rock is prepared in the following steps.

Firstly, sieves of four kinds of sizes was used to sieve these rock blocks. They are screened by 4 groups with the size of 0 ~ 5 mm; 5 mm ~ 10 mm; 10 mm ~ 15 mm and 15 mm ~ 20 mm, as shown in Fig. 4-2.



(a) 15 mm ~ 20 mm



(b) 10 mm ~ 15 mm



(c) 5 mm ~ 10 mm



(d) 0 mm ~ 5 mm

Fig. 4-2 Four particle groups with different particle size after screening

Secondly, the rock blocks at each particle size grade were mixed evenly according to the proportion given in Table 4-2.

Table 4-2 Particle size grade schemes of the broken rock samples

Particle grade schemes	Percentage of block mass in each particle size range (%)			
	0 mm ~ 5	5 mm ~ 10	10 mm ~ 15	15 mm ~ 20
	mm	mm	mm	mm
G1	25	25	25	25
G2	15	35	35	15
G3	35	15	15	35
G4	40	30	20	10
G5	10	20	30	40

The rock blocks in the caving zone is from the rupture of the immediate roof of the coal mine. Because the block size distribution of the immediate roof is random, five different kinds of grading size are considered in this study: the proportion of the size groups is homogeneous distribution (G1); the proportion of the large and small size groups is less than the middle size groups (G2); the proportion of the large and small size groups is more than the middle size groups (G3); the proportion of the size groups monotonously decreases with the size increasing (G4); and the proportion of the size groups monotonously increases with the size increasing (G5). According to the size grading from G1 to G5, the qualitative results of difficult size grading conditions' influence can be obtained. As for the certain percentage of the particle size in the caving zone, further study need to be carried out in the future.

Thirdly, make the rock block saturated. Because of the rock block components' stable chemistry, water can reduce the interaction between rock blocks, but no corrosion effect.

The rock block should be soaked in the waterborne dyes until it is saturated. To confirm the soaked time, 5 groups of rock block (shown in Fig. 4-3) was tested. They were immersed in the water and measured the weight every 20 minutes. When the mass

of the rock block is stable, it can be confirmed that the block has been absorbed sufficient moisture and reached saturation. The results of the rock block weight change are shown as Fig. 4-4.

As shown at Fig. 4-4, the weights of the rock blocks become to be stable after immersing one hour. To ensure the saturated of the blocks, every sample of broken rock is soaked in the waterborne dyes for 80 minutes.



Fig. 4-3 The sample of saturated time confirming test

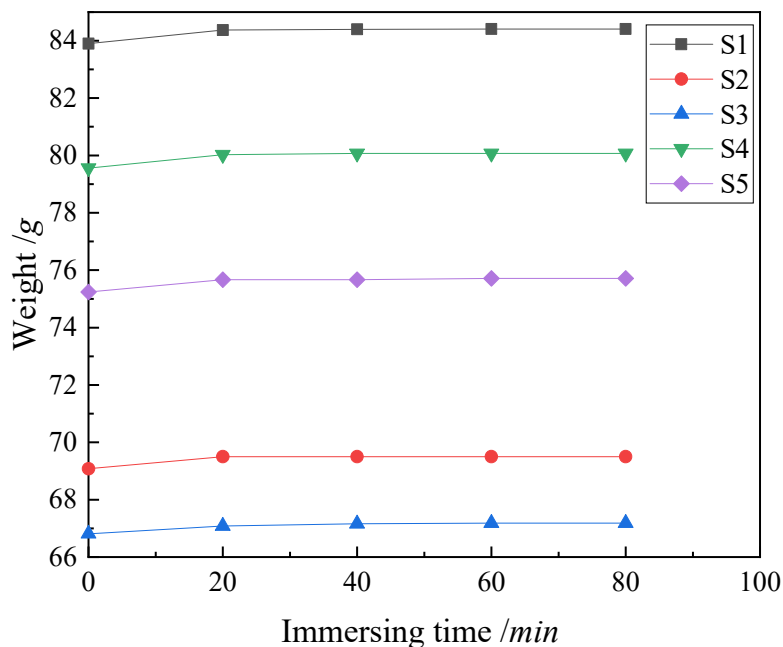


Fig. 4-4 The weight change at saturated time tests

4.1.3 Experimental apparatus

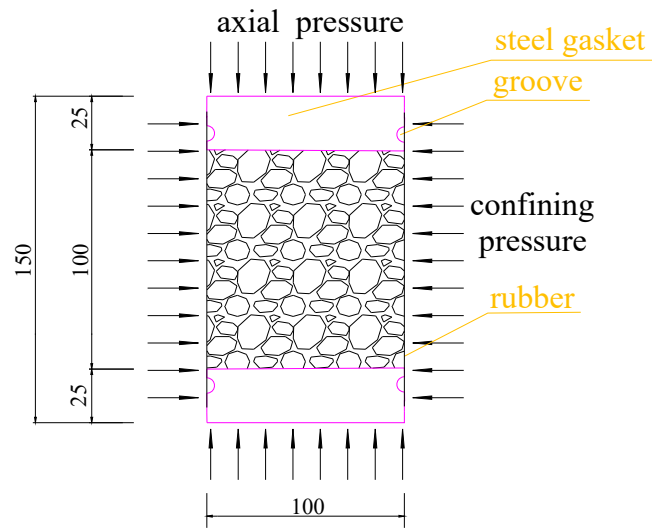
MTS815 Electrohydraulic Servo Rock Test System in China University of Mining and Technology was used to perform the triaxial compression creep test of broken rock, as shown in Fig. 4-5.



Fig. 4-5 Physical diagram of MTS815

The maximum diameter of the specimen that the apparatus can hold is 100 mm, and the maximum height is 200 mm. The minimum diameter of cylindrical specimen should be more than five times the size of the largest rock fragment in the specimen (Ulusay 2015). Considering the sample size requirement of MTS815, each broken rock sample has the scale with 100 mm (in diameter) \times 100 mm (in height) in this study. The confining pressure is applied by an oil hydraulic system and has the maximum capacity of 45 MPa. The maximum of the axial pressure is 1,700 kN. The schematic of broken rock sample is shown in Fig. 4-6.

As shown in Fig. 4-6, there are two steel gaskets to ensure the vertical direction of the axial pressure in each sample. Unconsolidated broken rock blocks were wrapped by rubber membrane. As the broken rock block need to stay saturated, the rubber membrane also can be used to seal in the moisture of the saturated rock block. The rubber membrane can be fixed together with the steel gasket by tying the steel wire into the groove of the steel gasket.



(a) Schematic diagram of the sample



(b) Photo of the sample

Fig. 4-6 Schematic of the sample design

4.1.4 Experimental procedure

According to the description of above subsection, the whole triaxial compressive creep test consists of the 5 steps, including rock block preparation, sample saturation, sample consolidation, creep loading and particle sieving.

4.2 Creep results of broken rock under triaxial compression test

4.2.1 Gradation loading

There are two commonly used loading methods for rock creep experiments: separate loading and gradation loading. The separate loading method is easy to be influenced by the heterogeneity of each sample of materials on the test results. Gradation loading can avoid the influence of irregular rock samples on creep deformation, but the deformation of the subsequent stage load includes the creep deformation produced by the previous stage load.

Because the gradation loading method is easy to operate and can save the test time, it is well used by rock tests. Chen, et al proposed Chen's loading method for creep data processing of gradation loading (Chen, 1991; Yang 2011). This creep data proposing method takes the loading history into consider and enable to get the one-time loading

creep curve when $\sigma_n = \sum_{i=1}^n \Delta\sigma_i$ for step loading with step distance $\Delta\sigma$. To meet the

requirements of Chen's loading method, the creep deformation should enter the stable creep stage when doing next level of loading, and the loading step distance should be the same. Fig. 4-7 shows the stress loading curve of Chen's loading method.

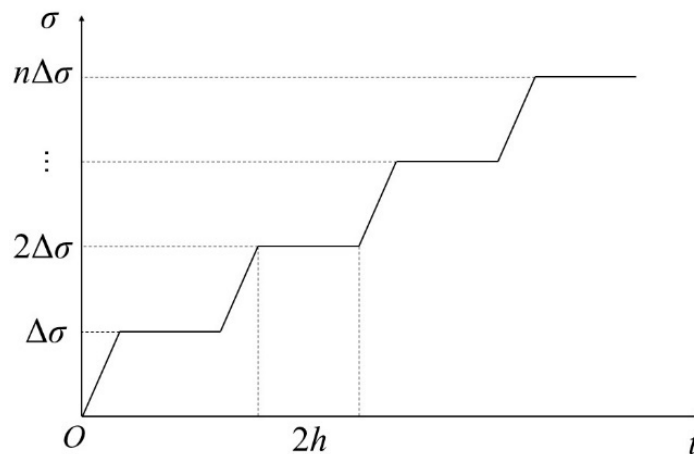


Fig. 4-7 Stress loading path of the Chen's loading method

4.2.2 Creep results of broken rock

The influence of particle size grading, confining pressure and axial pressure on the

broken rock creep behavior was studied. The confining pressure was changed as 2 MPa, 3MPa and 4 MPa, respectively. According to a large amount creep results of the broken rock, the axial strain curve is hard to reach the accelerated creep stage like an intact rock sample due to the large void ratio (Wang et al. 2018; Li et al. 2020; Ma et al. 2014). The axial pressure is set as 2 MPa, 4 MPa, 6 MPa and 8 MPa, respectively.

The creep results of each sample of gradation loading under different confining pressure and size grading are shown as Figs. 4-8 and 4-9.

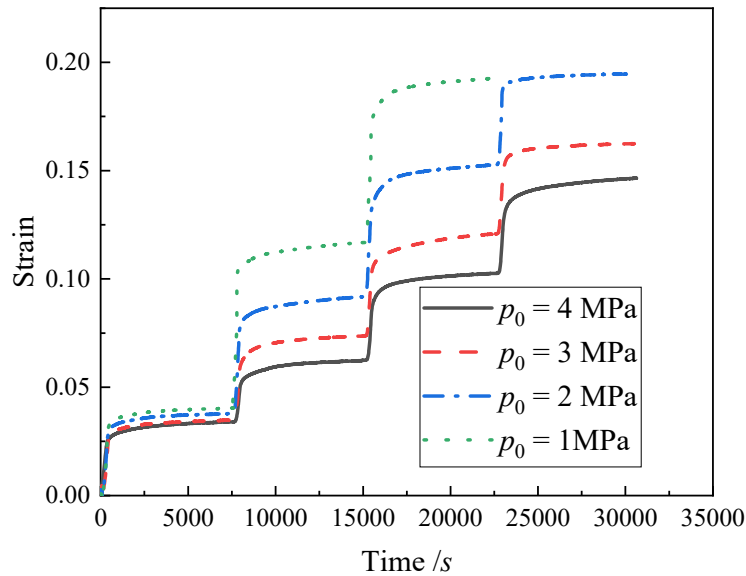


Fig. 4-8 Strain time curve of broken rock undergoing different confining pressure

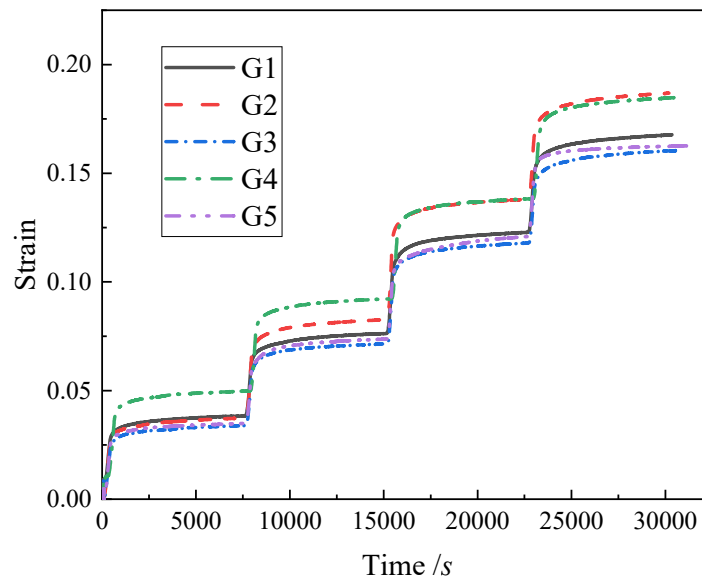
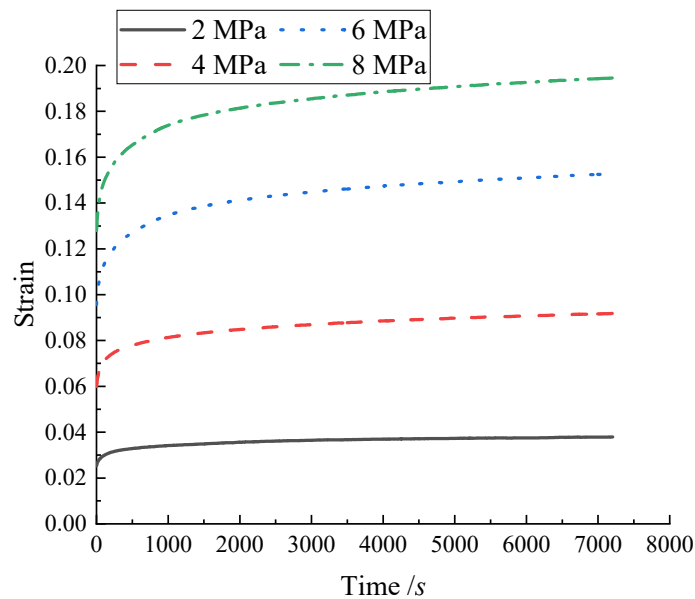


Fig. 4-9 Strain time curve of broken rock undergoing different size grading

As the maximum displacement in this experiment was set as 20 mm, the apparatus will stop automatically when axial displacement is more than 20 mm. In that case, it is hard to add the fourth loading when the confining pressure is 1 MPa, which results in the lack of the creep data of the rock undergoing the confining pressure of 1 MPa and the axial pressure of 8 MPa.

As shown in Figs. 4-8 and 4-9, the strain time curve rises as a shape of step, and under each level of load, the broken rock exhibits instantaneous deformation and stable deformation, and more than 90% of the overall deformation is elastic deformation.

According to the Chen's loading method, the creep data of this test was disposed, and the final brock rock creep data under different confining pressure and size grading is shown in Fig. 4-10. Because the creep results with confining pressure 1 MPa was lack the data when axial pressure was 8 MPa, this data was not analyzed to compare with other confining pressure's results.



(a) $p_0 = 2 \text{ MPa}$

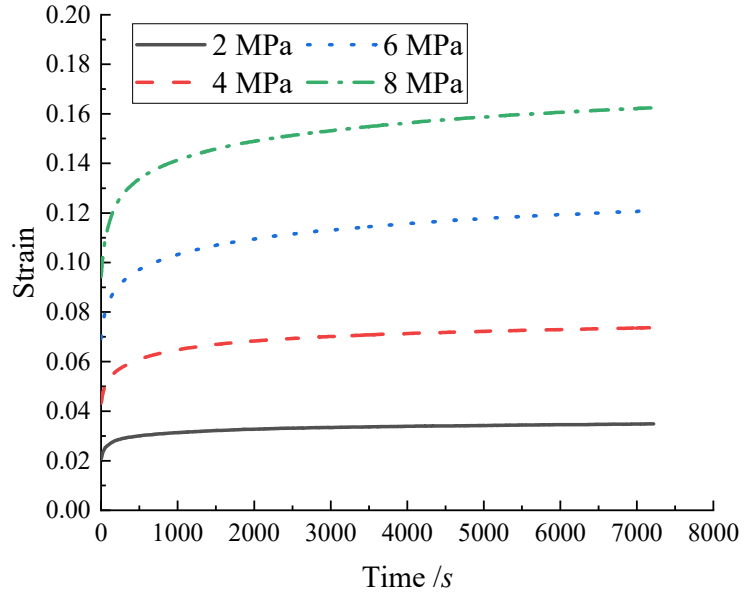
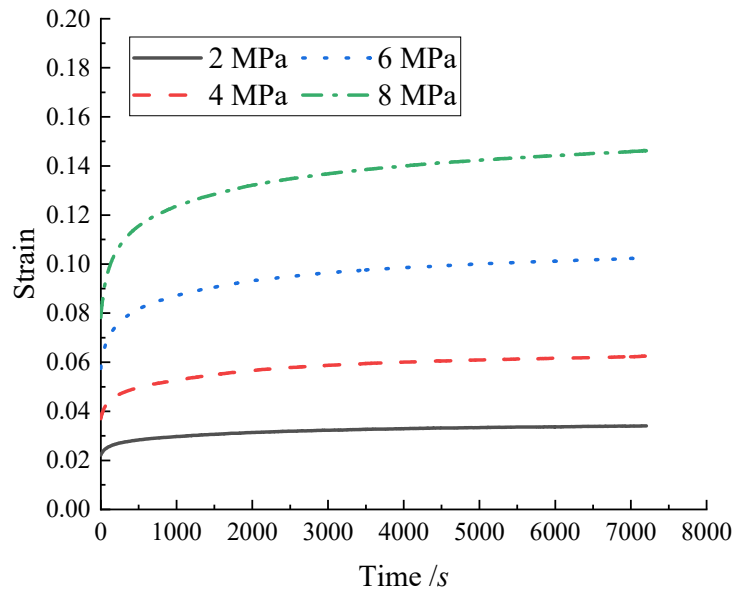
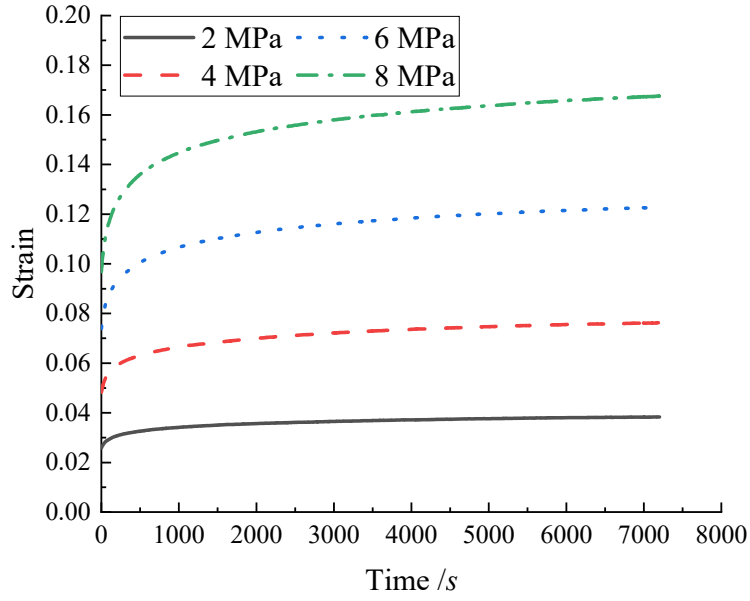
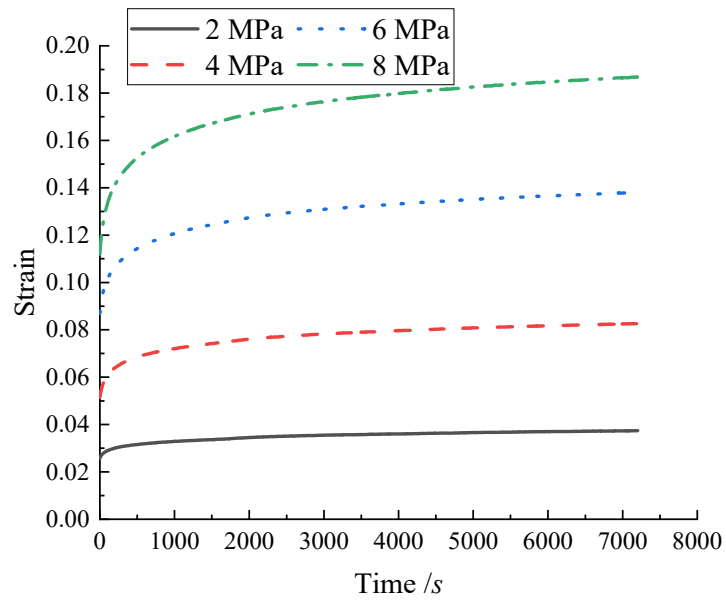
(b) $p_0 = 3$ MPa(c) $p_0 = 4$ MPa

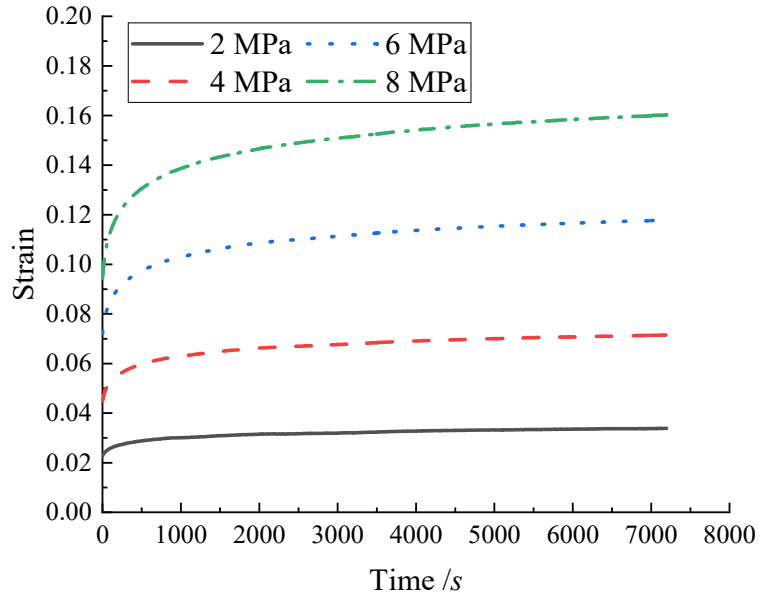
Fig. 4-10 Creep curve of broken rock under different confining pressure



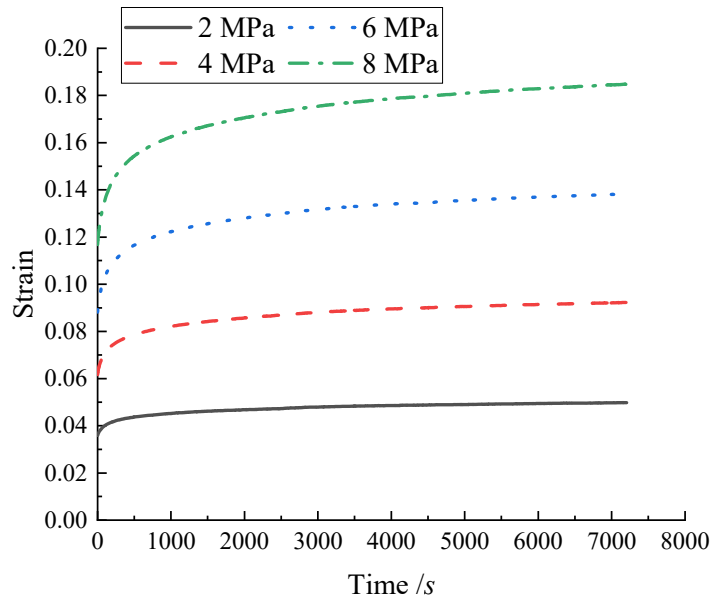
(a) size grading G1



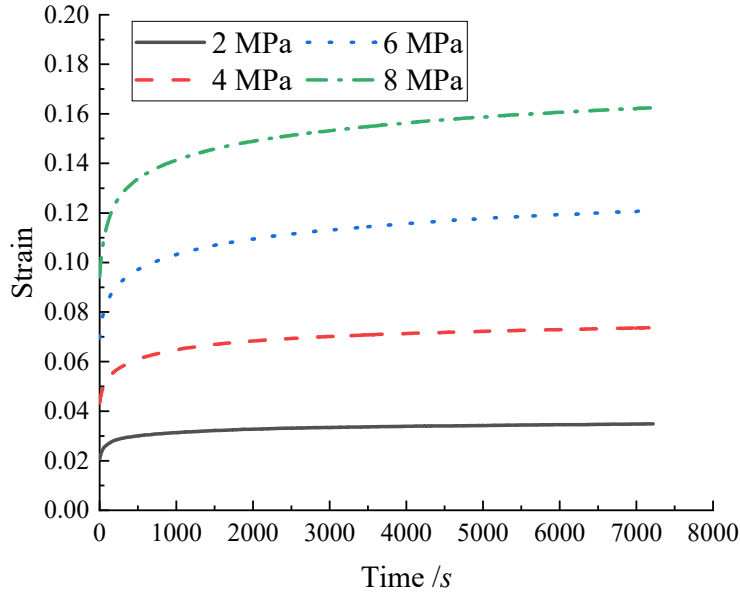
(b) size grading G2



(c) size grading G3



(d) size grading G4



(e) size grading G5

Fig. 4-11 Creep curve of broken rock under different size grading

As shown in Figs. 4-10 and 4-11, the creep strain is increased with the increase of axial pressure. There are two stages of broken rock creep curve, accelerating creep stage and stable creep stage. The time entering the stable stage is increasing with the axial stress. Also, according to Fig. 4-10, when the axial pressure is the same, as the confining pressure increases, the maximum creep decreases gradually. When the confining pressure is increased from 2 MPa into 4 MPa, the maximum creep value is reduced by 0.0484, 0.0502, 0.0294 and 0.0039, respectively, while the decreasing ratio is 24.9%, 32.87%, 31.92% and 10.97%, respectively.

To future explore the creep characteristics of the broken rock, take the sample with the size grading G5 and the confining pressure 3 MPa as an example, and its creep strain rate is shown in Fig. 4-12.

According to Fig. 4-12, the strain rate sudden decreases at the beginning of the creep loading. At the initial loading time, the rock block in the broken rock impacted by the loading changing will redistribute, which causes the sudden change of strain rate. Then, it is gradually stable and fluctuated in a small degree at 0. However, the time when the creep strain rate is getting stable is increase with axial pressure.

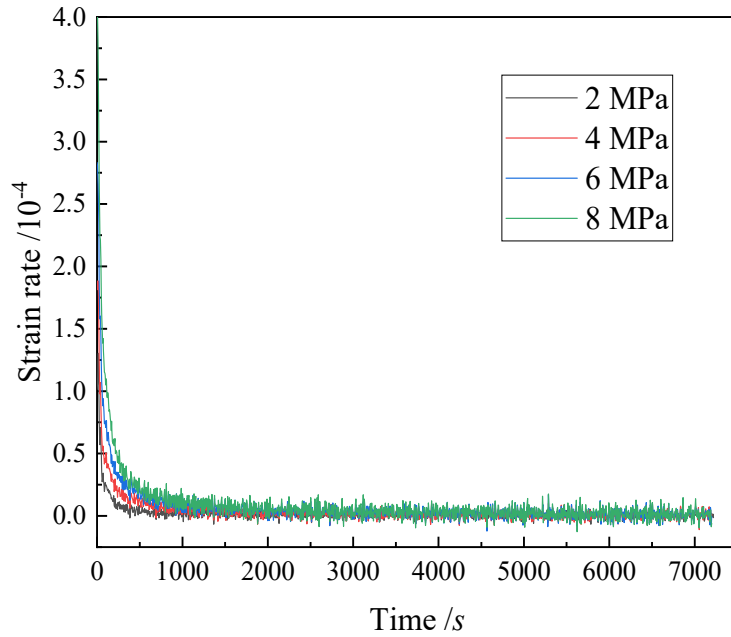


Fig. 4-12 Creep strain rate curve of broken rock with size grading G5 and $p_0 = 3$ MPa

4.3 Particle breakage characteristics of broken rock under triaxial compression loading

Aiming at the fourth reason caused the error of the subsidence prediction model of caving zone: The rock blocks was assumed that they were not broken again. Hence, the breakage law of the broken rock under the creep loading is studied.

4.3.1 Introduction of particle breakage indexes

Particle breakage indexes have been proposed by many researchers based on the particle size distributions before and after the compression test (Hang 2019; Hardin 1985; Marsal 1967; Shi 2018; Lade 1996; Lackenby 2007). According to a series of compression tests on broken rock material and sand, the breakage potential B_p was defined as the area between the particle size distribution curve and the 0.074 mm line, while the change area of the size grading curve before and after the test was defined as the total breakage B_t (Hang 2019; Hardin 1985). Then, the relative breakage index B_r can be calculated by dividing the total breakage using the breakage potential B_p , illustrated in Eq. (4-1) (Hardin 1985).

$$B_r = \frac{B_t}{B_p} \quad (4-1)$$

The relative breakage index putted forward by Hardin is one of the most useful tools to evaluate the breakage degree of the fragmentation of the broken rock (Hang 2019; Hardin 1985). The diagram of the relative breakage index is shown in Fig. 4-13.

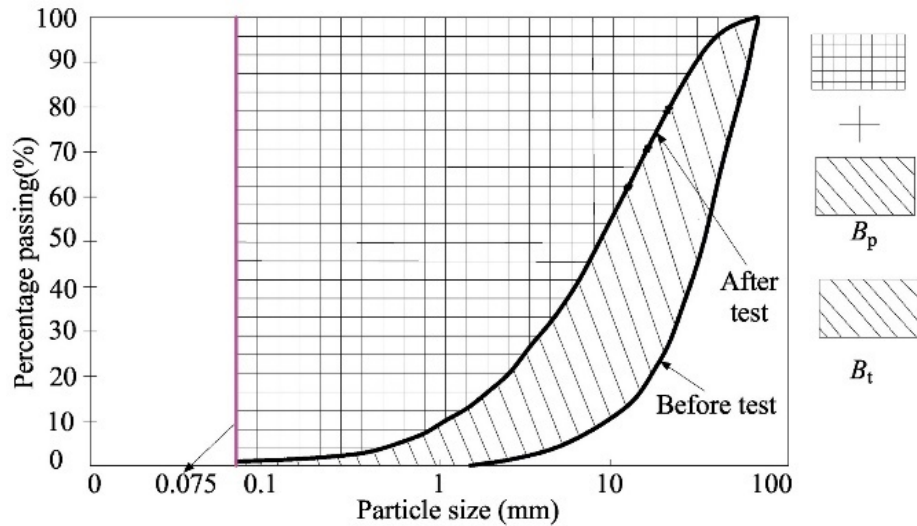
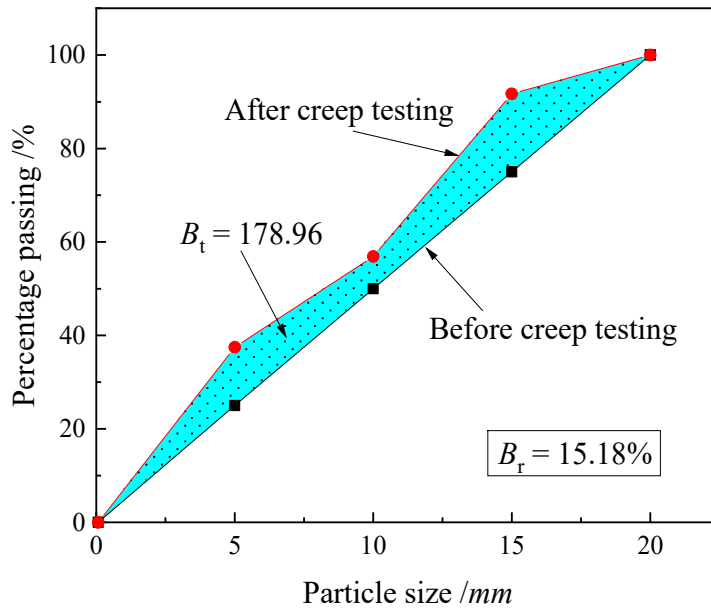


Fig. 4-13 Definition of the relative breakage index B_r (Hang et al. 2019)

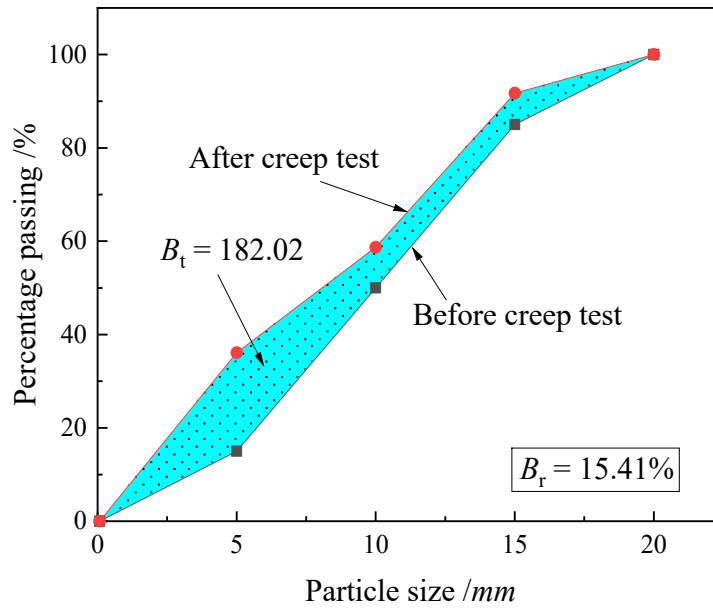
4.3.2 Particle breakage characteristics of broken rock under different grading size index

According to the definition, the relative breakage indexes of different size grading in creep tests are calculated and shown in Fig. 4-14.

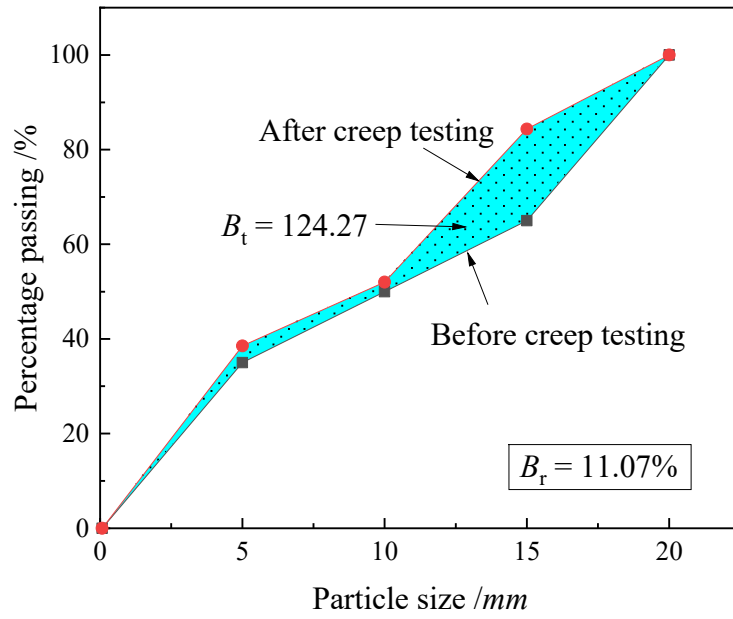
As shown in Fig. 4-14, size grading of broken rock impacts the total breakage B_t and the relative breakage index B_r . The change in particle size in the range of 0 ~ 10 mm is greater than the change in the range of 10 mm ~ 20 mm, in cases that the particle size grading is G2 and G4. On the contrary, when the particle size grading is G1 and G3, the creep compressive test changes the rock block with particle size in range 10 mm ~ 20 mm more. In cases that particle grading size is G5, the total breakage is the largest, and the change of each particle size range is almost the same.



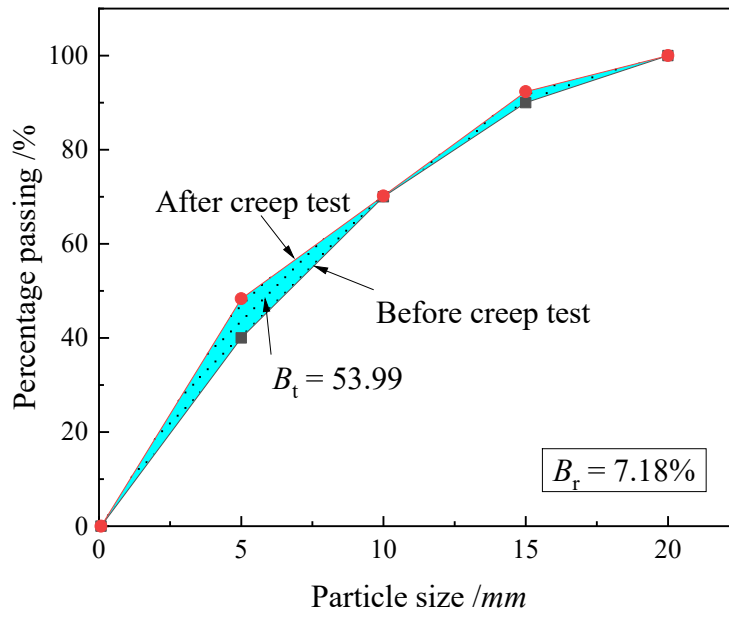
(a) Size grading G1



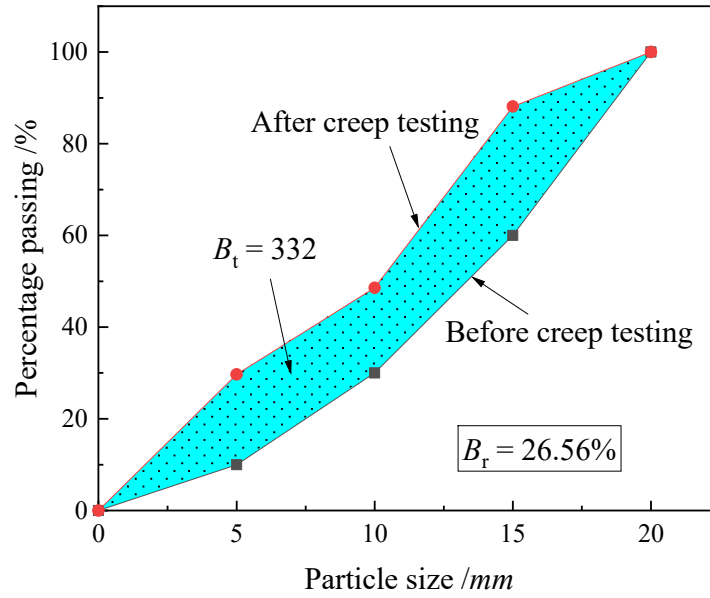
(b) Size grading G2



(c) Size grading G3



(d) Size grading G4



(e) Size grading G5

Fig. 4-14 Relative breakage indexes of broken rock under different size grading

To compare the relative breakage index of different particle size grading clearly, put the particle size distribution and the relative breakage index of each size grading in the same figure, as shown in Fig. 4-15.

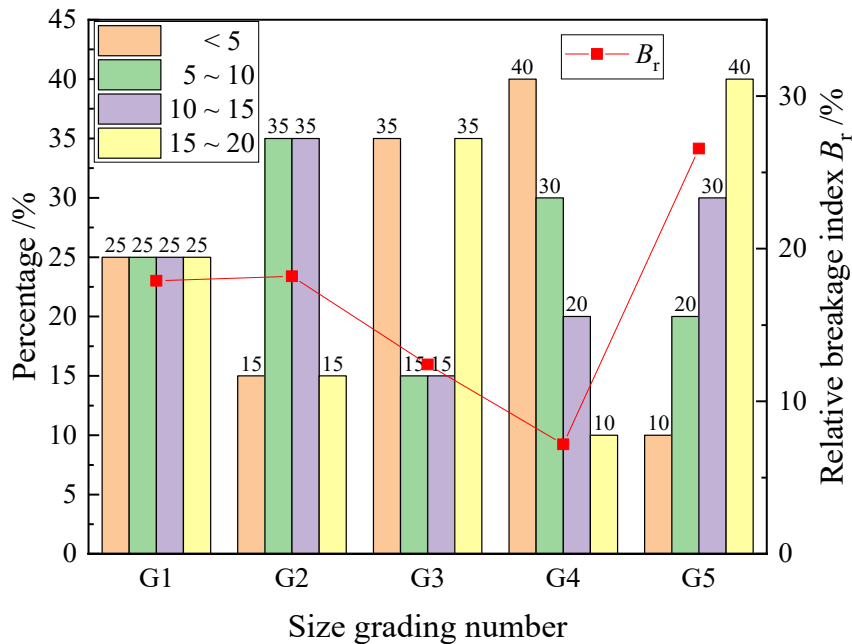


Fig. 4-15 Relative breakage index of different size grading after creep test

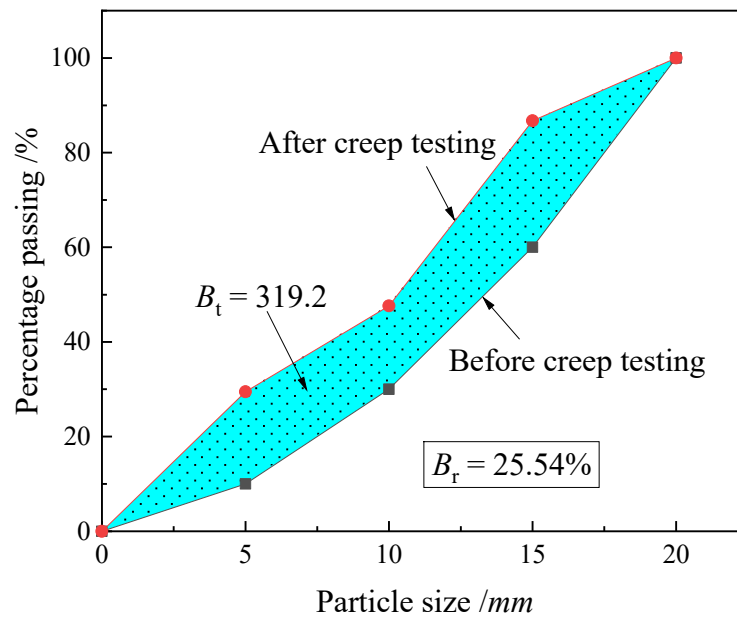
As shown in Fig. 4-15, as large-size particles are more likely to be crushed in creep

experiments than small-size particles, the relative breakage index is the largest when the proportion of particles increases monotonously with the particle size (G5). Also, when the proportion of particles reduces monotonously (G4), the relative breakage is the smallest. Compared with size grading G1, G2 and G3, if the particle size proportion is bigger at the edge size grading group (G3), its relative breakage index B_r is smaller than that of the size proportion smaller at the edge size grading group (G2) and the size proportion same of each size grading group. According to the results of breakage index, the most unstable size grading is G5, while the most stable size grading is G4.

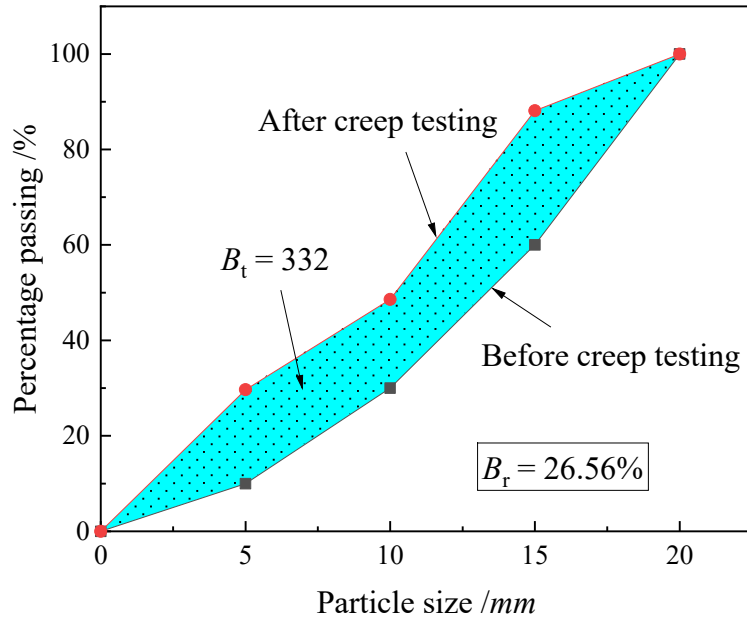
4.3.3 Particle breakage characteristics of broken rock under different confining stress

The breakage characteristics can be influenced by confining pressure. The results of breakage index under different confining pressure is shown in Fig. 4-16.

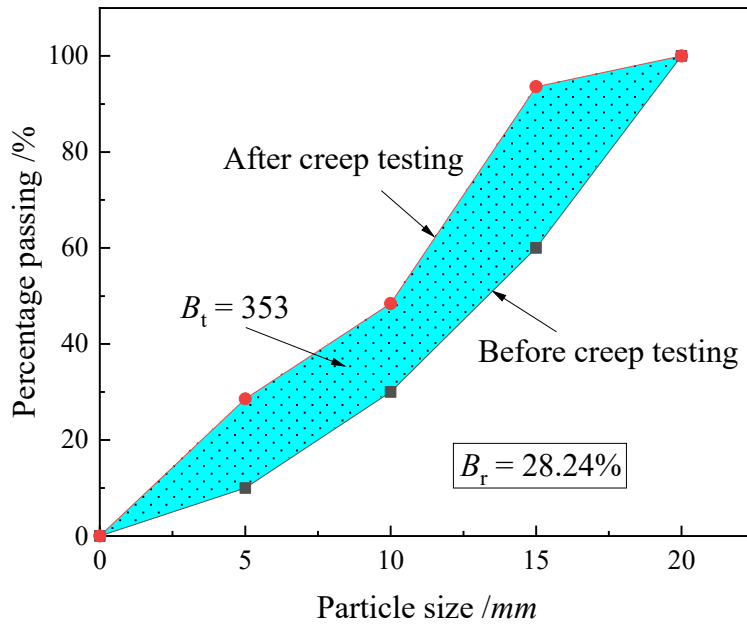
According to Fig. 4-16, the breakage index reduced with confining pressure increasing. The larger the confining pressure was, the more difficult the broken rock deformed, which caused the results that there were less large size rock particles broke and divided into small size. Hence, it is reasonable to say that the broken rock is more stable at a certain high confining pressure.



(a) Confining pressure is 2 MPa



(b) Confining pressure is 3 MPa



(c) Confining pressure is 4 MPa

Fig. 4-16 Relative breakage indexes of broken rock under different confining pressure

The relative breakage index B_r is related to the break degree of the rock mass, and the break degree is related to the bulking coefficient which is an important parameter of the caving zone deformation properties. The change law of the bulking coefficient under triaxial creep loading will be discussed in Chapter 5. Generally, the larger the

relative breakage index is, the easier the rock blocks in the caving zone break by the creep loading of the surrounding rock mass.

The size of the rock blocks in the caving zone is always more than 1 m. Due to the limitation of this experiment small scale, it is difficult to get the quantitative relation between the deformation of the caving zone and the relative breakage. The further study of the large-scale rock block need be carried out in the future to get more precise relation between the breakage index and the caving zone deformation.

If the mining technology and the overburden characteristics is confirmed in a certain mining field, the size grading of its caving zone can be determined, and this law of relative breakage index in different confining pressure and size grading can be used.

4.4 Summary

(1) An experiment method was proposed and held on to study the broken rock's creep behavior under triaxial compression test in this study. It included five parts: rock block preparation, sample saturation, sample consolidation, creep loading and particle sieving. By using this experiment method, the creep curves and breakage indexes under different grading size, confining pressure and axial pressure were obtained.

(2) The broken rock experiences instantaneous deformation and stable deformation, and more than 90% of the overall deformation was elastic deformation. The time entering the stable stage was increasing with the axial stress. As the confining pressure increasing, the maximum creep decreased gradually. When the confining pressure increased from 2 MPa into 4 MPa, the maximum creep value was reduced by 0.0484, 0.0502, 0.0294 and 0.0039, respectively, while the decreasing ratio is 24.9%, 32.87%, 31.92% and 10.97%, respectively.

(3) The relative breakage index was the largest when the proportion of particles increased monotonously with the particle size. When the proportion of particles reduced monotonously, the relative breakage would be the smallest. The most unstable size

grading was in the case that the size increases monotonous, while the most stable size grading was when the size decreases monotonous. The breakage index reduced with confining pressure increasing.

Reference

- Chen ZJ, Kang WF, Huang JP. Sealing stress, creep, expansion and constitutive equation of rock. *Chinese Journal of Rock Mechanics and Engineering*. 1991,10(4):299-312. (In Chinese)
- Hang YL, Li JM, Ma D, et.al. Triaxial compression behaviour of gangue solid wastes under effects of particle size and confining pressure. *Science of the Total Environment* 2019;693:133607.
- Hardin B. Crushing of soil particles. *J Geotech Eng* 1985;111:1177-1192.
- Lackenby J, Indraratna B, McDowell G, and Christie D. Effect of confining pressure on ballast degradation and deformation under cyclic triaxial loading. *Géotechnique* 2007;57:527-536.
- Lade PV, Yamamuro JA and Bopp PA. Significance of particle crushing in granular materials. *J Geotech Eng* 1996;122:309-316.
- Li M, Zhang JX, Meng GH, Gao Y, Li AL. Testing and modelling creep compression of waste rocks for backfill with different lithologies. *International Journal of Rock Mechanics and Minings Sciences* 2020;125:104170.
- Ma Z, Gu R, Huang Z, Peng G, Zhang L, Ma D. Experimental study on creep behavior of saturated disaggregated sandstone. *International Journal of Rock Mechanics and Minings Sciences* 2014;66:76-83.
- Marsal RJ. Large-scale testing of rockfill materials. *J Soil Mech Found Div* 1967;94:1042-1047.
- Shi Y, Gan L, Li XB, He SY, Sun C, Gao L. Dynamics of metals in backfill of a phosphate mine of Guiyang, China using a three-step sequential extraction technique. *Chemosphere* 2018;192:354-361.
- Sun CL, Li GC, Gomah ME, Xu JH, Sun YT. Creep characteristics of coal and rock investigated by nanoindentation. *International Journal of Mining Science and Technology* 2020;30(6):769-776.
- The ISRM suggested methods for rock characterization, testing and monitoring: 2007-2014. In: Ulusay R C, Editor. Springer Press, 2015.
- Wang C, Lu Y, Hao G, Cui B, Zhao Z. Simulated test on compression deformation
-

characteristics and mechanism of fractured rock in mined out area. *Geotech Geol Eng* 2018;36(5):2809-2821.

Yang WD, Zhang QY, Chen F et al. Research on Nonlinear Rheological Model of Diabase and Processing Method of Creep Loading History. *Chinese Journal of Rock Mechanics and Engineering*. 2011,30(7):1405-1413. (In Chinese)

CHAPTER 5

5 Prediction of broken rock bulking coefficient based on particle discrete element method

Based on the results of Chapter 4, it can be found that the time effect behavior of rock blocks is complicated and not only deformation but also rock blocks itself are broken due to the loading. Herein, a numerical simulation tests was carried out to obtain the rock blocks inside visible results and the change law of the bulking coefficient which can reflect the bulking degree of rock mass.

Since the breakage rule of the broken rock in the caving zone was discussed in Chapter 4, further study of the quantitative bulking characteristics still needs to be carried out. As an important coefficient to reflect the bulking degree, the bulking coefficient plays an important role in prediction the deformation of the caving zone. It can be calculated as:

$$K = \frac{V_r}{V_s} \quad (5-1)$$

where K is the bulking coefficient; V_r is the volume of the whole broken rock; and V_s is the total volume of each rock fragment.

Because V_r and V_s change all the time with the compressive loading, it is difficult to monitor them during the experiment process. At this case, it is necessary to study the bulking coefficient law by numerical simulation method. In addition, numerical simulation can also provide the visible information of the inside rock blocks deformation.

5.1 Establishment of the particle numerical model

The broken rock of a caving zone above goafs undergoes loading from surrounding rock and overburden, which leads to changes in the bulking coefficient. Hence, the broken rock in the caving zone is under stress from x , y and z directions. It is necessary

to study the time effect and change laws of broken rock bulking coefficient in the overburden caving zone under ground stress conditions.

5.1.1 Boundary profile of rock fragments in particle mechanical model

In mining sites, the rock fragment shapes of broken rock are various (Feng and Wang 2020; Fan and Liu 2017; Yavuz 2004). The occlusion between the rock fragments inhibits its slippage and rotation, which affects the overall deformation of the rock mass. During the simulation by particle discrete elements, the ball, as the basic element, is a standard sphere, which makes it difficult to simulate the slippage, occlusion and fragmentation between rock blocks in a broken rock sample. Therefore, it is necessary to generate numerical block elements with irregular shapes.

To obtain the geometry of the rock block, a 3D laser scanner, Reeyee X5 was used to scan four kinds of gangues obtained from the goaf in the coal mine (Xiao et al. 2020). The scanning results were the basis for generating the geometric contours of the clump element in the numerical simulation. The scanning geometric shapes and fragment templates are shown in Fig. 5-1. When establishing the numerical model, the size of each rock block is set by Fish code based on these four kinds of geometric template.

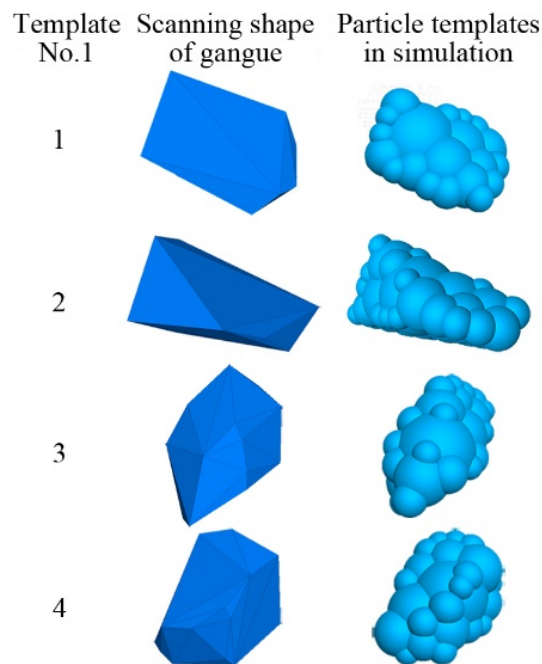


Fig. 5-1 Gangue scanning geometry and rock fragment templates in simulation

5.1.2 Deformation and damage criterion of rock fragments in particle mechanical model

According to the error cause discussion of the subsidence prediction model of the caving zone in Subsection 3.3.2, the failure of the rock blocks during the loading should be considered in the numerical simulation study.

To simulate the deformation and failure of rock blocks, all the pebbles in rigid clumps were transformed into corresponding balls with the same radius and position by Fish code. These balls were connected by the parallel bonds and could rotate and move. The parallel bonds would be broken when the gap between two balls at the ends was larger than a certain value, that is, a crack was formed inside this rock block. In that case, the rigid clump was transformed into a flexible cluster which may be deformed and destroyed. The contact between balls within the same cluster was parallel bond contact model, which could resist tension, pressure and bending moment, while the contact between balls within two contiguous clusters was linear contact model, which could only resist pressure.

The shapes of the gangue rock fragment are irregular and the basic elements of the cluster are balls, so there is totally different overlaps between balls inside the cluster inevitably, resulting in that the event 'bond_break' in PFC5.0 is harder to occur than expected (Potyondy and Cundall 2004). Hence, the contact broken condition should be reset.

The theory of maximum elongation linear strain, also termed the second strength theory, states that no matter what the stress states, when the maximum elongation linear strain reaches the material ultimate strain value at a certain point, the material undergoes brittle fracture. When the linear strain of the contact is greater than the ultimate strain value, that is, $\varepsilon_u > [\varepsilon_u]$, the contact mode is changed from a linear parallel bond model into a linear model, and then the bond breaking is realized. At this time, the contact no longer resists the tension and the relative torsion of the balls at both ends, indicating that the rock block is damaged inside at the same position with the broken contact. The deformation diagram of the contact is shown in Fig. 5-2.

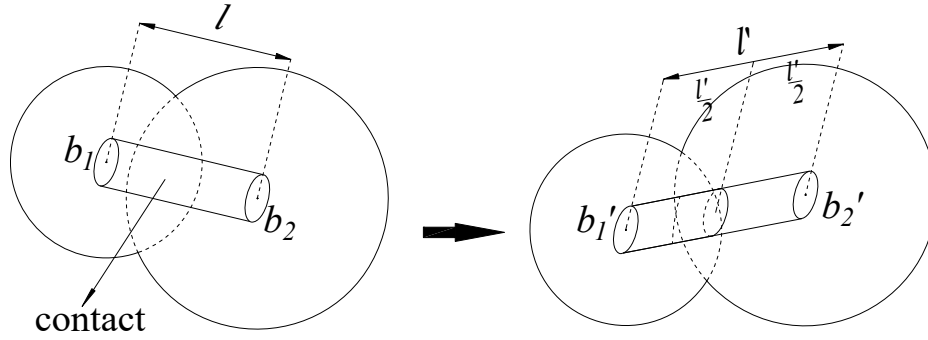


Fig. 5-2 The deformation of contact inside the gangue rock-block

The equation of calculating the contact linear strain of rock material is given by

$$\varepsilon_u = \frac{l' - l}{l} \quad (5-2)$$

in which l' is the length of the contact at the new step; and l is the initial length of the contact.

Once breaking or failure occurred in the cluster, a new rock block with damage or two new smaller rock blocks are formed. Then, the next timestep is conducted until the further breaking.

5.1.3 Simulation of the time effect in particle mechanical model

To describe the macroscopic damage phenomena, it is necessary to analyse the micromechanical behaviours behind it. The time effect of rock material deformation can be considered as a macroscopic reflection of the stress gradually corroding the rock mass strength (Potyondy 2007). There are three bond-aging models which were used in particle discrete element (Potyondy 2007; Tran et al. 2009; Silvani et al. 2009), and the curves trend of them were explained in Subsection 1.1.3. All these three bond-aging models can be used to simulate rock mass creep with appropriate empirical parameters (Zhao and Song. 2015). Therefore, the bond-aging model proposed by Potyondy was utilized in this paper.

Based on stress corrosion theory in Potyondy's bond-aging model, the corrosion rate law for the bond diameter is described as follows (Potyondy 2007)

$$\frac{dR}{dt} = \begin{cases} 0 & \sigma < \sigma_a \\ -\beta_1 \exp(\beta_2 \frac{\sigma}{\sigma_c}) & \sigma_a \leq \sigma < \sigma_c \\ -\infty & \sigma_c \leq \sigma \end{cases} \quad (5-3)$$

in which R is the bond radius; β_1 and β_2 are constants related to the chemical environment and temperature; σ is the normal stress acting on the contact; σ_a is the threshold stress; and σ_c is the short-term normal strength of the contact.

According to Eq. (5-3), the bond radius multiplier of the particle mechanical model can be calculated by

$$\lambda_r = \begin{cases} 1 & \sigma < \sigma_a \\ -\beta_1 \frac{\Delta t}{R} \exp\left(\beta_2 \frac{\sigma}{\sigma_c}\right) & \sigma_a \leq \sigma < \sigma_c \\ 0 & \sigma_c \leq \sigma \end{cases} \quad (5-4)$$

in which λ_r is the multiplier of the bond radius; and Δt is the timestep.

5.1.4 Bulking coefficient monitoring in particle mechanical model

The volume of the broken rock at time t can be calculated by

$$V_t = \pi(Z_t - Z_p)r_s^2 \quad (5-5)$$

in which Z_t and Z_p are the height of the top and bottom loading plate, respectively; and r_s is the radius of the simulated model. The volume changes during loading, so Z_t , Z_p and r_s should be monitored and updated at each timestep.

According to the definition, the equation for calculating the bulking coefficient of the broken rock model based on the particle discrete element numerical simulation can be expressed by

$$K = \frac{\pi(Z_t - Z_p)r_s^2}{\sum_{m=1}^N V_{Pm}} \quad (5-6)$$

in which K is the bulking coefficient of the numerical model; N is the total number of rock fragments in the rock mass model; and V_{Pm} is the volume of the m^{th} rock fragment.

Implementing Eq. (5-6) by code into the numerical model, then the change law of the bulking coefficient K with time is enabled to be reported by the history command in PFC5.0.

5.2 Schemes

5.2.1 Model sizes

The minimum diameter of a cylindrical sample should be more than five times the size of the largest rock fragment in the sample (Ulusay 2015; ASTM standard 2013), and the ratio of grain size to sample height should be less than 0.1 (Aydan et al. 2014). Hence, a sample of the broken gangue rock established by the four kinds of block templates in Fig. 5-1 with a height of 300 mm and a bottom diameter of 200 mm was generated. The schematic of the gangue sample is shown in Fig. 5-3.

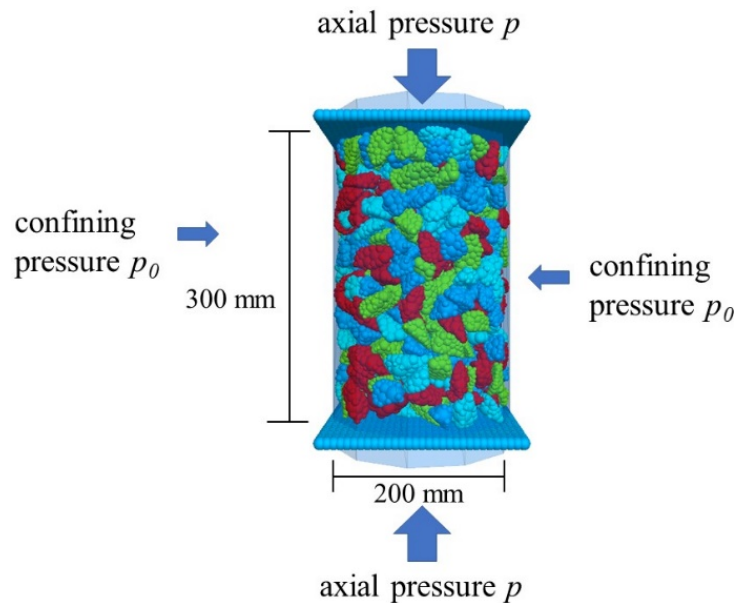


Fig. 5-3 The schematic diagram of the specimen and the loading plates

5.2.2 Loading process

To realize the constant triaxial compression loading of the numerical model, the axial pressure and the confining pressure were firstly set to be the same, and then were controlled by a servo mechanism system. However, if the loading plates use walls in PFC5.0 software directly, the pressure sometimes fluctuates and also it becomes

necessary to check each contact between the balls and walls at each timestep. To improve the accuracy of the axial loading and the calculation speed, after the servo system was balanced, two rigid loading plates in clump style were generated to replace the top and bottom walls. Then, the constant axial pressure was applied to the upper and lower loading plates, respectively, and the simulation of the constant loading of the broken gangue was realized, as shown in Fig. 5-3.

5.2.3 Modelling parameters

Liu did a series compression tests, point load split test and shear with variable angle to study the gangue mechanical parameters (Liu 2014). The gangue blocks were obtained from the No.12 Mine of China Pingmei Shenman Group whose shortest length of a side is shorter than 200 mm. Then he used these mechanical parameters to calibrate the meso-structure parameters of the gangue.

The meso-structure parameters of this numerical model referred to Liu's research, as shown in Table 5-1.

Table 5-1 Meso-structure parameters of the numerical model (Liu 2014).

Parameters	Values
Normal stiffness K_n (N/m)	6×10^9
Normal-to-shear stiffness ratio K_n/K_s	2.25
Contact normal stiffness K_n' (Pa/m)	6×10^9
Contact normal-to-shear stiffness ratio K_n'/K_s'	2.25
Friction coefficient μ	0.5
Contact tensile strength σ_c (Pa)	1×10^7
Contact shear stiffness τ_c (Pa)	5.5×10^7

The mechanical properties of the intact rock used to calibrate the meso-parameters are shown in Table 5-2.

Table 5-2 Mechanical parameters of the numerical intact rock model (Liu 2014).

Parameters	Values
Elastic modulus E (GPa)	5.08
Poisson's ratio μ	0.23
Compressive strength σ_c (MPa)	13.12
Tensile strength σ_t (MPa)	3.25
Cohesion c (MPa)	6.98
Friction angle φ ($^\circ$)	43.55

5.2.4 Specimens

Herein, the influences of size grading of the rock block, axial pressure and confining pressure on the deformation behavior of the broken rock over time were studied.

Talbot gradation index which is widely accepted by researchers can be used to describe the size gradation of the gangue broken rock (Talbot and Richart 2007; Wu et al. 2020). The ratio P of the mass M of the rock block with a size less than or equal to d in the sample to the total mass of the rock fragment M_t can be obtained by (Talbot and Richart 2007; Wu et al. 2018)

$$P = \frac{M}{M_t} = \left(\frac{d}{d_{\max}} \right)^n \quad (5-7)$$

in which n is the Talbot index; and d_{\max} is the maximum size of the clump. The gangue fragments were divided into four size groups: 10 mm~14 mm, 14 mm~18 mm, 18 mm~22 mm and 22 mm~26 mm. Each gradation group has the same proportion of the four kinds of geometry shown in Fig. 5-1.

Ten different samples of broken rock were generated, and properties of each sample are presented in Table 5-3. The geometry of each rock block in Fig. 5-1 of these ten samples was also randomly generated in the same proportion. Samples 1, 2, 3 and 4 could be used to study the influence of the size grading on deformation behavior of the broken rock. Samples 3, 5, 6 and 7 could be used to study the effect of axial stresses, while the effect of confining stress could be studied by samples 3, 8, 9 and 10.

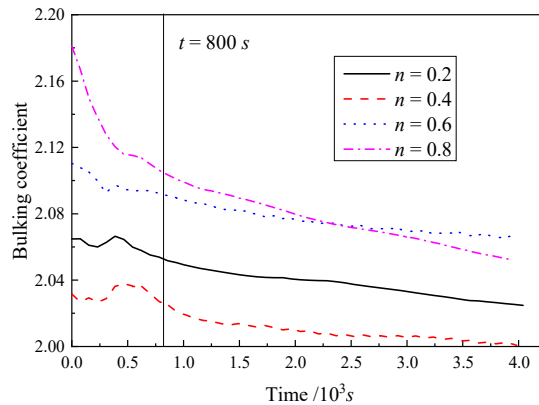
Table 5-3 Specimen schemes in particle discrete element numerical simulation

No.	Talbot grading index	Axial stress (MPa)	Confining stress (MPa)
1	0.2	30	3
2	0.4	30	3
3	0.6	30	3
4	0.8	30	3
5	0.6	15	3
6	0.6	20	3
7	0.6	25	3
8	0.6	30	1
9	0.6	30	2
10	0.6	30	4

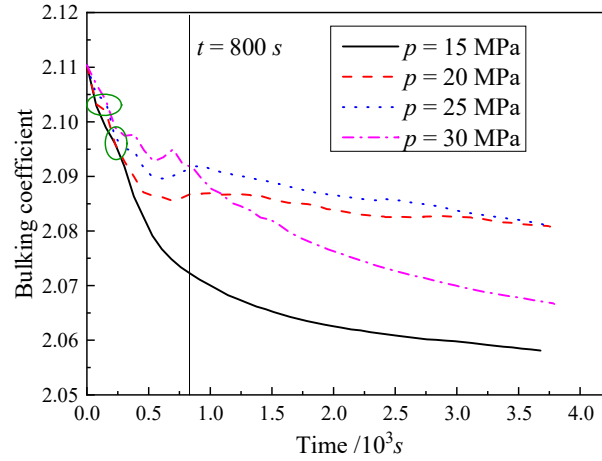
5.3 Change law of bulking coefficient

5.3.1 Bulking coefficient

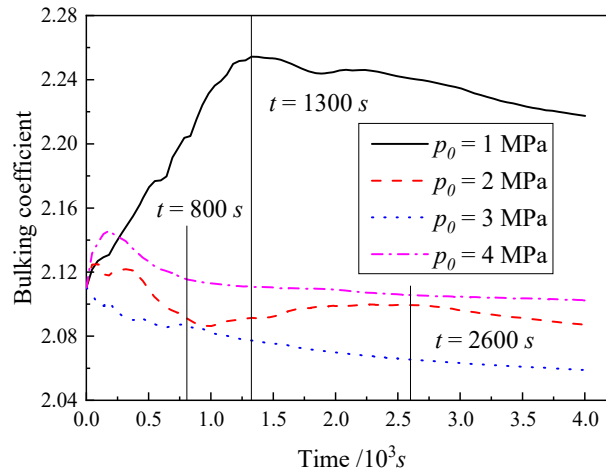
After balancing the servo system, the change law of the bulking coefficient over time during the loading process is shown in Fig. 5-4. The time began with the axial pressure applied at the upper and lower loading plates, the strain at this time was set as zero.



(a) Influence of Talbot grading index



(b) Influence of axial stress



(c) Influence of confining stress

Fig. 5-4 The changing curve of the bulking coefficient under different conditions

As shown in Fig. 5-4, before loading time is 800 s, the bulking coefficient of the broken rock was affected by the redistribution of the internal rock skeleton and had a particular fluctuation trend. When loading time exceeds 800 s, the rate of bulking coefficient decreasing became smaller, except that there was a gradual increase in the bulking coefficient, in Fig. 5-4(c), at $p_0 = 1$ MPa before $t = 1,300$ s and at $p_0 = 2$ MPa before $t = 2,600$ s. This was because the void rate of the broken rock declining with the redistributed of the rock blocks and made the broken rock more complex to deform further.

Fig. 5-4(a) shows the curve of bulking coefficient at different Talbot grading index. During the loading period, the curve $n = 0.4$ was always smaller than the other three gradation conditions. If the lithology of the rock blocks was the same, the value of the

bulking coefficient could reflect the density of the material, indicating that the model had the highest density at $n = 0.4$. High density could cause a small void ratio, resulting in small displacement and stable deformation. It was consistent with the theory of Talbot grading based on experimental studies, which proved that at $n = 0.4 \sim 0.6$, the material has the highest stability (Wu et al. 2018; Wu et al. 2019). Up to the loading time was 800 s, the curve of $n = 0.8$ was the most changed. After the loading time was 800 s, the rate of reduction of bulking coefficient of $n = 0.8$ was the highest, and this indicated that the density of $n = 0.8$ was the lowest case, and the void ratio was the highest one.

Fig. 5-4(b) shows the curves of the change in the bulking coefficient under different axial pressures. Up to the loading time was 800 s, except for $p = 15$ MPa, the bulking coefficient fluctuated to a certain extent, but the overall trend decreased rapidly. Except for the overlap of the three data points highlighted by the green ellipse in Fig. 5-4(b), the greater the axial pressure is, the smaller the bulking coefficient is. The curve of $p = 30$ MPa fluctuated twice, while the curves of $p = 25$ MPa and $p = 20$ MPa fluctuated once. The variation degree of $p = 25$ MPa was greater than that of $p = 20$ MPa. As for $p = 15$ MPa, there was no fluctuation, and the curve was monotonously decreasing. At the initial stage of loading, the greater the axial pressure of the broken rock is, the greater the effect on the sliding and occlusion of the rock fragment inside the broken rock is, resulting in increment of internal unbalance factors. After the loading time was 800 s, the void rate of the rock gets smaller, and the deformation of the rock fragments became dominated. The larger the external force on the rock is, the greater its volume changes is. Therefore, the slope of the bulking coefficient curve increased with the increasing axial pressure.

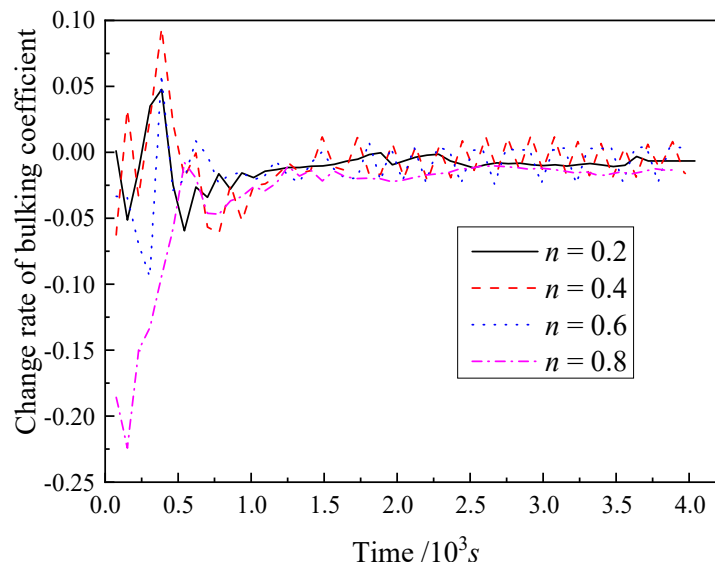
The influence of different confining pressure on bulking coefficient is illustrated in Fig. 5-4(c). When the restriction of the lateral deformation of the rock mass was weak, due to the lack of cementation between rock fragments, the rock mass tended to considerably expand in the lateral direction under a higher axial pressure. Therefore, the bulking coefficients of $p_0 = 1$ MPa before $t = 1,300$ s and $p_0 = 2$ MPa before $t = 2,600$ s tended to increase with time. When the expansion and deformation of the rock mass reached the peak values, the density of the rock mass become to be small, and the axial compression on the deformation was increased, resulting in the decrease of the

bulking coefficient. Therefore, the bulking coefficients of $p_0 = 1$ MPa and $p_0 = 2$ MPa reduced after they reached their peaks. The greater the axial pressure is, the greater the probability of lateral expansion deformation and the more difficult the axial deformation is, which would cause the volume fluctuates. In this situation, the correlation between the confining pressure and the bulking coefficient seems to be low. The bulking coefficient curve of $p_0 = 2$ MPa fluctuated between the curve of $p_0 = 3$ MPa and $p_0 = 4$ MPa, and the bulking coefficient when $p_0 = 4$ MPa was larger than that when $p_0 = 3$ MPa, while their tendency was the same.

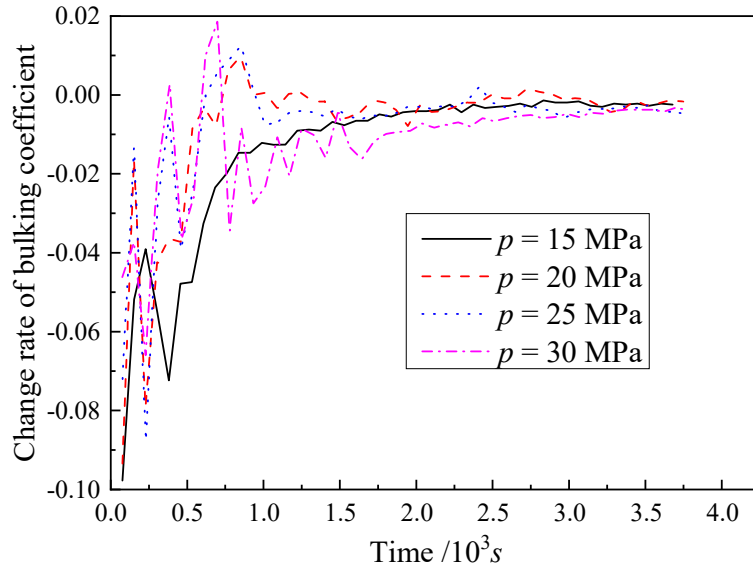
5.3.2 Change rate of the bulking coefficient

The curves of the change rate of the bulking coefficient under the influence of Talbot grading index, axial pressure and confining pressure are shown in Fig. 5-5.

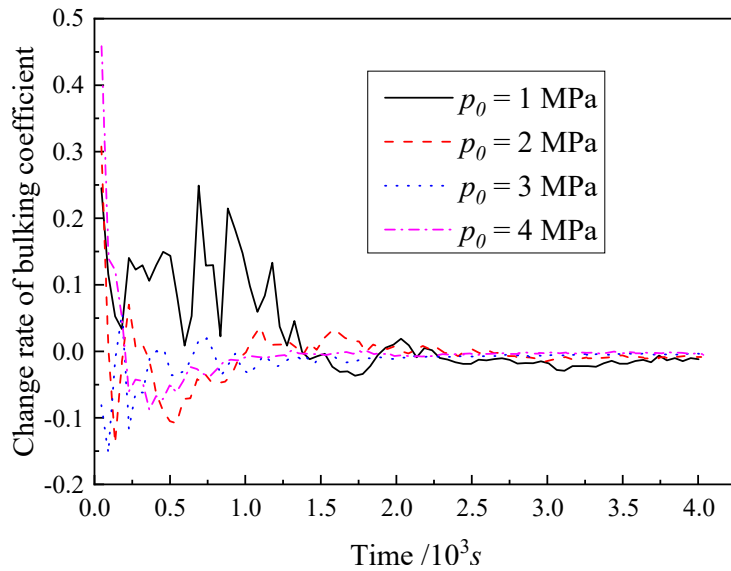
It could be found that the change rate of the bulking coefficient fluctuated significantly at the beginning of the loading in Fig. 5-5. This was related to the change of the particle arrangement caused by the rotation and re-occlusion of particles inside the rock fragment affected by external loads. Then, the change rate gradually stabilized and tended to approach zero, with the fluctuation between $-0.05/s$ and $0.05/s$.



(a) Influence of Talbot grading index



(b) Influence of axial stress



(c) Influence of confining stress

Fig. 5-5 Bulking coefficient change rate under different conditions

Fig. 5-5(a) shows the change rate of bulking coefficient of various Talbot gradation models. At the stabilization stage of deformation, compared to the sudden change of $n = 0.4$ and $n = 0.6$ models, the curves of $n = 0.2$ and $n = 0.8$ changed more smoothly, and the change rate of $n = 0.2$ was closer to zero. Fig. 5-5(b) presents the variation rate of bulking coefficient under the influence of axial pressures. The fluctuation range of the curve increased with the axial stress. Fig. 5-5(c) presents the change rate of bulking coefficient under the influence of confining pressure. At the initial loading stage, the

fluctuation time of the change rate curve decreased with the increasing confining pressure. At the later stage, the curve was more stable at $p_0 = 3$ MPa and $p_0 = 4$ MPa.

5.3.3 Deformation inside rock blocks

To help deeply understand the deformation of the broken rock, visualized illustration of the deformation of the rock blocks is necessary. Take Specimen No.3 in Table 5-3 as an example, a 2D cut figure of the specimen is shown in Fig. 5-6.

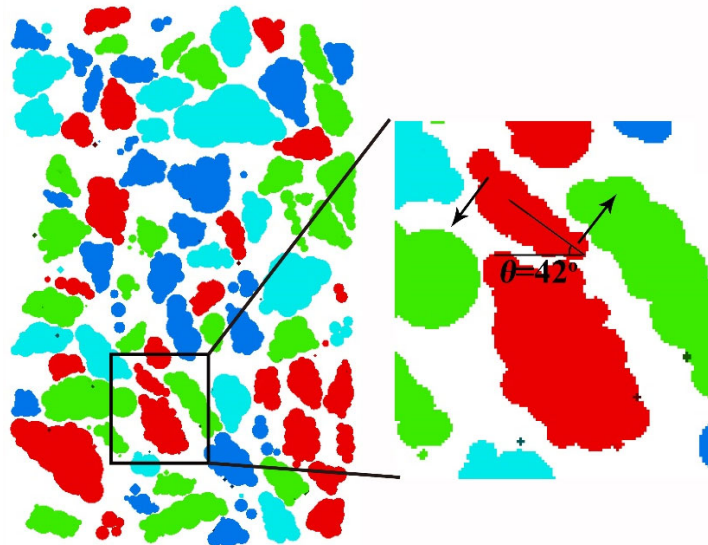


Fig. 5-6 2D cut of Specimen No.3

Considering the complex deformation between the broken rock blocks, only one rock block was taken for analysis, as shown in Fig. 5-6. The initial angle θ between this rock block and the horizontal direction was 42° . Influenced by its interaction with the surrounding rock blocks, it tended to rotate counterclockwise.

Fig. 5-7 illustrates the deformation of the studied rock block and the surrounding blocks at different time.

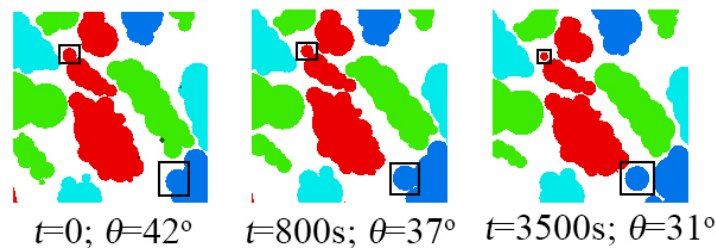


Fig. 5-7 Deformation of the researched rock block with time increasing

According to the deformation of the particle in the black box shown in Fig. 5-7 at different time, the rock located on the edge of the rock block could be easily damaged, which leads to an increase in the Talbot grading index. In addition, the angle between the studied rock block and the horizontal line gradually decreased. For the first 800 s, this rock block turned 5° counterclockwise, and then it took 2,800 s to rotate 6° anticlockwise. As the compression time increased, the rotation speed of this rock block slowed down. The rapid change of the rock block before 800 s could explain why the bulking coefficient fluctuated at the initial loading stage.

5.3.4 Internal force distribution of the broken rock

The contact force between the contiguous balls in a numerical rock fragment reflects the internal force distribution of the rock mass. Take Specimen Nos. 1, 2, 3 and 4 in Table 5-3 as examples, the internal force of each numerical broken rock model at the same time of the deformation stability stage is shown in Fig. 5-8.

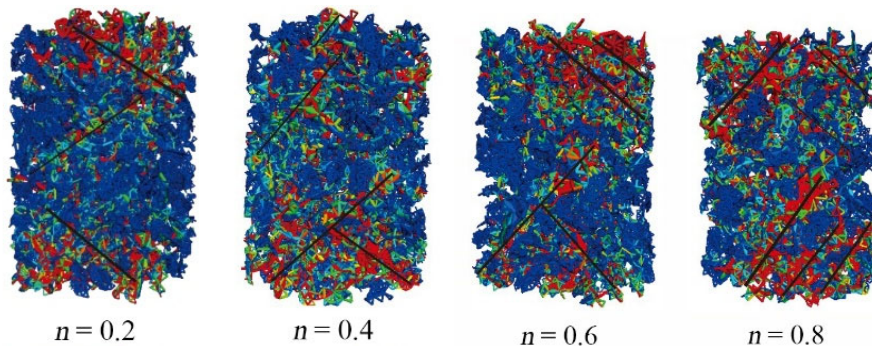


Fig. 5-8 The block internal contact force distribution under different Talbot grading index

The same legend was used in the four figures in Fig. 5-8, but the largest contact force was different. The red colored zone meant the contact force was equal or larger than 0.9 kN, and the blue colored zone presented that the contact force was between 0 and 0.1 kN. The direction of the black line described the track of higher force area inside the model, and the thickness of the line qualitatively represented the magnitude of the force.

As shown in Fig. 5-8, the high-stress area was the smallest in case of $n = 0.2$, while the high-stress area was the largest in case of $n = 0.8$. Combined with Fig. 5-5(a), change rate of the bulking coefficient was the smallest in case of $n = 0.2$, and it was the

largest in case of $n = 0.8$, but both had small fluctuations. Therefore, the larger the internal force is, the larger the change rate of the bulking coefficient is.

The distribution of the contact high-force zone reflects the possible failure trend of the material. The trend of the numerical model high-stress zone was a straight line with a particular inclination, which was similar to the crack propagation shape of the intact sandstone in the triaxial compression creep failure state. Fig. 5-9 shows the fracture morphology in the intact coal under creep test with confining pressure (Zhang et al. 2020). Hence, the time-effect characteristics of the broken rock strain could be analogized to the creep characteristics of an intact rock specimen.

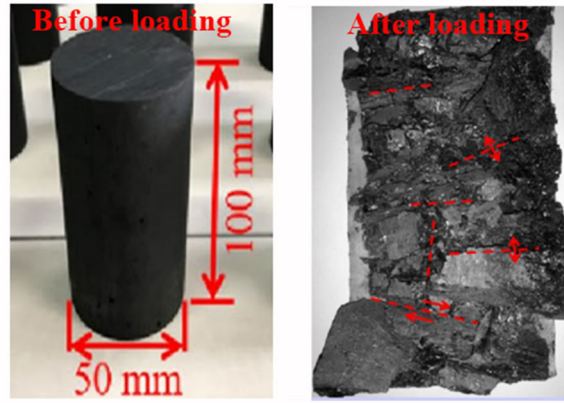


Fig.5-9 The morphology of intact coal before and after creep loading (Zhang et al. 2020)

5.4 Bulking coefficient calculation and prediction model

5.4.1 Calculation equation of bulking coefficient

The Burgers creep model is widely accepted to describe the creep processes of the viscoelastic body (Wang et al. 2015; Zou et al. 2013). In this chapter, it is used to describe the creep strain for the derivation of the bulking coefficient calculation equation.

The Burgers creep model can be expressed as (Zhao et al. 2019)

$$\varepsilon_z^c = \frac{\sigma_0}{E_2} + \frac{\sigma_0}{\eta_2} t + \frac{\sigma_0}{E_1} \left[1 - \exp\left(-\frac{E_1}{\eta_1} t\right) \right] \quad (5-8)$$

where ε_z^c is the creep strain; σ_0 is the stress of the rock specimen; η_1 and η_2 are viscosity coefficients; E_2 is the instant elastic modulus; and E_1 is the viscoelastic modulus.

The increment of bulking coefficient can be represented by the increment of strain. Assuming that the material obeys the small deformation theory, the bulking coefficient increment ΔK_P from t_1 to t_2 can be expressed as

$$\Delta K_P = \frac{(\varepsilon_{v2} - \varepsilon_{v1})V_1}{(1 + \varepsilon_{v1})V_P} = \frac{(1 + \lambda_x + \lambda_y)\Delta\varepsilon_z K_{P1}}{1 + (1 + \lambda_x + \lambda_y)\varepsilon_{z1}} \quad (5-9)$$

where ε_{v1} and ε_{v2} are the volumetric strain at t_1 and t_2 , respectively; V_1 is the volume of the broken rock at t_1 ; V_P is the total volume of rock fragments; λ_x is the ratio of the strain in the x-axis direction to the strain in the z-axis direction; λ_y is the ratio of the strain in the y-axis direction to the strain in the z-axis direction; $\Delta\varepsilon_z$ is the strain increment in the z-axis direction from t_1 to t_2 ; ε_{z1} is the strain in the z-axis direction at t_1 ; and K_{P1} is the bulking coefficient at t_1 .

Since the strain in the Burgers creep model is continuous and differentiable, Eq. (5-9) is continuous in time. Hence, assume that t_2 minus t_1 is infinitesimal, then Eq. (5-9) can be transformed as

$$K_P' - \frac{(1 + \lambda_x + \lambda_y)\varepsilon_z'(t)}{1 + (1 + \lambda_x + \lambda_y)\varepsilon_z(t)} K_P(t) = 0 \quad (5-10)$$

By solving the first order linear differential equation, Eq. (5-10) can be rewritten as

$$K_P(t) = K_0 \left[1 + (1 + \lambda_x + \lambda_y)\varepsilon_z(t) \right] \quad (5-11)$$

in which K_0 is the initial bulking coefficient.

Substituting Eqs. (5-8) into (5-11), the bulking coefficient can be calculated by

$$K_P(t) = K_0 \left[\sigma_0 (1 + \lambda_x + \lambda_y) \left(\frac{1}{E_2} + \frac{1}{\eta_2} t - \frac{1}{E_1} \exp\left(-\frac{E_1}{\eta_1} t\right) \right) + 1 \right] \quad (5-12)$$

5.4.2 Deformation characteristic parameter in the prediction model

The bulking coefficient is closely related to the deformation of the caving zone. Since the overburden will still deform for a long term after mining, it may affect the stability of the surface in the overtime. To early know the instability of the overburden and take appropriate control measures in time, it is necessary to predicate the bulking coefficient of broken rock mass in the caving zone.

However, it is difficult to obtain the proportionality coefficients of lateral strain to axial strain which changes with time. To solve this problem, a parameter related to the deformation anisotropy of material deformation named deformation characteristic parameter a was introduced, and set $a=1+\lambda_x+\lambda_y$. As λ_x and λ_y had the same direction, the deformation characteristic parameter a can reflect the difference between the lateral and axial strain.

Hence, Eq. (5-12) can be rewritten as

$$K_p(t) = K_0 [aQ(t) + 1] \quad (5-13)$$

in which $Q(t) = \sigma_0 \left(\frac{1}{E_2} + \frac{1}{\eta_2} t - \frac{1}{E_1} \exp\left(-\frac{E_1}{\eta_1} t\right) \right)$.

To explore the properties of the deformation characteristic parameter a and its influence on the prediction of the bulking coefficient, the curves of change in the deformation characteristic parameter a of the specimens in Table 5-3 are shown in Fig. 5-10.

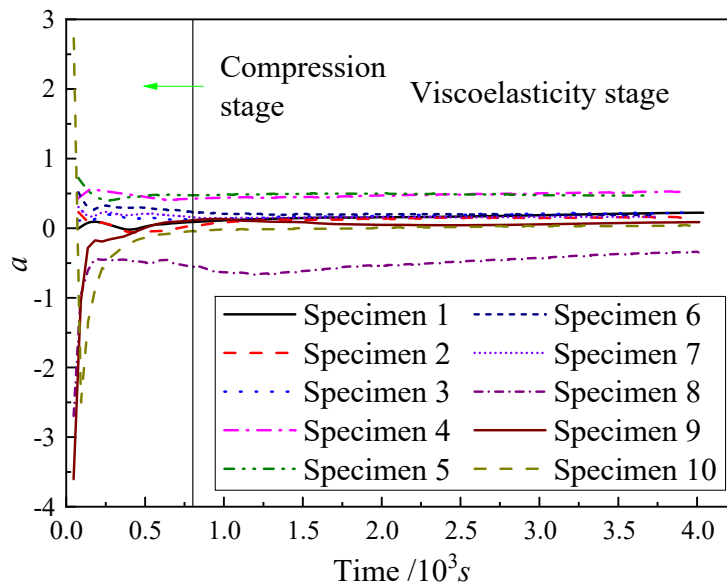
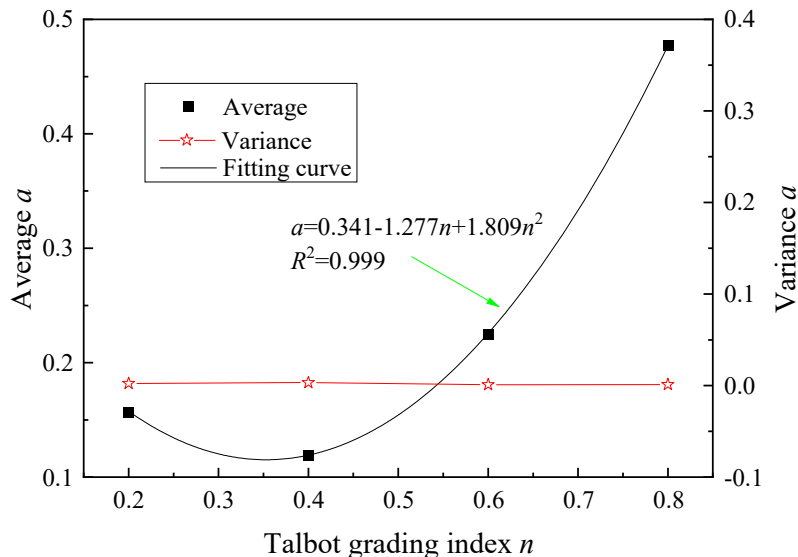


Fig. 5-10 Changing curves of deformation characteristic parameter a

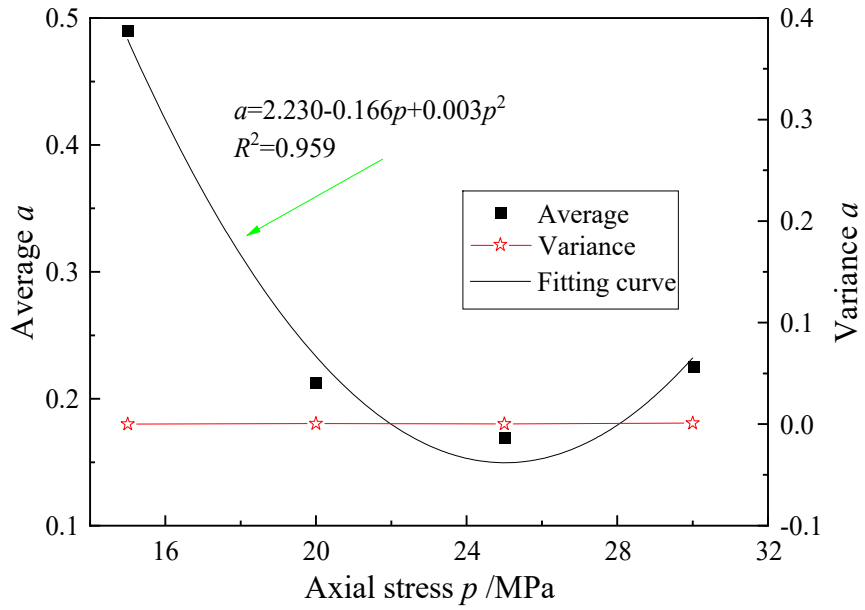
According to Fig. 5-10, at the initial loading stage, deformation characteristic parameter a changed a lot and then stable. According to the analysis of the bulking coefficient at Subsection 5.2.1, the broken rock was in the compaction stage before 800 s. Subsequently, the fluctuation of the deformation characteristic parameter a disappeared, and the curve was almost constant. The deformation rate of the rock mass become to be decreased, and the broken rock entered the viscoelastic deformation stage.

To understand properties of the deformation characteristic parameter a , the degree of fluctuation and its relation to various factors were studied. Because the lateral and axial strains are close to zero at the initial loading stage, the ratios of x-axial direction and y-axial direction to z-axial direction strain varies dramatically and the value of the deformation characteristic a is not constant. Therefore, it is reasonable to delete the initial three-point data at the beginning loading time when studying properties of the deformation characteristic parameter a . The average and variance deleted the initial three data of the deformation characteristic parameter a are shown in Fig. 5-11.

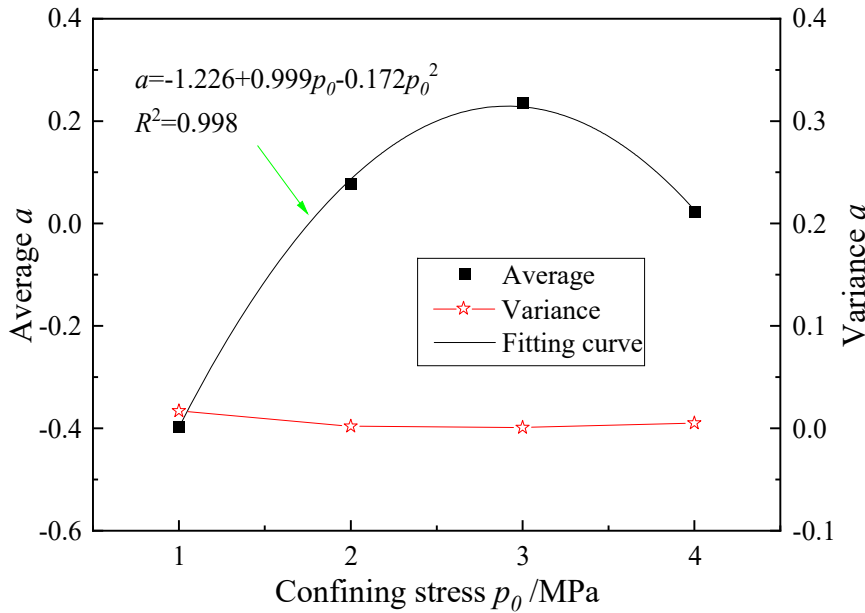
As shown in Fig. 5-11, There were quadratic functional relationships between the deformation characteristic parameter and Talbot grading index, axial pressure and confining pressure. The equations were $a=0.341-1.277n+1.809n^2$, $a=2.230-0.166p+0.003p^2$ and $a=-1.226-0.999p_0-0.172p_0^2$, respectively.



(a)



(b)



(c)

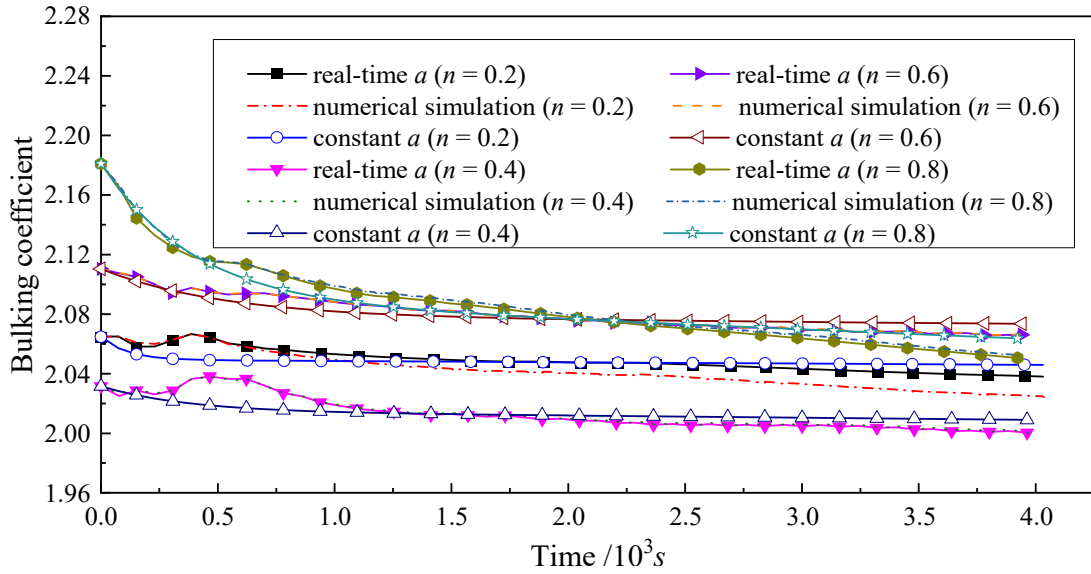
Fig. 5-11 Average and variance of a under the influence of different factors

5.4.3 Feasibility of bulking coefficient prediction

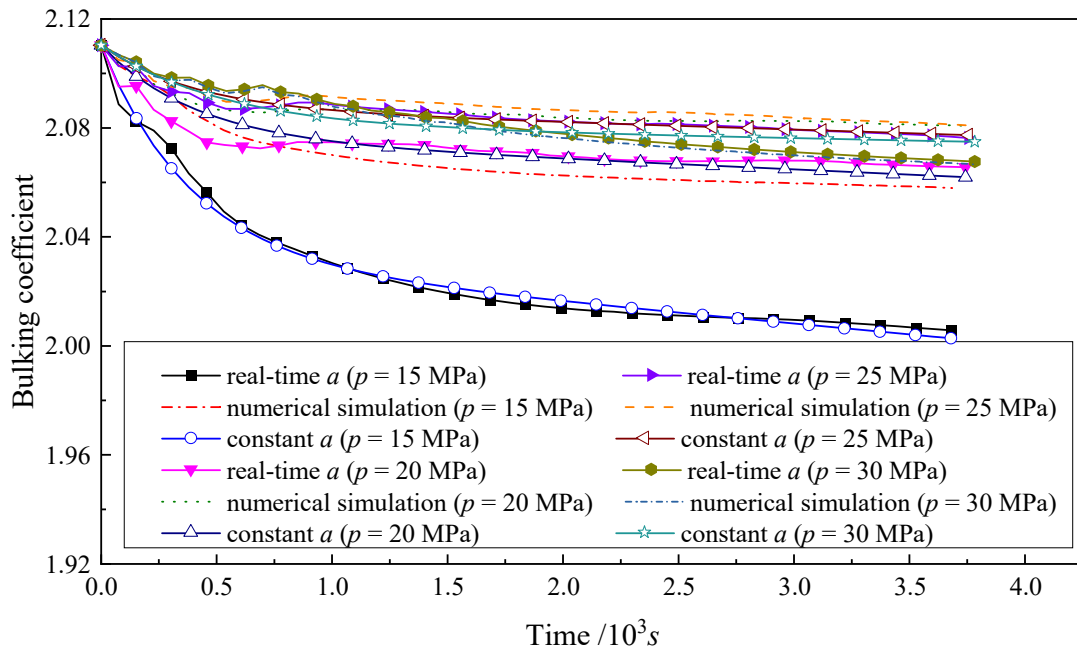
It is necessary to further study the influence of deformation characteristic parameter a on the accuracy of the bulking coefficient's calculation and prediction and prove the feasibility of predicting the bulking coefficient of the broken rock. Therefore, a constant value a was substituted into Eq. (5-13), and then compared with numerical simulation

results and the calculation results substituting real-time a . The constant a substituted this time was the average value obtained in Subsection 5.4.2.

Fig. 5-12 shows the comparison results of the bulking coefficient by the calculation model with real-time a , the numerical simulation method, and the calculation model with constant a . Hence, by analysing the difference between these three kinds of results, the necessity of accurate a could be studied.



(a) Talbot grading index



(b) Axial stress

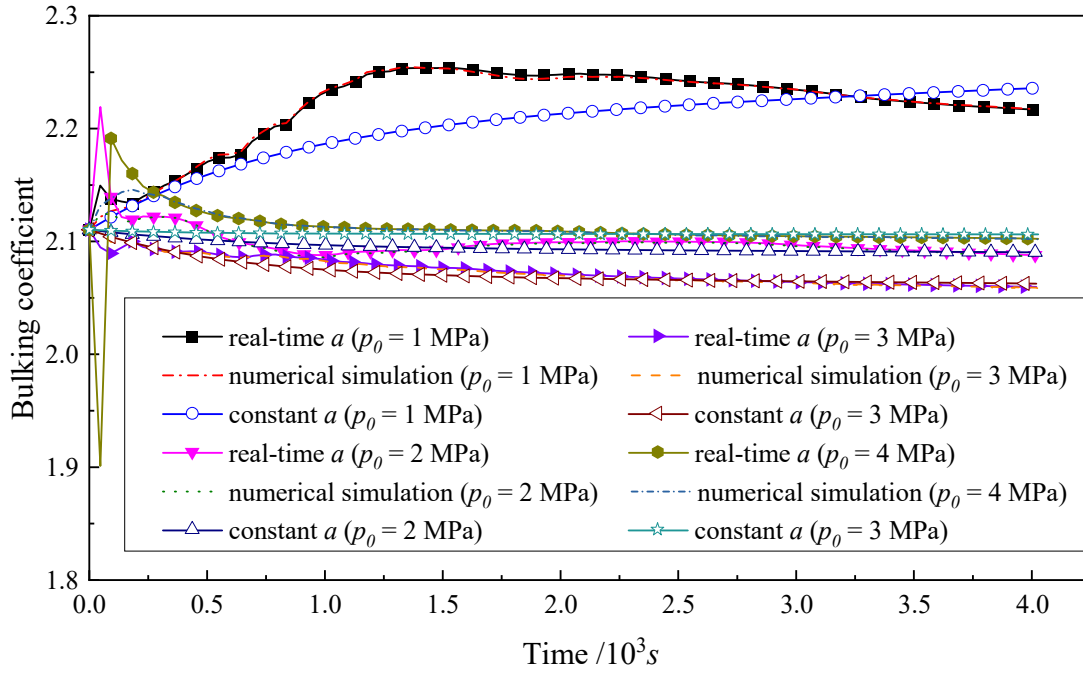


Fig. 5-12 Bulking coefficient results comparison based on different method

In the process of deriving the calculation equation of the bulking coefficient, when converting the increment of the bulking coefficient into the total value, it was assumed that the change of the bulking coefficient with time was continuous and derivable. In that case, the difference between the curves of numerical simulation and calculation results with real-time a was essentially the difference between the Burgers creep model and the simulated gangue broken rock creep results. As shown in Fig. 5-12, the results calculated by real-time a shows good agreement with the numerical simulation results, which further proved that the broken rock has viscoelastic properties, and its creep behavior fitted Burgers creep model well.

As shown in Fig. 5-12, if a was set to a constant value in the early loading stage, the fluctuation trend of the bulking coefficient was quite different from that of other two results. Therefore, the deformation characteristic parameter a could affect the fluctuation of the bulking coefficient. For the mid- and long-term prediction of the bulking coefficient, the curve trend of constant a is very similar to that of numerical simulation. When the confining pressure in Fig. 5-12(c) was 1 MPa, which was Specimen No. 8 in Table 5-3, the bulking coefficient increased abnormally at the beginning of loading. The fluctuating trends are different between the curves of the

constant a and the real-time a when p_0 is 1 MPa, so if the deformation characteristic parameter a of the material assumes to be constant, there will be a certain error. However, the maximum relative error was only 0.02. Therefore, when predicting the bulking coefficient at mid- and long-term, more than 1.0×10^3 s, a can be directly calculated by the fitting formulas in Fig. 5-11, $a=0.341-1.277n+1.809n^2$, $a=2.230-0.166p+0.003p^2$ and $a=-1.226-0.999p_0-0.172p_0^2$, and then the corresponding bulking coefficient can be obtained by Eq. (5-13).

5.5 Summary

(1) A three-dimension numerical model was established to represent the rock block of broken rock, considering the block damage and the time effect. A damage criterion of the rock fragment by particle discrete element was put forward. After analyzing the numerical simulation test data, a formula for calculating bulking coefficient and a prediction model were proposed.

(2) Before constant triaxial compression loading time was 800 s, the deformation of broken rock was in compaction stage, and the bulking coefficient decreased with a certain fluctuation. The fluctuation degree increased with the axial pressure and declined with the confining pressure. After 800 s, the deformation of broken rock entered the viscoelastic deformation stage, the bulking coefficient gradually monotonously decreased with time, and the change rate fluctuated between -0.05/s and 0.05/s. The rock block could be easily damaged at the protruding edge.

(3) Broken rock has obvious viscoelastic properties, and its creep behavior can be fitted by Burgers creep model. The proposed model for predicting the bulking coefficient was proved to be reliable and could be used for overburden stability analysis. The deformation characteristic parameter affected the fluctuation trend of the bulking coefficient at initial stage. It could be set as a constant for the mid- and long-term prediction of the bulking coefficient. There were quadratic functional relationships between the deformation characteristic parameter and Talbot grading index, axial pressure and confining pressure. The equations were $a=0.341-1.277n+1.809n^2$, $a=2.230-0.166p+0.003p^2$ and $a=-1.226-0.999p_0-0.172p_0^2$ respectively with the determination coefficients which were all less than 0.959.

Reference

- Aydan Ö, Ito T, Özbay U, Kwasniewski M., Shariar K., Okuno T., et al. ISRM suggested methods for determining the creep characteristics of rock. *Rock Mechanics and Rock Engineering* 2014;47(1):275-290.
- Fan L, Liu S. A conceptual model to characterize and model compaction behavior and permeability evolution of broken rock mass in coal mine gobs. *International Journal of Coal Geology* 2017;172:60-70.
- Feng G, Wang P. Simulation of recovery of upper remnant coal pillar while mining the ultra-close lower panel using longwall top coal caving. *International Journal of Mining Science and Technology* 2020;30(1):55-61.
- Liu Z. Compaction properties of gangue and its application in backfilling coal mining. Doctoral dissertation. Xuzhou: China University of Mining and Technology; 2014.p.61
- Potyondy D O, Cundall P A. A bonded-particle model for rock. *International Journal of Rock Mechanics and Mining Sciences* 2004;41(8):1329-1364.
- Potyondy DO. Simulating stress corrosion with a bonded-particle model for rock. *International Journal of Rock Mechanics and Mining Sciences* 2007;44(5):677-691.
- Standard A. C192: Standard Practice for Making and Curing Concrete Test Specimens in the Laboratory. Annual Book of ASTM Standards, ASTM International, West Conshohocken, PA 2013.
- Silvani C, Désoyer T, Bonelli S. Discrete modelling of time-dependent rockfill behaviour. *International Journal for Numerical and Analytical Methods in Geomechanics* 2009;33(5):665-685.
- Talbot A N, Richart F E. The strength of concrete and its relation to the cement, aggregate and Water. Bulletin No.137. University of Illinois: Urbana; 2007.
- The ISRM suggested methods for rock characterization, testing and monitoring: 2007-2014. In: Ulusay R C, Editor. Springer Press, 2015.
- Tran T-H, Vénier R, Cambou B. Discrete modelling of rock-ageing in rockfill dams. *Computers and Geotechnics* 2009;36(1-2):264-275.
-

- Wang X, Qu Z, Dou Y, Ma W. Loads of casing and cement sheath in the compressive viscoelastic salt rock. *Journal of Petroleum Science and Engineering* 2015;135:146-151.
- Wu JY, Feng MM, Mao XB, Xu JM, Zhang WL, Ni XY, et al. Particle size distribution of aggregate effects on mechanical and structural properties of cemented rockfill: experiments and modeling. *Construction and Building Materials* 2018;193:295-311.
- Wu JY, Feng MM, Ni XY, Mao XB, Chen ZQ, Han GS. Aggregate gradation effects on dilatancy behavior and acoustic characteristic of cemented rockfill. *Ultrasonics* 2019;92:79-92.
- Wu Y, Jing H, Yin Q, Yu LY, Meng B, Li S. Strength prediction model considering material, ultrasonic and stress of cemented waste rock backfill for recycling gangue. *Journal of Cleaner Production* 2020;276:123189.
- Xiao M, Ju F, He z, Li KY, Wang P. Experimental study on influence factors of the lateral pressure coefficient of gangue back-filling materials. *Journal of Mining and Safety Engineering* 2020;37(1):73-80.
- Yavuz H. An estimation method for cover pressure re-establishment distance and pressure distribution in the goaf of longwall coal mines. *International Journal of Rock Mechanics and Mining Sciences* 2004;41(2):193-205.
- Zhang L, Li X, Ren T. A theoretical and experimental study of stress–strain, creep and failure mechanisms of intact coal. *Rock Mechanics and Rock Engineering* 2020;53(12):5641-5658.
- Zhao YL, Wang YX, Wang WJ, Tang LM, Liu Q, Cheng GM. Modeling of rheological fracture behavior of rock cracks subjected to hydraulic pressure and far field stresses. *Theoretical and Applied Fracture Mechanics* 2019;101:59-66.
- Zhao Z, Song E-x. Particle mechanics modeling of creep behavior of rockfill materials under dry and wet conditions. *Computers and Geotechnics* 2015;68:137-146.
- Zou L, Wang S, Lai X. Creep model for unsaturated soils in sliding zone of Qianjiangping landslide. *Journal of Rock Mechanics and Geotechnical Engineering* 2013;5(2):162-167.

CHAPTER 6

6 Creep equation of broken rock in caving zone based on Fractional order theory

Creep is one of the important properties of rock rheology. It refers to the characteristic that the deformation of rock increases with time under the action of stable and continuous stress. Rock creep is an inherent characteristic of the rock itself, but it will change with the stress state it undergoes and the environment it is in. In fact, under the action of stable continuous stress, the rock deformation is divided into two parts. One is the instantaneous elastic deformation generated at the moment of loading, and the other is the creep deformation that gradually increases with time, as shown in Eq. (6-1). When building a rock creep constitutive model, not only the creep deformation must be represented, but also the instantaneous elastic deformation should be considered.

$$\varepsilon = \varepsilon_0 + \varepsilon(t) \quad (6-1)$$

where ε_0 is the instantaneous elastic strain; and $\varepsilon(t)$ is the creep strain.

6.1 Creep curves of broken rock in caving zone

The creep curves of standard rock material can be divided into three kinds of mode, as shown in Fig. 6-1.

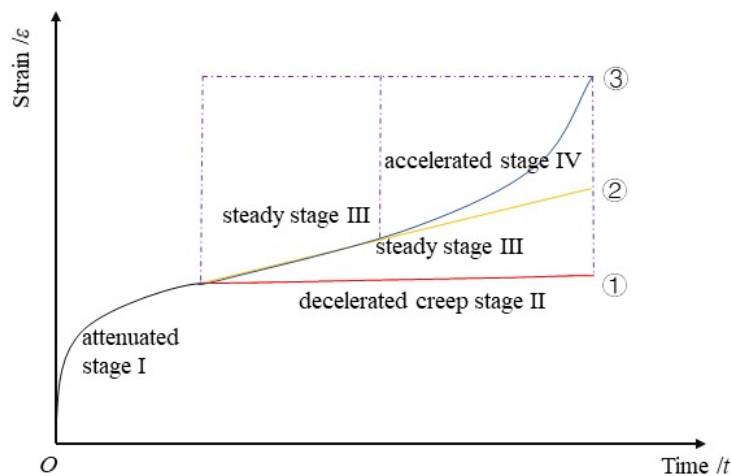


Fig. 6-1 Creep curve modes of standard rock material

According to Fig. 6-1, the creep modes of standard rock has three main types: When the stress value is low, the rock undergoes the creep mode curve ①, which has short-term creep at an attenuated rate and entered decelerated creep stage. When the stress value is larger but less than the peak strength, creep curve ② becomes the creep behaviour law of a standard rock, which entered into a steady stage after the attenuated rate. When the stress is equal or almost the same as peak strength, the standard rock creep curve will be the curve ③ in Fig. 6-1. This creep curve includes three parts: an attenuated stage with attenuated strain rate, a steady stage with constant strain rate and an accelerated stage with accelerated strain rate.

As the broken rock is unconsolidated, it is hard for it to undergo the shear failure as the intact rock under the triaxial compression. Hence, either high-stress or low-stress environments, the transition of the deformation from creep at an attenuated rate to steady-state creep occurred while the creep at an accelerated rate did not (Li et al. 2020). This can also explain why there is no accelerated stage of creep curve in broken rock triaxial experiment results at Fig. 4-10 and Fig. 4-11.

6.2 Fractional order theory

6.2.1 Introduction of fractional order theory

In the 1940s, the mechanics scholars Scott Blair and Geradimov independently proposed the fractional derivative models of Newtonian fluid and Hooke's solid. Geophysicists Caputo and Mainardi applied the fractional calculus method to complex viscoelastic and rheological media and developed several new mechanical models. With the completion of the doctoral dissertation on viscoelastic material modeling of Bagley fractional calculus under the guidance of Torvik, it showed that fractional calculus can be applied to the description of viscoelastic materials and other complex mechanical processes. At the end of the 20th century, due to the research needs of abnormal diffusion, porous media mechanics, non-Newtonian fluid mechanics, viscoelastic mechanics, soft matter physics and mechanics, the research and application

of fractional derivatives have once again attracted widespread attention. Among them, the modeling problems of complex physics, mechanics, biology and engineering are the main force to promote the theory and application of fractional calculus. The order of fractional calculus in these models has certain physical meaning or collective explanation. From an application point of view, the essential difference between the fractional derivative model and the integer order model is:

① Fractional derivative has global relevance, which can better reflect the historical dependence process of the development of system functions; while integer-order derivative has locality and are not suitable for describing the process of historical dependence of functions.

② The fractional derivative model overcomes the shortcomings of the classical integer differential model theory that the experimental results are not in good agreement. Good results can be obtained by using fewer parameters of the fractional derivative model.

③ When describing complex physical and mechanical problems, compared with the nonlinear model, the physical meaning of the fractional model is clearer and the expression is more concise.

6.2.2 Definition of fractional calculus

In the field of fractional calculus, there are mainly three most widely used definition forms: Riemann-Liouville definition, Caputo definition and Grunwald-Letnikov definition. Among them, Riemann-Liouville was mainly used herein.

According to the definition of Riemann-Liouville integrate, for any complex number α , $\text{Re}(\alpha) > 0$, the integral of order α of the function $f(t)$ is defined as:

$$\left({}_t D_t^{-\alpha} f\right)(t) = \frac{1}{\Gamma(\alpha)} \int_{t_0}^t \frac{f(\tau)}{(t-\tau)^{1-\alpha}} d\tau \quad (6-2)$$

where $\Gamma()$ is Gamma function, which can be described as:

$$\Gamma(z) = \int_0^{\infty} e^{-x} x^{z-1} dx, \quad \text{Re}(z) > 0 \quad (6-3)$$

As for the definition of the Riemannian-Liouville derivative, for any complex number α , $\text{Re}(\alpha) > 0$, it can be defined as:

$${}^{RL}D_t^\alpha f(t) = \frac{d^n}{dt^n} [{}_{t_0}D_t^{-(n-\alpha)} f(t)] \quad (n = |\alpha| + 1, n-1 < \alpha \leq n) \quad (6-4)$$

When α is an integer, Eq. (6-4) changes into integer derivative.

According to fractional order theory, the Riemann-Liouville fractional derivative has the following main characteristics:

Characteristic 1:

$${}^{RL}D_t^\lambda [Cf(t)] = C {}^{RL}D_t^\lambda [f(t)] \quad (\lambda \in R) \quad (6-5)$$

where C is arbitrary constant.

Particularly, the Riemann-Liouville fractional derivative of the constant C is not 0 but as follows:

$${}^{RL}D_t^\alpha C = \frac{Ct^{-\alpha}}{\Gamma(1-\alpha)} \quad (6-6)$$

Characteristic 2:

$${}^{RL}D_t^\lambda [f_1(t) + f_2(t)] = {}^{RL}D_t^\lambda [f_1(t)] + {}^{RL}D_t^\lambda [f_2(t)] \quad (\lambda \in R) \quad (6-7)$$

Characteristic 3:

$${}^{RL}D_t^{-\lambda} {}^{RL}D_t^{-\alpha} [f(t)] = {}^{RL}D_t^{-\lambda-\alpha} [f(t)] \quad (\lambda, \alpha > 0) \quad (6-8)$$

Characteristic 4:

$${}^{RL}D_t^\lambda {}^{RL}D_t^{-\alpha} [f(t)] = {}^{RL}D_t^{\lambda-\alpha} [f(t)] \quad (\lambda, \alpha > 0) \quad (6-9)$$

Characteristic 5:

$${}^{RL}D_t^\lambda [(t-t_0)^\gamma] = \frac{\Gamma(1+\gamma)}{\Gamma(1+\gamma-\lambda)} (t-t_0)^{\gamma-\lambda} \quad (6-10)$$

It is noted that the solution of the fractional calculus function $\frac{d^p}{dt^p} f(t) = 0$, ($0 < p < 1$) is $f(t) = Ct^{p-1}$, indicating that the dynamic steady-state systems of fractional order are not static. If $f(t)$ is regarded as the dimensionality, the stability of the fractional dimensionality of the dynamic system expresses that the phase space volume $f(t)$ decreases with time. Therefore, the fractional dynamic system is a dissipative system.

6.2.3 Fractional basic mechanical elements -- Abel dashpot

When establishing the fractional order creep model, the same as the integer order model, the corresponding model is established through the combination of mechanical components. Fractional mechanical components include three categories: elastic components, viscous components, and plastic components. Among them, the elastic element and the plastic one are the same as the integer order mechanical element. The viscous element of the integer order model is called the dashpot, while in the fractional order model, the viscous element becomes the Abel dashpot, as shown in Fig. 6-2.

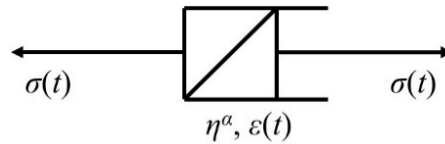


Fig. 6-2 Schematic diagram of Abel dashpot

Abel dashpot is a mechanical element derived based on integer order dashpot. Its constitutive equation is:

$$\sigma(t) = \eta^\alpha \frac{d^\alpha \varepsilon(t)}{dt^\alpha} \quad (0 \leq \alpha \leq 1, \alpha \in R^+, t > 0) \quad (6-11)$$

where η is the viscosity coefficient of the Abel dashpot; α is the order of the Abel dashpot.

When $\alpha = 1$, Eq. (6-11) changes into $\sigma(t) = \eta \frac{d\varepsilon(t)}{dt}$, that is, Abel dashpot changes into integer order dashpot. At this time, the viscous fluid characteristics of rock is performed. When $\alpha = 0$, the constitutive equation is $\sigma(t) = E\varepsilon$, Abel dashpot becomes

spring, and the elastic solid characteristic will be performed. When the orders α is between 0 and 1, the Abel dashpot model can describe a viscoelastic body whose deformation is between elastic and viscous.

The creep equation of Abel dashpot can be described as:

$$\varepsilon(t) = \frac{\sigma_0}{\eta^\alpha} \frac{t^\alpha}{\Gamma(\alpha+1)} \quad (0 \leq \alpha \leq 1, \alpha \in R^+, t > 0) \quad (6-12)$$

According to Eq. (6-12), fix other parameters, the creep curves under different fractional order β were obtained, as shown in Fig. 6-3 (Cao 2017).

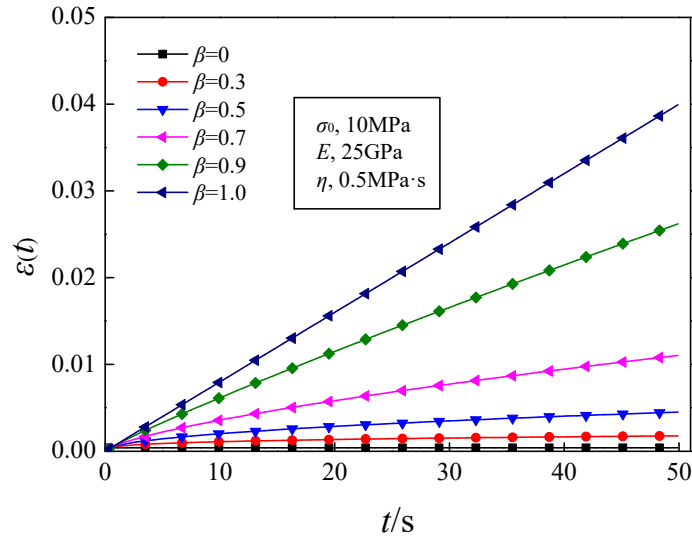


Fig. 6-3 Creep characteristic curves of Abel dashpot in different β -th-order (Cao 2017)

According to Fig. 6-3, when $\beta \neq 1$ and 0, the creep curve did not linear increase like Newton fluid ($\beta = 1$) and did not stay as constant like elastic body ($\beta = 0$). The creep curve showed a non-linear gradual process, which could reflect the viscoelastic properties of rock materials.

6.3 Creep model of broken rock based on fractional order theory

6.3.1 Construction of broken rock creep model

According to the analysis in Subsection 6.1, the creep curve of broken rock did not exhibit creep at an accelerated rate even the loading time is significant. Therefore,

in order to discuss the creep behavior of broken rock quantitatively, the excited three creep mechanical elements were connected in series, which include the Hooke body describing transient creep, the Kelvin model representing decelerated creep and the Bingham model used to describe steady creep.

The viscous element of the fractional-order model is known as an Abel dashpot (Peng et al. 2017; Wu et al. 2015), which better describes gradual nonlinear changes in the curve of creep of the broken rock in overburden caving zone (Li et al. 2020). Hence, the dashpot in the integer Kelvin model and the integer Bingham model was replaced by an Abel dashpot. Fig. 6-4 shows the final construction of broken rock creep model schematic diagram.

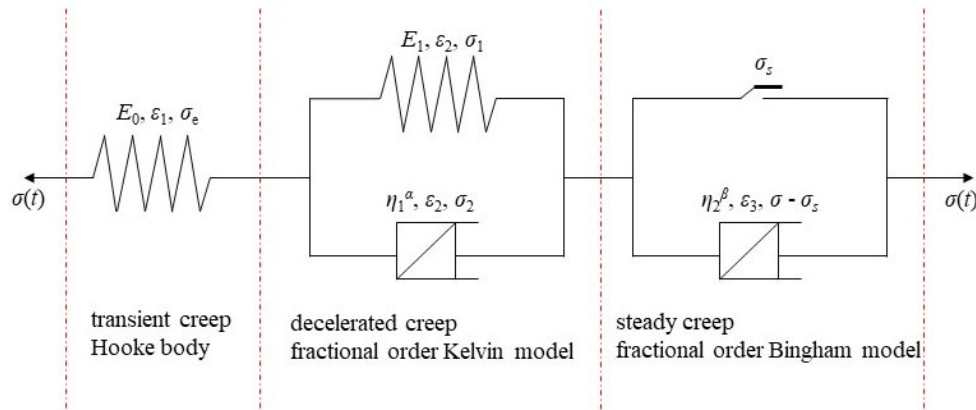


Fig. 6-4 Schematic diagram of the broken rock creep model

As shown in Fig. 6-4, E_0 and E_1 are the elastic modulus of the spring in Hooke body and fractional order Kelvin model, respectively; $\varepsilon_1, \varepsilon_2$ and ε_3 are the strain of the spring in Hooke body, fractional order Kelvin model and fractional order Bingham model, respectively; σ_e and σ_1 is the stress of the spring in Hooke body and fractional order Kelvin model, respectively; σ_2 is the stress of the Abel dashpot in fractional order Kelvin model; σ_s is a critical stress when the creep curve changed from curve ① to curve ② in Fig. 6-1. The main parameters of Abel dashpot models in fractional order Kelvin model and fractional order Bingham model are viscosity coefficient η_1^α and η_2^β , and the order α and β , respectively.

According to the combination of the basic elements in Fig. 6-4, the state equation

of the broken rock model is:

When $0 \leq \sigma \leq \sigma_s$, the Bingham model in Fig. 6-4 does not work and the transient creep stage and the decelerated creep stage occurred. The creep model of broken rock in that case can be described as:

$$\left\{ \begin{array}{l} \sigma_e = E_0 \varepsilon_1(t) \\ \sigma_{ev} = E_1 \varepsilon_2(t) + \eta_1^\alpha \frac{d^\alpha \varepsilon_2(t)}{dt^\alpha} \\ \varepsilon = \varepsilon_1 + \varepsilon_2 \\ \sigma = \sigma_e = \sigma_{ev} \end{array} \right. \quad (6-13)$$

where σ_{ev} is the stress undergone by the fractional order Kelvin model in Fig. 6-4.

Solve Eq. (6-13), and let $\sigma = \sigma_0$ (σ_0 is the stress the calculated material undergone), the creep equation when $0 \leq \sigma \leq \sigma_s$ is obtained as follow:

$$\varepsilon(t) = \frac{\sigma_0}{E_0} + \frac{\sigma_0}{\eta_1^\alpha} t^\alpha E_{\alpha, \alpha+1} \left(-\frac{E_1}{\eta_1^\alpha} t^\alpha \right) \quad (6-14)$$

where $E_{\alpha, \alpha+1} \left(-\frac{E_1}{\eta_1^\alpha} t^\alpha \right)$ is Mittag-Leffler function, which was defined as:

$$E_{a,b}(z) = \sum_{k=0}^{\infty} \frac{z^k}{\Gamma(ak+b)} \quad (6-15)$$

where α is strictly positive.

When $\sigma > \sigma_s$, the Bingham model in Fig. 6-4 works and the transient creep stage and the steady creep stage occurred. The creep model of the broken rock in that case can be described as:

$$\left\{ \begin{array}{l} \sigma_e = E_0 \varepsilon_1(t) \\ \sigma_{ev} = E_1 \varepsilon_2(t) + \eta_1^\alpha \frac{d^\alpha \varepsilon_2(t)}{dt^\alpha} \\ \sigma_{ev} - \sigma_s = \eta_2^\beta \frac{d^\beta \varepsilon_3(t)}{dt^\beta} \\ \varepsilon = \varepsilon_1 + \varepsilon_2 + \varepsilon_3 \\ \sigma = \sigma_e = \sigma_{ev} = \sigma_v \end{array} \right. \quad (6-16)$$

where σ_v is the stress undergone by the fractional order Bingham model in Fig. 6-4.

Solve Eq. (6-16), and let $\sigma = \sigma_0$, the creep equation when $\sigma > \sigma_s$ is obtained as:

$$\varepsilon(t) = \frac{\sigma_0}{E_0} + \frac{\sigma_0}{\eta_1^\alpha} t^\alpha E_{\alpha, \alpha+1} \left(-\frac{E_1}{\eta_1^\alpha} t^\alpha \right) + \frac{\sigma_0 - \sigma_s}{\eta_2^\beta} \frac{t^\beta}{\Gamma(1+\beta)} \quad (6-17)$$

6.3.2 Calculation of broken rock creep model

Moreover, there is a switch in the fractional order Bingham model in Fig. 6-4. When $\sigma < \sigma_s$, Hooke body and Kelvin model deform together, and the creep curve corresponds to curve ① in Fig. 6-1. When $\sigma > \sigma_s$, Bingham model participates in the broken rock creep deformation, resulting in the creep curve of broken rock in line with curve ② in Fig. 6-1. σ_s represents the threshold stress value from decelerated creep stage to steady creep stage, which is the long-term strength of the broken rock. σ_s can be obtained from a large amount of indoor experiments. In this research, it is assumed that σ_s is the lower level of loading stress at which steady creep stage occurs. According to the experiment results, σ_s in this study is the secondary load stress 4 MPa.

According to the definition of Mittag-Leffler function, the following equation can be written as:

$$\begin{aligned} E_{\alpha,1} \left(-\frac{E_1}{\eta_1^\alpha} t^\alpha \right) &= \sum_{k=0}^{\infty} \frac{\left(-\frac{E_1}{\eta_1^\alpha} t^\alpha \right)^k}{\Gamma(\alpha k + 1)} \\ &= \frac{1}{\Gamma(1)} + \frac{-\frac{E_1}{\eta_1^\alpha} t^\alpha}{\Gamma(\alpha + 1)} + \frac{\left(-\frac{E_1}{\eta_1^\alpha} t^\alpha \right)^2}{\Gamma(2\alpha + 1)} + \dots + \frac{\left(-\frac{E_1}{\eta_1^\alpha} t^\alpha \right)^{k+1}}{\Gamma(\alpha k + \alpha + 1)} + \dots \\ &= 1 - \frac{E_1}{\eta_1^\alpha} t^\alpha \left(\frac{1}{\Gamma(\alpha + 1)} + \frac{-\frac{E_1}{\eta_1^\alpha} t^\alpha}{\Gamma(2\alpha + 1)} + \dots + \frac{\left(-\frac{E_1}{\eta_1^\alpha} t^\alpha \right)^k}{\Gamma(\alpha k + \alpha + 1)} + \dots \right) \\ &= 1 - \frac{E_1}{\eta_1^\alpha} t^\alpha E_{\alpha, \alpha+1} \left(-\frac{E_1}{\eta_1^\alpha} t^\alpha \right) \end{aligned} \quad (6-18)$$

Then, substituting Eq. (6-18) into Eq. (6-14) and Eq. (6-17), they can be rewritten

respectively as:

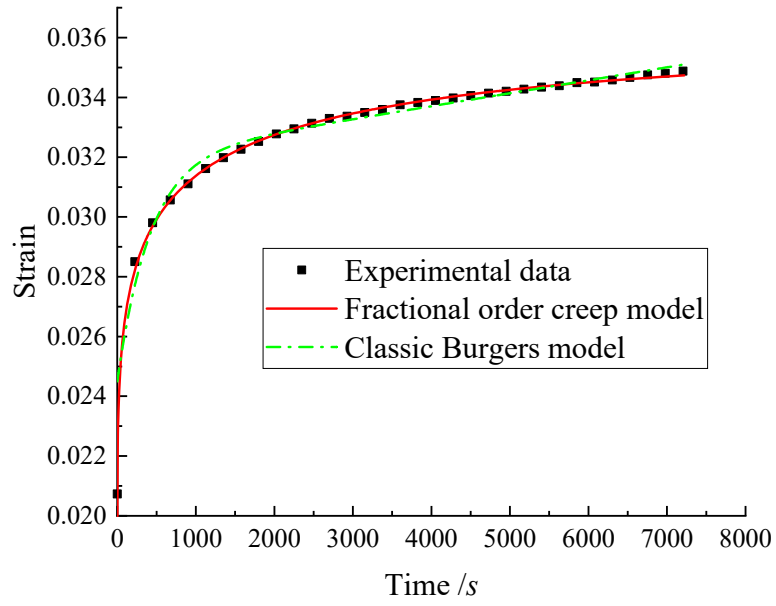
$$\begin{cases} \varepsilon(t) = \frac{\sigma_0}{E_0} + \frac{\sigma_0}{E_1} \left[1 - E_{\alpha,1} \left(-\frac{E_1}{\eta_1^\alpha} t^\alpha \right) \right] & 0 \leq \sigma \leq \sigma_s \\ \varepsilon(t) = \frac{\sigma_0}{E_0} + \frac{\sigma_0 - \sigma_s}{\eta_2^\beta} \frac{t^\beta}{\Gamma(1+\beta)} + \frac{\sigma_0}{E_1} \left[1 - E_{\alpha,1} \left(-\frac{E_1}{\eta_1^\alpha} t^\alpha \right) \right] & \sigma > \sigma_s \end{cases} \quad (6-19)$$

Because creep problem is related to time, if the exponential coefficient of creep compliance was maintained, the Gamma function in Mittag-Leffler function can be simplified (Li M et al. 2020). Hence, assume that α in Mittag-Leffler function is equal to 1, then according to the method of power series expansion, Eq. (6-19) can be recomputed as:

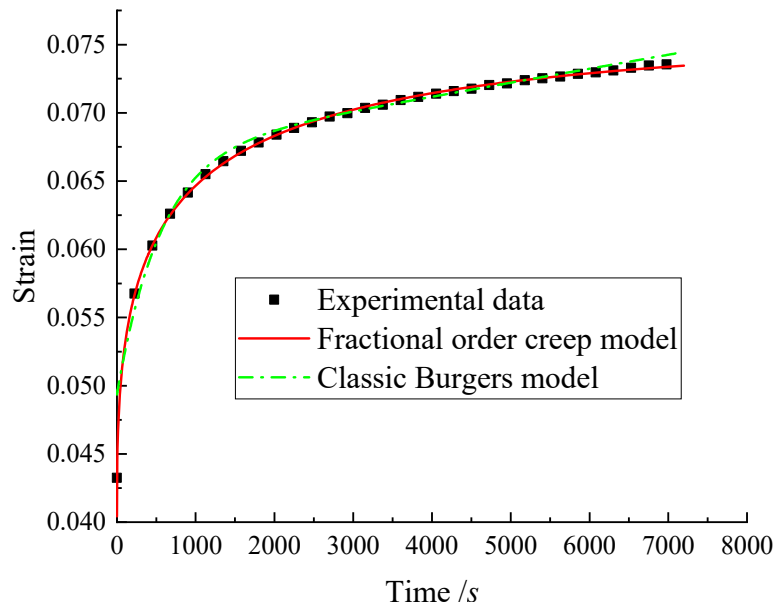
$$\begin{cases} \varepsilon(t) = \frac{\sigma_0}{E_0} + \frac{\sigma_0}{E_1} \left[1 - \exp\left(-\frac{E_1}{\eta_1^\alpha} t^\alpha\right) \right] & 0 \leq \sigma \leq \sigma_s \\ \varepsilon(t) = \frac{\sigma_0}{E_0} + \frac{\sigma_0 - \sigma_s}{\eta_2^\beta} \frac{t^\beta}{\Gamma(1+\beta)} + \frac{\sigma_0}{E_1} \left[1 - \exp\left(-\frac{E_1}{\eta_1^\alpha} t^\alpha\right) \right] & \sigma > \sigma_s \end{cases} \quad (6-20)$$

6.4 Reliability of proposed broken rock creep model

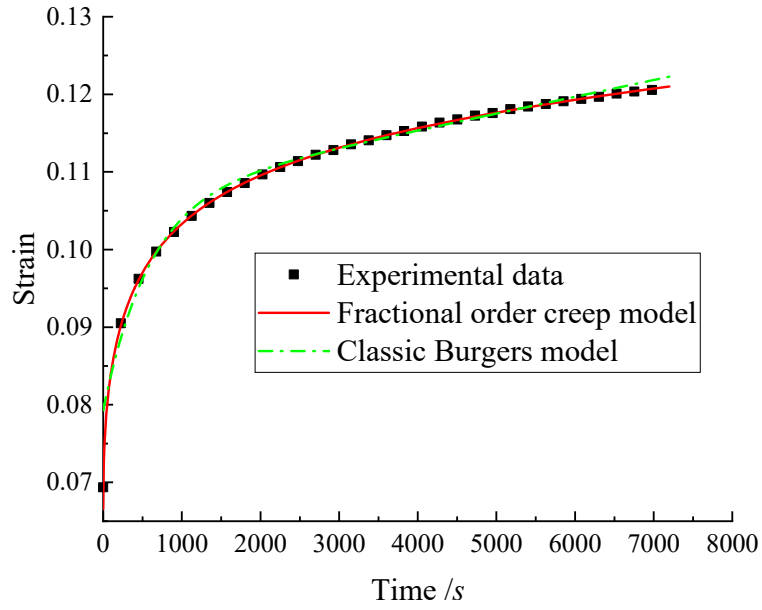
To obtain the parameters of creep equation, the least squares method was adopted to carry out the non-linear fitting of creep data. Meanwhile, the parameters of classical Burgers creep model which was widely used to describe creep behavior was also identified by the least square method. The results of these creep parameters with the different size grading are shown in Figs. 6-5, 6-6, 6-7, 6-8, and 6-9. The experiment data in these figures is obtained from the experiment study in Chapter 4. The fitting parameters is shown in Table S1 in supplement.



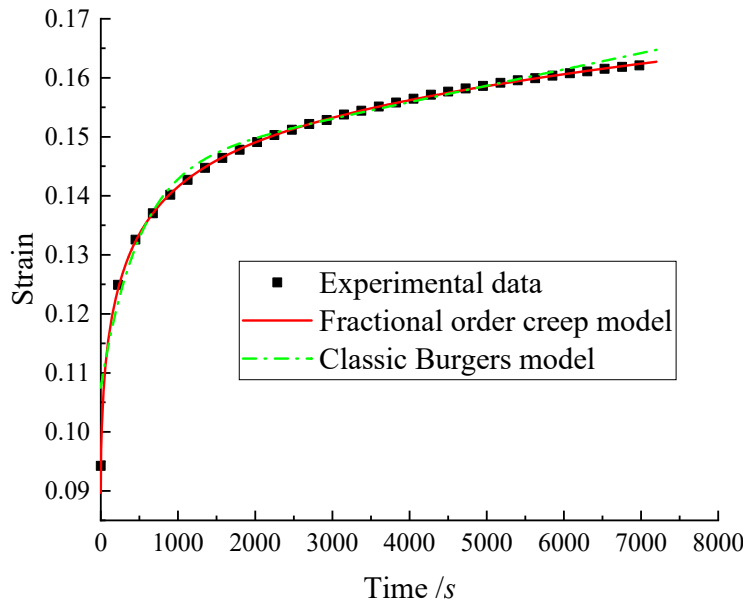
(a) Axial pressure 2 MPa



(b) Axial pressure 4 MPa

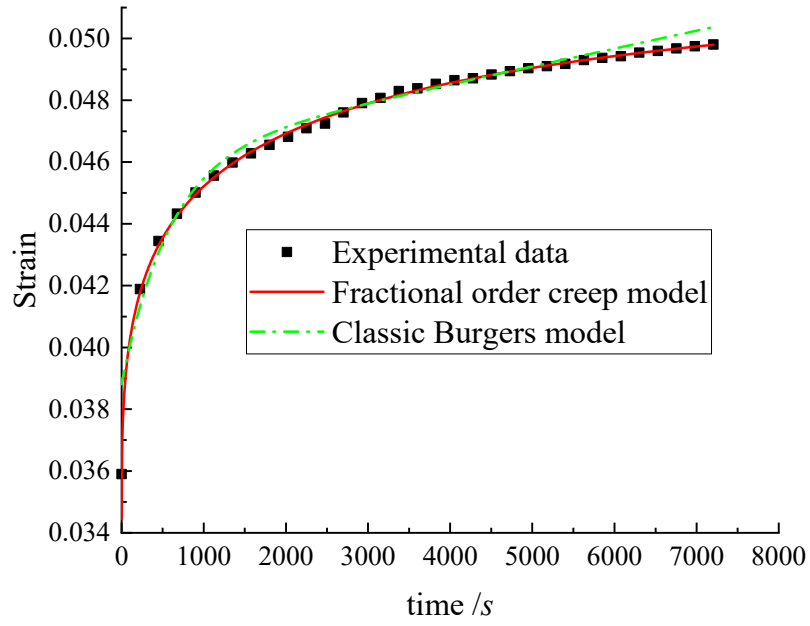


(c) Axial pressure 6 MPa

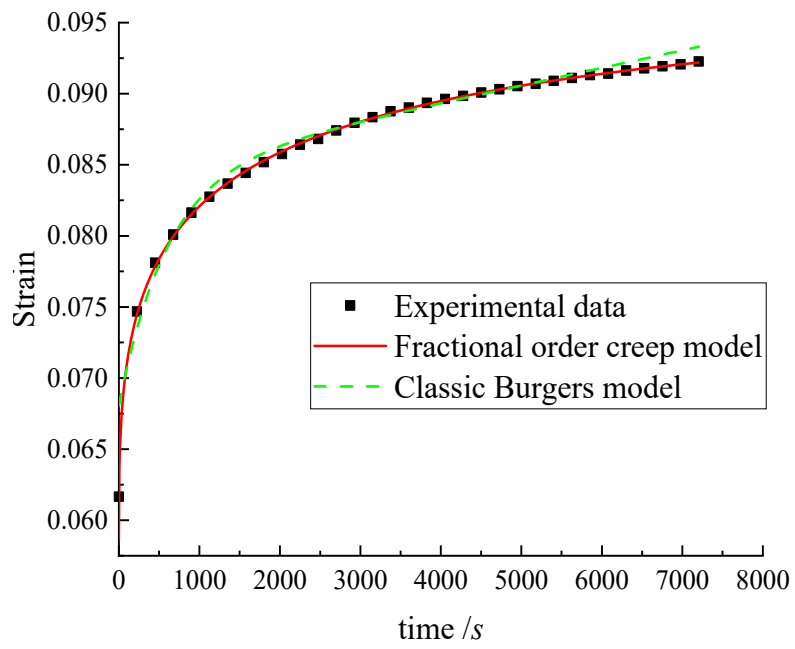


(d) Axial pressure 8 MPa

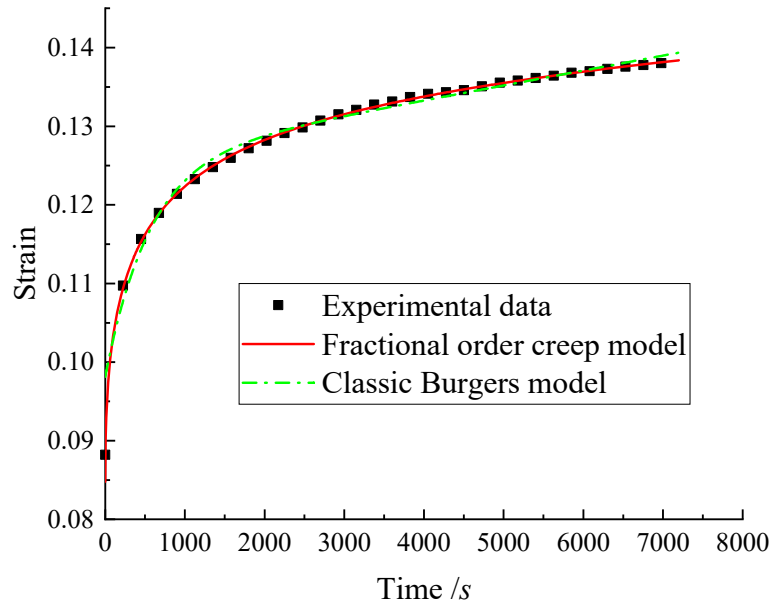
Fig. 6-5 Creep compression test data and fitted results at the size grading of G5



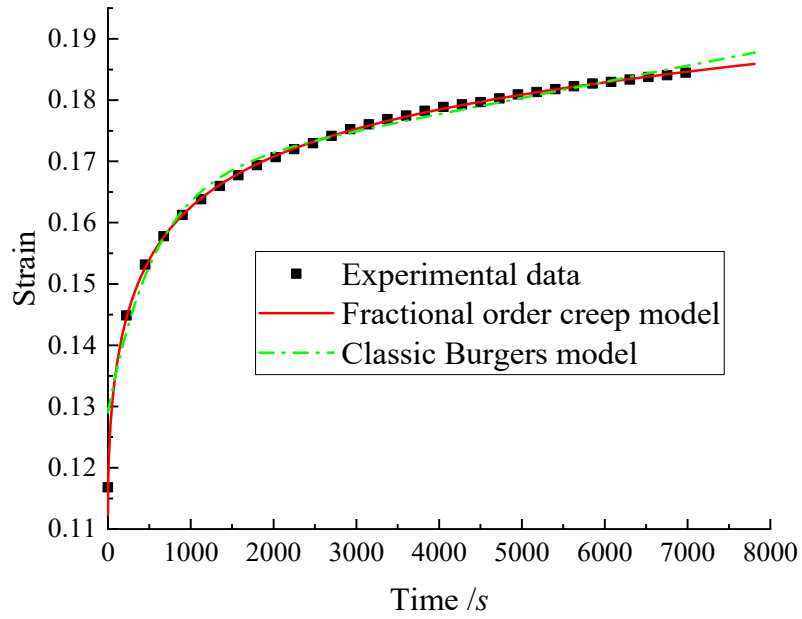
(a) Axial pressure 2 MPa



(b) Axial pressure 4 MPa

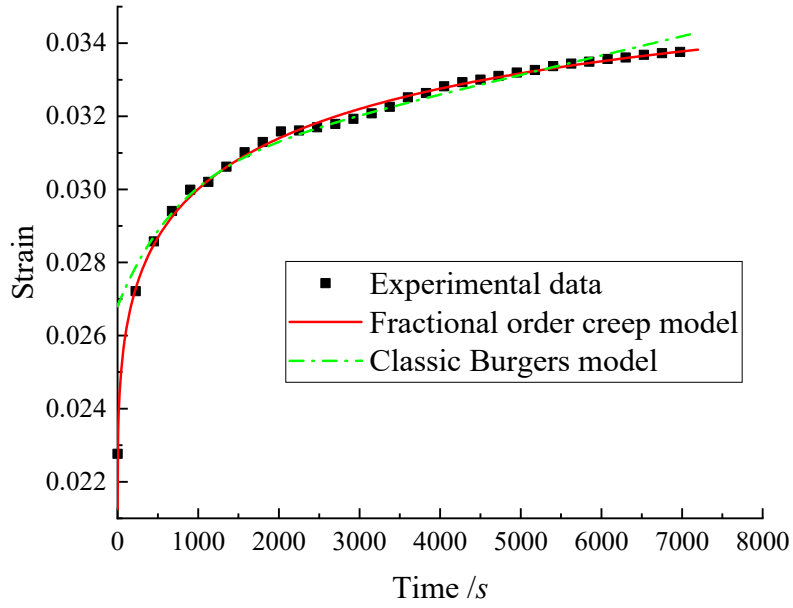


(c) Axial pressure 6 MPa

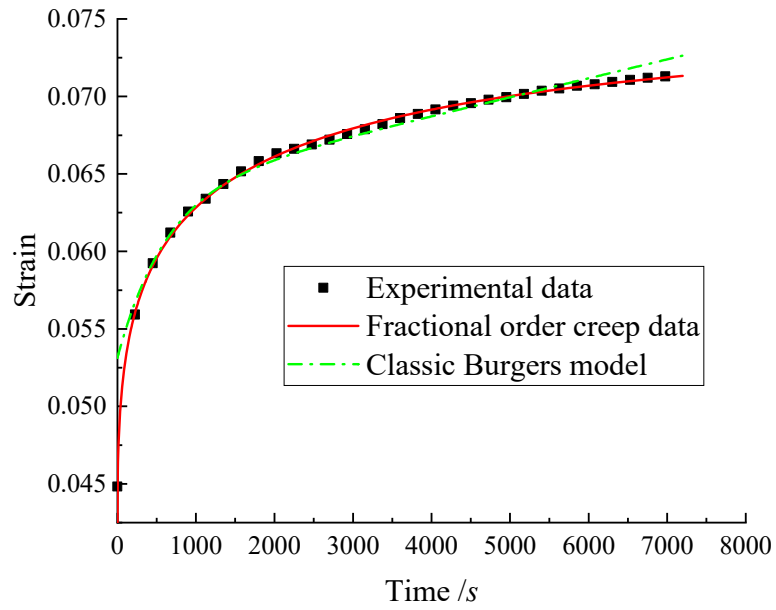


(d) Axial pressure 8 MPa

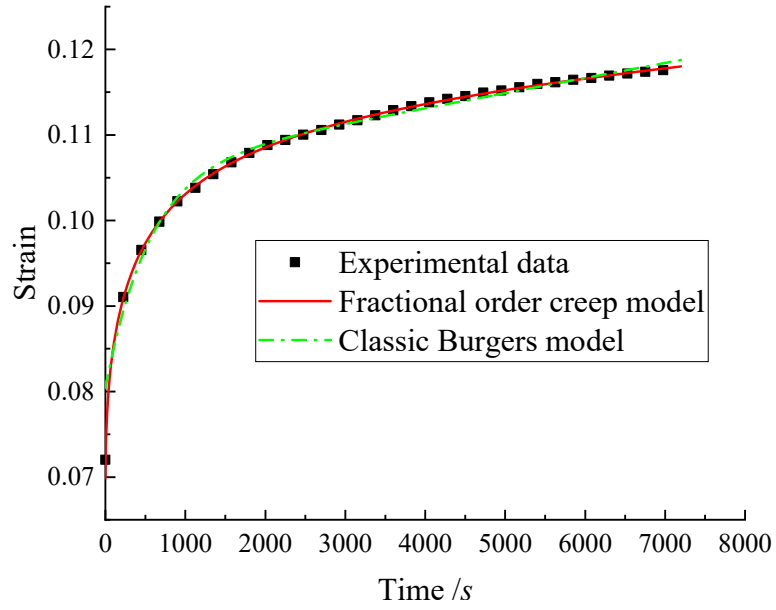
Fig. 6-6 Creep compression test data and fitted results at the size grading of G4



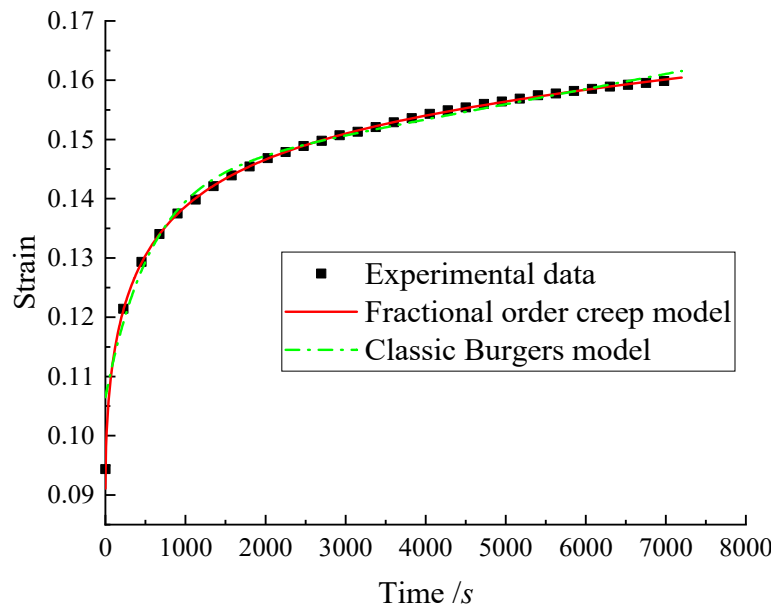
(a) Axial pressure 2 MPa



(b) Axial pressure 4 MPa

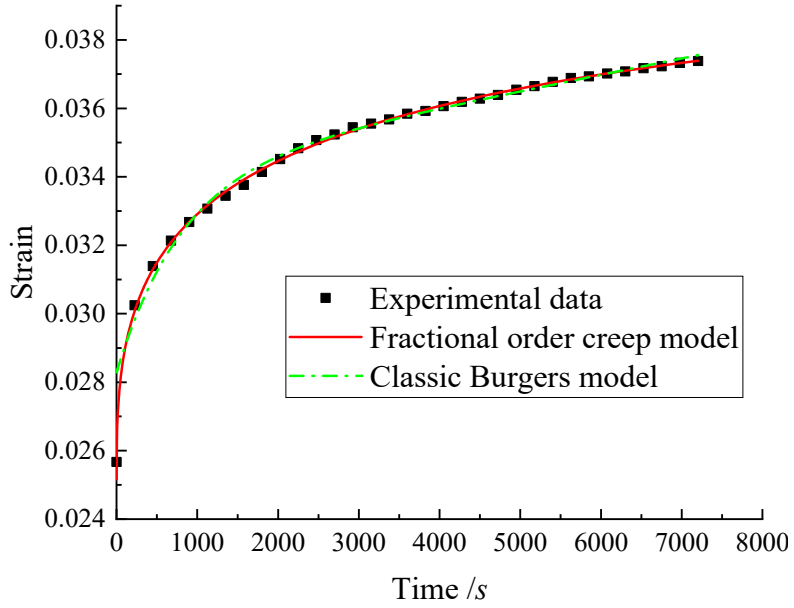


(c) Axial pressure 6 MPa

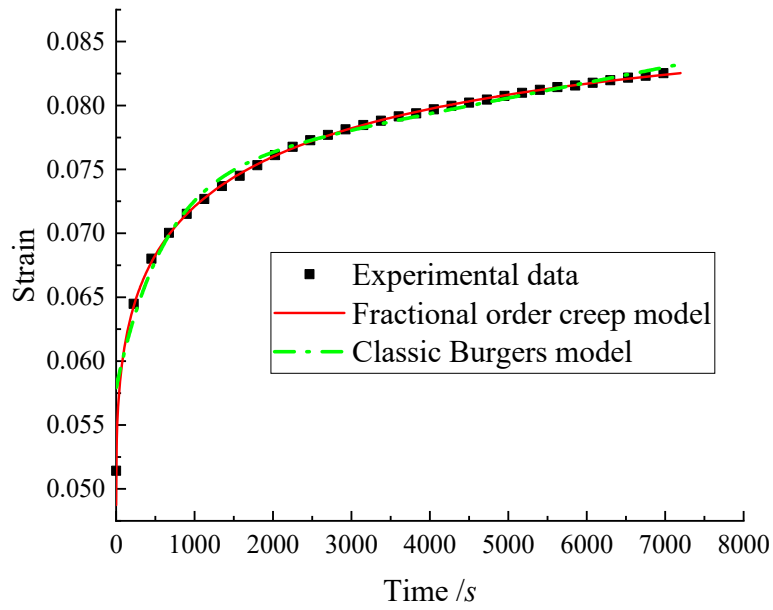


(d) Axial pressure 8 MPa

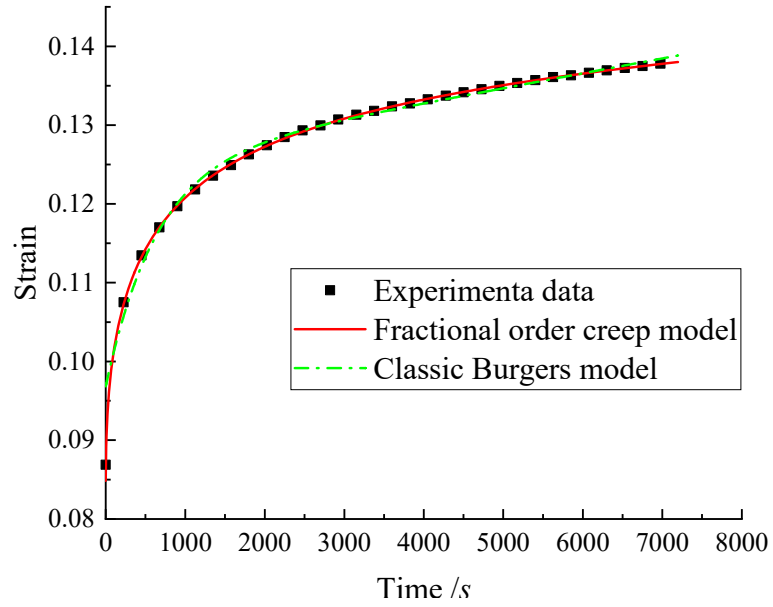
Fig. 6-7 Creep compression test data and fitted results at the size grading of G3



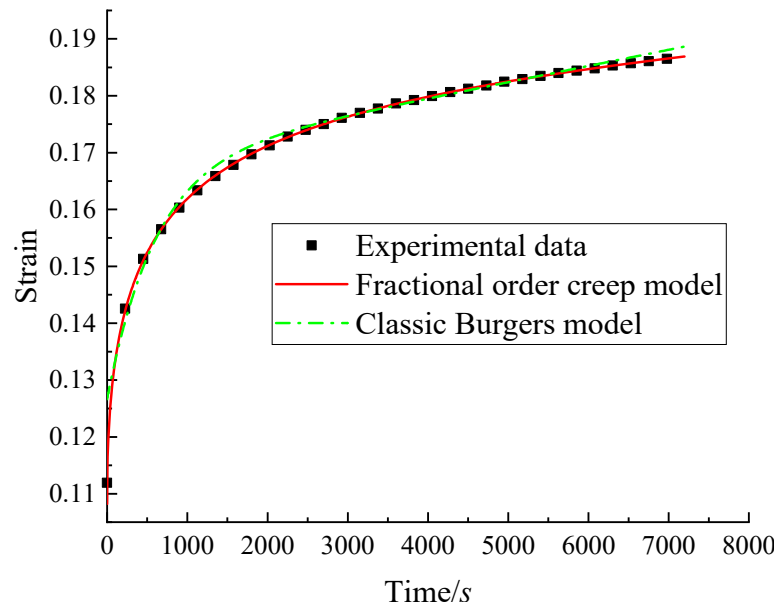
(a) Axial pressure 2 MPa



(b) Axial pressure 4 MPa

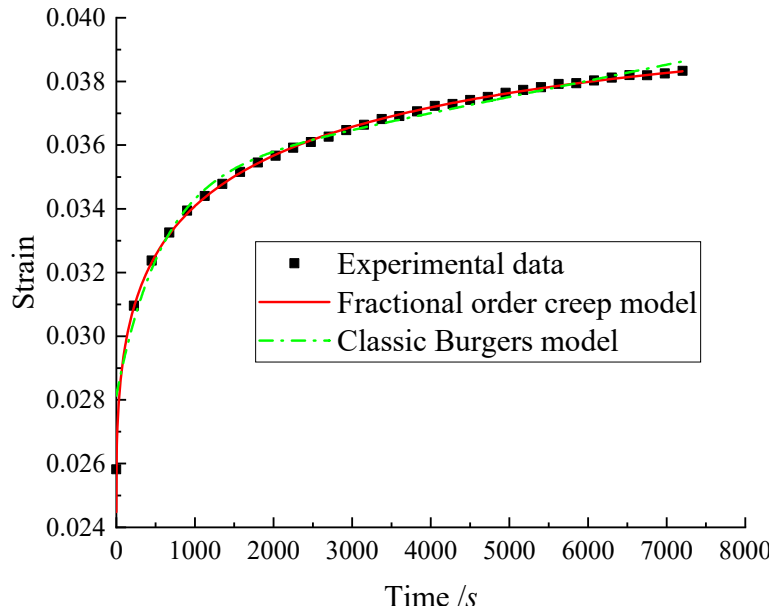


(c) Axial pressure 6 MPa

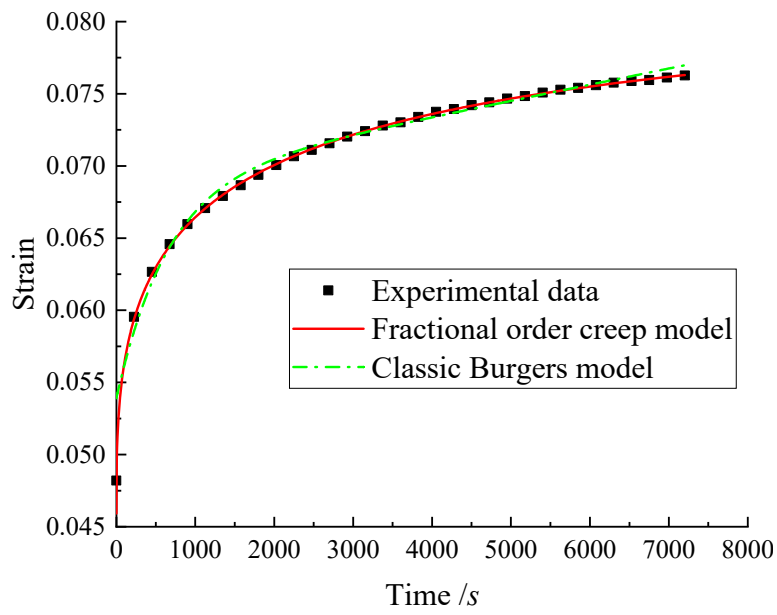


(d) Axial pressure 8 MPa

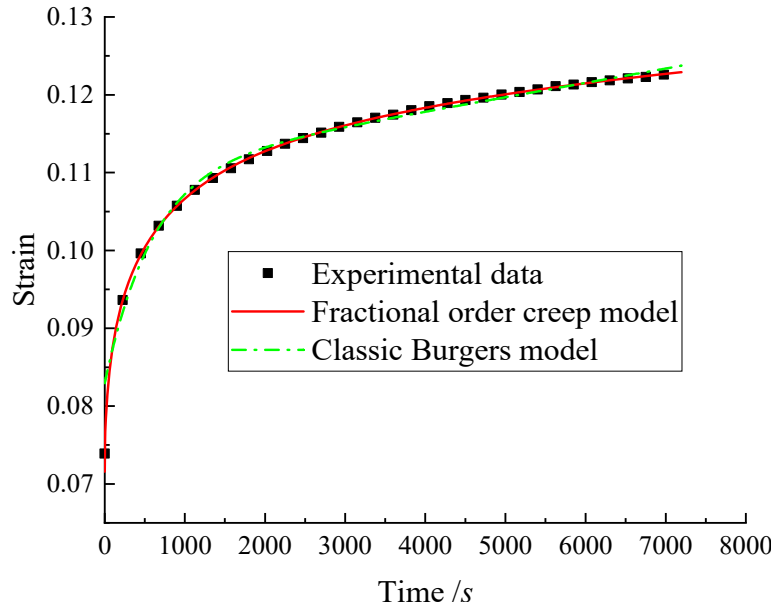
Fig. 6-8 Creep compression test data and fitted results at the size grading of G2



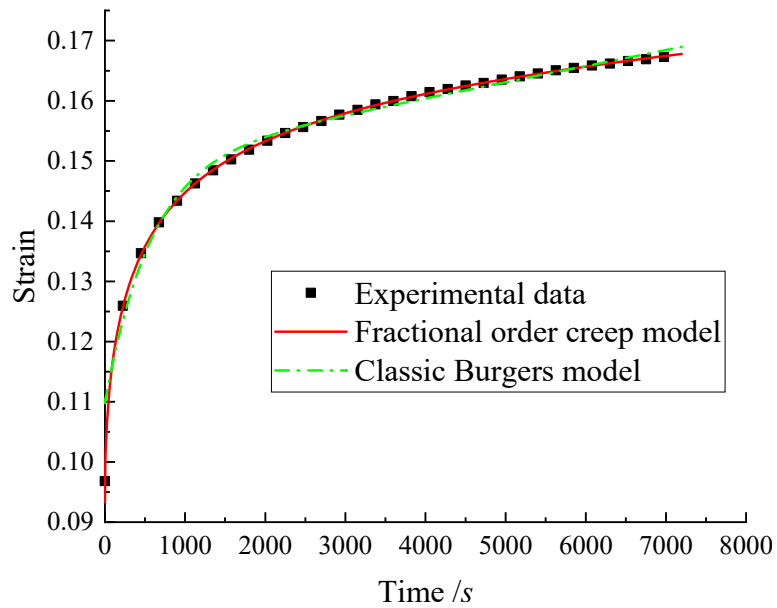
(a) Axial pressure 2 MPa



(b) Axial pressure 4 MPa



(c) Axial pressure 6 MPa



(d) Axial pressure 8 MPa

Fig. 6-9 Creep compression test data and fitted results at the size grading of G1

An analysis of Figs. 6-5, 6-6, 6-7, 6-8 and 6-9 show that the classical Burgers creep model and the creep model of Eq. (6-20) can both reveal trends in the creep behavior of broken rock in the goaf. However, comparing with the Classic Burgers creep model, the trend of the fractional order creep model Eq. (6-20) show better agreement with the

experimental data, especially at the early stage of the curve. Therefore, it was proved that the creep model in Fig. 6-4 could describe the creep behavior of broken rock in mining goaf accurately. Meanwhile, the fitting determination coefficients of Eq. (6-20) and classic Burgers creep model also could prove this viewpoint, as shown in Fig. 6-10.

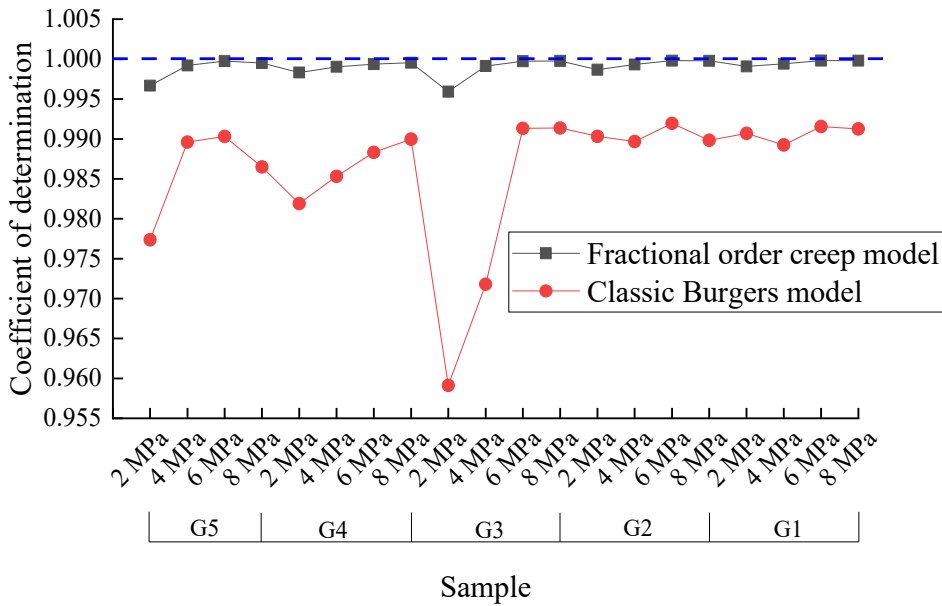


Fig. 6-10 Determination coefficient of fractional order creep model and classic Burgers model

According to Fig. 6-10, the coefficient of determination of the Burgers creep model is larger than 0.955, almost reaches 1. The bulking coefficient prediction model is deduced based on the Burgers creep model. Hence, it can be said that the accuracy of the bulking coefficient equation in Chapter 5 is enough for prediction. However, the fractional order creep model coefficient of determination is higher than the Burgers creep model. It is indicated that the broken rock properties are between the linear increase like Newton fluid and constant like elastic body.

6.5 Application of the fractional order creep model

The deformation characteristics of the broken rock under triaxial compression was studied above, and Eq. (6-20) was proposed to describe the creep behavior of broken rock. To study the applicability of the creep theory of broken rock, large-scale study

needs be carried out.

6.5.1 Caving zone subsidence considering time based on fractional order model

The deformation of caving zone can be calculated by the strain integral of caving zone. According to Eq. (6-20), the deformation of caving zone is:

$$\begin{cases} W(t) = \int \sigma_0(h) dh \left\{ \frac{1}{E_0} + \frac{1}{E_1} \left[1 - \exp\left(-\frac{E_1}{\eta_1^\alpha} t^\alpha\right) \right] \right\} & 0 \leq \sigma \leq \sigma_s \\ W(t) = \int \sigma_0(h) dh \left\{ \frac{1}{E_0} + \frac{1}{\eta_2^\beta} \frac{t^\beta}{\Gamma(1+\beta)} + \frac{1}{E_1} \left[1 - \exp\left(-\frac{E_1}{\eta_1^\alpha} t^\alpha\right) \right] \right\} - \frac{\sigma_s}{\eta_2^\beta} \frac{t^\beta}{\Gamma(1+\beta)} H_c & \sigma > \sigma_s \end{cases} \quad (6-21)$$

where H_c is the total height of caving zone; h is the height of the caving zone from the floor. If use F to represent the constant $\int \sigma_0(h) dh$, then Eq. (6-21) can be rewritten as:

$$\begin{cases} W(t) = \frac{F}{E_0} + \frac{F}{E_1} \left[1 - \exp\left(-\frac{E_1}{\eta_1^\alpha} t^\alpha\right) \right] & 0 \leq \sigma \leq \sigma_s \\ W(t) = \frac{F}{E_0} + \left(\frac{F}{\eta_2^\beta} - \frac{\sigma_s}{\eta_2^\beta} H_c \right) \frac{t^\beta}{\Gamma(1+\beta)} + \frac{F}{E_1} \left[1 - \exp\left(-\frac{E_1}{\eta_1^\alpha} t^\alpha\right) \right] & \sigma > \sigma_s \end{cases} \quad (6-22)$$

Eq. (6-22) describes the relationship between the subsidence value and time. If we know the initial period of caving zone subsidence, the future subsidence value can be predicted by Eq. (6-22).

6.5.2 Proof of caving zone subsidence prediction equation

(1) Proved by simulation experiment

Li carried out a similar simulation experiment of underground overburden (Li 2017). The sample was made the same layer as the filed case with certain similarity scaling parameters, shown in Fig. 6-11. The geometrical scale and the time scale were 150 and 12.25, respectively. Then, the stress scale could be calculated as 250 (Li 2017).

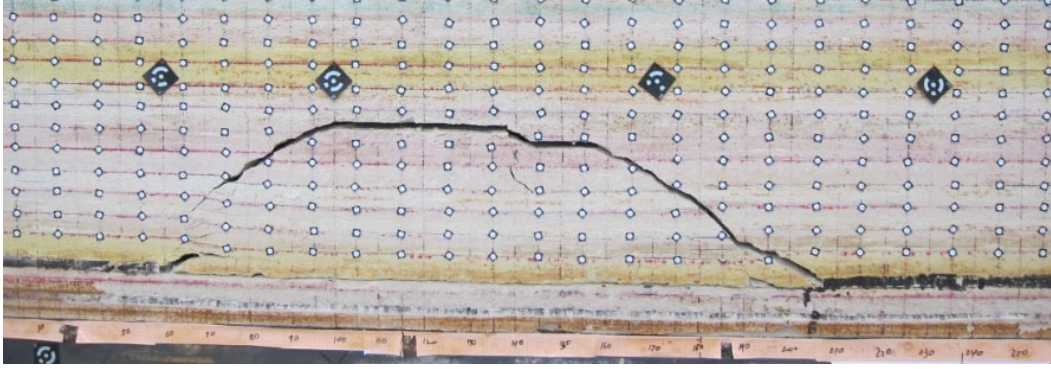


Fig. 6-11 Deformations of overburden after mining at 220m of simulation experiment (Li 2017)

To prove the accuracy of the subsidence prediction equation, the caving zone deformation results of this test study was fitted by the subsidence prediction equation, Eq. (6-22). The fitting results are shown in Fig. 6-12. The fitting function parameters in Fig. 6-12 are shown in Table 6-1.

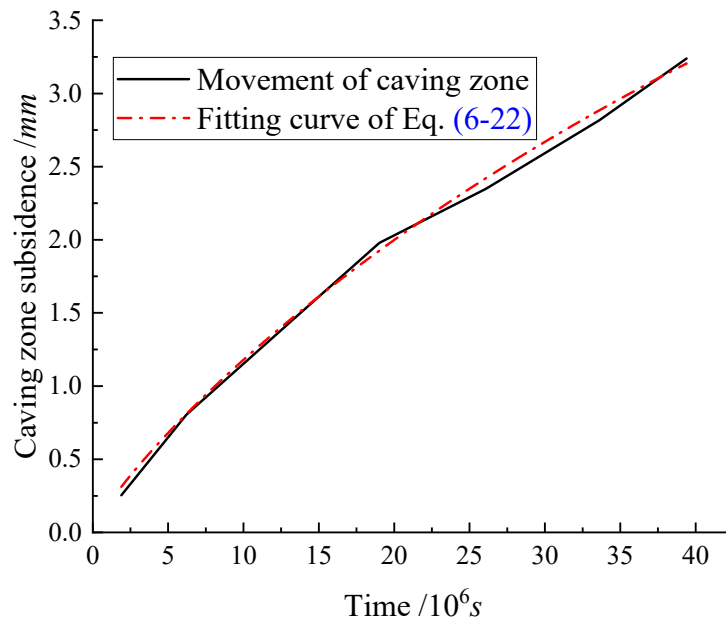


Fig. 6-12 Comparison of the subsidence between prediction equation and experiment results

As shown in Fig. 6-12, the curve of the prediction equation fitted well with the caving zone subsidence results of the similar simulation experiment. The determination coefficient of this fitting function is 0.997.

Table 6-1 Fitting parameters of the subsidence prediction equation with simulation experiment results

Parameters	Values
E_0	983.82 MPa
E_1	2.13 MPa
η_1	1.99×10^8
α	0.86
F	16.57 MPa

(2) Proved by on-site results of Zhangzhuang mine

Each zone's subsidence results of Zhang Huaizhu working face in Zhuangzhuang mine was calculated in Chapter 3 by the proposed calculated method. To farther prove the reliability of the prediction equation of the caving zone subsidence, the results of Zhang Huaizhu working face was fitted by the prediction equation, as shown in Fig. 6-13. The fitting parameters are shown in Table 6-2.

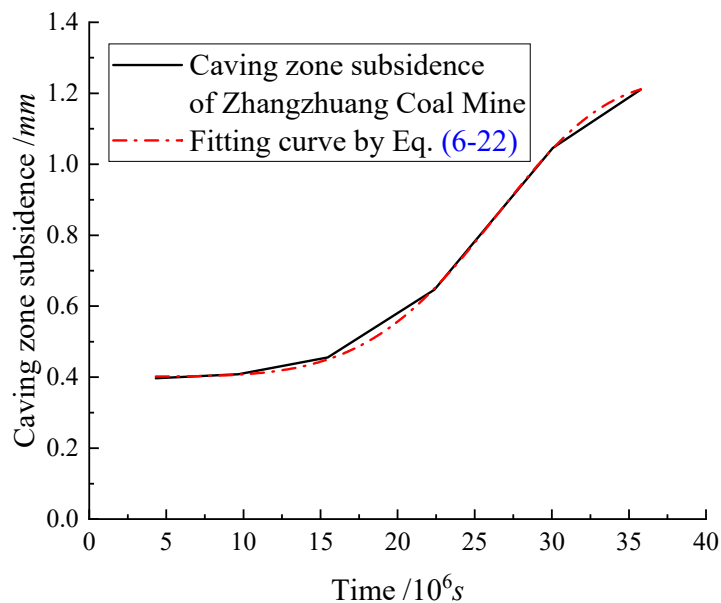


Fig. 6-13 Comparison of the subsidence between prediction equation and on-site results

According to Fig. 6-13, the field data in Chapter 3 can fit the prediction equation well with the determination coefficient 0.999. Hence, it can say that the data from Zhang Zhuang mine proved the reliability of the caving zone subsidence prediction equation.

Table 6-2 Fitting parameters of the subsidence prediction equation of on-site calculated results

Parameters	Values
E_0	11.35
E_1	5.44
η_1	3.955×10^7
α	4.815
F	4.56

However, the caving zone deformation data from Zhangzhuang mine was only 6 points and the monitoring scale was huge, which made a large tendency to cause big errors. Hence, it is not enough to fitting the deformation equation Eq. (6-22) by only these data. More results from other kinds of mine site, such as inclined coal seam, deep buried, shallow buried and so on, need be compared in the future study. At that case, further research of the accuracy and the application will be studied.

6.6 Summary

(1) A creep model base on fractional calculus of broken rock was proposed and the reliability of it was proved by the triaxial compression experiment results. Fractional order creep model can fit the indoor experiment results better than classic Burgers model. The determination coefficients of the fractional order creep model were within 0.995.

(2) A caving zone subsidence prediction equation was built based on the creep model. The caving zone deformation data of simulation experiment and the field was fitted with the prediction equation to verify the accuracy. The determination coefficient of them are 0.997 and 0.999, respectively.

References

- Cao LL. Study on fracture mechanism and fractional order model of seepage-creep for coal measures sandstone. China University of Mining and technology Xuzhou. Doctoral thesis 2017. (In chinese)
- Li CR. Study on Failure Characteristics and Settlement Prediction Method of Mining Overburden. China University of Mining and technology Xuzhou. Master's thesis 2017. (In chinese)
- Li M, Zhang J, Meng G, et al. Testing and modelling creep compression of waste rocks for backfill with different lithologies. *Int J Rock Mech Min Sci*, 2020, 125: 104170.
- Peng Y, Zhao J, Li Y. A wellbore creep model based on the fractional viscoelastic constitutive equation. *Pet Explor Dev*. 2017;44:1038-1044.
- Wu F, Liu JF, Wang J. An improved Maxwell creep model for rock based on variable-order fractional derivatives. *Environ Earth Sci*. 2015;73:6965-6971.

CHAPTER 7

7 Conclusions

Ground subsidence in underground coal mining areas causes environmental damage and creates hazards on the ground surface, which is long-term, widely distributed, and can lead to large-scale geological disasters. Achieving a high-precision method to predict mining subsidence deformation is very important for assessing environmental damage and identifying countermeasures. The longwall mining system is a very productive and efficient method and is widely used throughout the world as a coal mining technique. During longwall mining, the immediate roof caves in behind the hydraulic shield support as coal is continuously extracted and then overlying strata hangs up to form a rock beam. As the longwall face continually advances, the rock beam breaks into large blocks and then collapses when the span reaches a certain limiting value. The broken rock fills in the goaf area in a space termed a caving zone. The overburden strata can be divided into three vertical zones including the continuous deformation zone, the damage zone, and the caving zone. Brillouin optical time-domain reflectometer (BOTDR) technology is introduced and adopted in this study to obtain the movement data along the vertical direction above the goaf. According to the results of the field measurements, the deformation of the caving zone is the most complex, and the long-term behavior has not yet been clarified. Therefore, this research discusses the deformation mechanism and long-term behavior of the caving zone by means of field investigations, laboratory tests and numerical simulations.

The main conclusions in this research is as follows:

Chapter 2: The BOTDR technique is described in this chapter for measuring ground movement of longwall coal mining. The returning strain from the BOTDR technology may differ from the rock mass surrounding the monitoring site since it can only measure the strain at specific monitoring points. Hence, if the strain detected by BOTDR technology at the monitoring point is assumed to be the same as total rock

mass deformation, especially in caving zones and damage zones, a high cumulative error would be predicted. A new calculation model is developed, which can determine ground deformation above goaf using data returned by BOTDR technology. The overburden above the goaf is divided into three zones in this model: caving zone, damage zone, and continuous deformation zone, and constitutive models of each zone are developed. The caving zone is represented as a constitutive model of rock fragment. The compressive deformation of the rock mass and the sliding behavior among rock particles are included in the deformation of this model. As an elastoplastic body, the damage zone is represented as the fracture zones. The elastic deformation zone and unconsolidated zone, which may be treated as an elastic body, are represented by the continuous deformation zone. The total deformation of each zone can be used to compute the amount of surface subsidence above the goaf.

Chapter 3: The field research and analysis of measurement data is undertaken in Zhangzhuang coal mine, Anhui Province, China to analyze the applicability of BOTDR Technology, the long-term behavior of each zone, and the applicability of calculation models given in Chapter 2. According to the deformation characteristics, the overburden can be categorized into three zones based on the measurement data: the continuous deformation zone, the damage zone, and the caving zone. After the extraction of longwall panels, there is large strain in the caving zone, and it gets larger with time. Furthermore, the long-term deformation behaviors of the damage and continuous deformation zones can be simulated as a result of predicting the deformation in each zone using the calculation model proposed in this research. However, the long-term deformation behavior of the caving zone cannot be simulated, and it is remarkable differences between the predicted value and measured one. As a result, in order to predict long-term ground behavior owing to the longwall coal mining, the long-term deformation behavior of the caving zone has to be understood and modeled.

Chapter 4: In order to understand the long-term deformation behavior of the caving zone, a series of triaxial creep tests are conducted using the specimen that

simulates the caving zone filled with rock fragments under different axial pressures, confining pressures and size distributions of rock fragments. Based on the results of a series of creep tests, it can be said that both the axial and confining pressures have an obvious impact on the creep behaviors of the specimen. The creep strain increases with increasing the axial pressure and decreases with increasing the confining pressure. Moreover, it also can be recognized that the breakage of rock fragments inside of the specimen occur during creep tests and this phenomenon also has an obvious effect on the creep behavior of the specimen. Here, the relative breakage index, which is calculated by the total breakage volume divided by the total volume of rock fragments, is introduced in order to evaluate the breakage degree of rock fragments in the specimen. The size of rock fragments in the specimen has an obvious impact on the breakage behavior of rocks and the breakage index become large when the contents of large size rock fragments is large. In addition, as the breakage index increases with increasing confining pressure, it can be expected that the decrease of creep strain with increasing confining pressure is due to the internal structural change of the specimen. Therefore, it can be said that the bulking coefficient, which represents the characteristics of volume expansion, is an important factor for prediction of long-term deformation behavior of the caving zone.

Chapter 5: The bulking coefficient plays an important role for long-term deformation behavior of the caving zone. In order to understand the long-term deformation behavior and determine the bulking coefficient of the specimen that simulates the caving zone, a three-dimensional numerical model of the specimen is developed and simulated by means of Particle Flow Code (PFC) Ver. 5.0. The failure criterion of the rock fragments in the specimen is also implemented in this simulation. Based on the results of a series of numerical simulations, the deformation behavior of the specimen can be understood and the creep behaviour of the specimen can be simulated by Burgers creep model. Moreover, as the particle size distribution of rock fragments in the specimen, the axial and confining pressures have an obvious impact on the bulking coefficient of the specimen, the deformation characteristics parameter

which represents the effects of the particle size distribution of rock fragments in the specimen, axial and confining pressures on the bulking coefficient is determined and introduced. Then the bulking coefficient under different conditions and elapsed time can be predicted.

Chapter 6: In this chapter, a new creep model is proposed in order to predict long-term behavior of the caving zone considering the change of bulking coefficient of caving zone. The new model attempts to predict the long-term behavior of the caving zone by incorporating the deformation characteristics parameter into the transition creep factor in the Burgers creep model. Compared with the results of the triaxial compressive tests, it can be said that the new creep model can simulate the behavior of the specimen simulated caving zone more accurately than the classic Burgers model. Moreover, compared with the results of laboratory tests with excavation model and the field measurement data of the caving zone in Zhangzhuang coal mine, it can be verified that the new proposed model can predict the long-term deformation behavior of the caving zone.

Supplement

Table S1 Fitting parameters of the fractional order creep model of broken rock

		E_0 (MPa)	E_1 (MPa)	η_1 (Gpa)	η_2 (Gpa)	α	β
G5-3	2 MPa	105.73	115.82	6.918×10^5	/	0.335	/
	4 MPa	98.94	112.20	5.53×10^4	/	0.420	/
	6 MPa	90.16	159.77	1.692×10^5	1.371×10^4	0.482	0.483
	8 MPa	89.22	157.99	3.112×10^5	7.195×10^3	0.501	0.496
G4-3	2 MPa	58.06	110.08	4.461×10^5	/	0.370	/
	4 MPa	68.16	101.61	2.621×10^5	/	0.379	/
	6 MPa	70.76	150.20	3.177×10^5	1.466×10^4	0.479	0.473
	8 MPa	71.20	150.61	3.596×10^5	8.571×10^3	0.502	0.500
G3-3	2 MPa	94.14	128.91	1.726×10^6	/	0.351	/
	4 MPa	96.14	118.49	2.447×10^5	/	0.386	/
	6 MPa	85.89	173.61	1.309×10^5	7.450×10^3	0.521	0.520
	8 MPa	87.83	161.08	2.679×10^5	7.299×10^3	0.514	0.514
G2-3	2 MPa	79.48	124.19	6.338×10^5	/	0.392	/
	4 MPa	82.05	100.70	2.076×10^5	/	0.387	/
	6 MPa	70.71	143.10	2.748×10^5	1.224×10^4	0.511	0.494
	8 MPa	73.93	133.65	4.350×10^5	9.592×10^3	0.497	0.492
G1-3	2 MPa	81.71	123.04	3.752×10^5	/	0.384	/
	4 MPa	87.11	109.87	2.594×10^5	/	0.392	/
	6 MPa	83.83	154.33	1.891×10^5	9.428×10^3	0.515	0.506
	8 MPa	85.75	146.26	2.461×10^5	5.870×10^3	0.517	0.517